

Dynamics and phases of matter in open quantum many-body systems

by

Shengqi Sang

A thesis
presented to the University of Waterloo
in fulfillment of the
thesis requirement for the degree of
Doctor of Philosophy
in
Physics

Waterloo, Ontario, Canada, 2024

© Shengqi Sang 2024

Examining Committee Membership

The following served on the Examining Committee for this thesis. The decision of the Examining Committee is by majority vote.

External Examiner: Chao-Ming Jian
Assistant Professor, Cornell University

Supervisor(s): Timothy H. Hsieh
Adjunct Faculty, University of Waterloo
Roger G. Melko
Professor, University of Waterloo

Internal Member(s): Anton A. Burkov
Professor, University of Waterloo
Beni Yoshida
Adjunct Faculty, University of Waterloo

Internal-External Member: David Gosset
Associate Professor, University of Waterloo

Author's Declaration

This thesis consists of material all of which I authored or co-authored: see Statement of Contributions included in the thesis. This is a true copy of the thesis, including any required final revisions, as accepted by my examiners.

I understand that my thesis may be made electronically available to the public.

Statement of Contributions

This thesis is based on four research manuscripts. Shengqi Sang is the first author for all four manuscripts.

Chapter.2 of this thesis consists mostly of material published in Ref.[1]. This work was done under the supervision of Timothy H. Hsieh.

Chapter.3 of this thesis consists mostly of material published in Ref.[2]. This work was done in collaboration with Zhi Li, and was supervised by Beni Yoshida and Timothy H. Hsieh.

Chapter.4 and 5 of this thesis consists mostly of material published in Ref.[3]. This work was done in collaboration with Yijian Zou, and was supervised by Timothy H. Hsieh.

Chapter.6 of this thesis consists mostly of material published in Ref.[4]. This work was done under the supervision of Timothy H. Hsieh.

Abstract

The thesis is divided into two parts, both focusing on the topic of open quantum many-body systems.

The first part explores the properties of quantum circuits interspersed with measurements. Tuned by the frequency of measurements, the circuit exhibits two stable dynamical phases: a weakly-monitored phase and a strongly-monitored one. For the former case, we analyze its non-equilibrium properties and unveil that it exhibits physical length scales that grow super-linearly with time. For the latter case, we demonstrate that it can maintain non-trivial quantum order when symmetries are present.

The second part addresses phases of matter for mixed many-body states. We propose a real-space renormalization group approach for mixed states and apply it to derive phase diagrams for various examples. For decohered topological codes, we establish a precise relationship between the decodability and the topological phase transitions. Lastly, we introduce the notion of ‘Markov length’, a length scale that measures the locality of correlation, as a diagnostic for the stability of mixed state phases.

Acknowledgments

I would like to start by expressing my deepest gratitude to my PhD advisor, Tim Hsieh, for all the guidance, support, and encouragement throughout this journey. He has always been willing to invest time in discussing physics with me and sharing his most interesting and thought-provoking ideas. I have been consistently amazed by his broad knowledge of the field and his unique approach to physics. His passion for science, his thoughtfulness, and his optimistic attitude have continually inspired me over the years. I am also grateful to him for his attentiveness during my early PhD years and for encouraging me to become an independent researcher as I approached the end.

My five-month visit at KITP was memorable and fulfilling. I am indebted to Professor Matthew Fisher for his warmest mentorship during my stay. Discussing physics with him was a rewarding and enjoyable experience. I extend my thanks to Yimu Bao, Jake Hauser, and Ali Lavasani for the wonderful moments we shared and for our collaboration. I would also like to acknowledge other graduate fellows in my cohort, especially Shankar Balasubramanian, Noam Chai, Kuan-Sen Lin, Aditya Mahadevan, and Pasha Nosov, for their suggestions and emotional support during my postdoc application process.

I received substantial support from others during my PhD years at the Perimeter Institute. I am particularly grateful to Ziwen Liu for sharing his expertise in quantum information theory and for countless inspiring discussions, Roger Melko for generously providing computational resources, Beni Yoshida for his patience in helping me improve a manuscript and for career advice, and Yijian Zou for teaching me tensor network techniques and for collaborations. I also extend thanks to Tyler Ellison, Zhi Li, Leonardo Lessa, Peter Lu, Ruochen Ma, Weicheng Ye, and Liujun Zou for extensive discussions over the years, from which I benefited greatly. Additionally, I cherish the day-to-day interactions with Yushao Chen, Guillaume Dideron, Jacob Lin, Shuwei Liu, Xiuzhe Luo, Han Ma, Amirreza Negari, Dongjin Lee, Jinmin Yi, Lei Yang, Shiyu Zhou, Keyou Zeng, Keke Zhang, and Zheng Zhou.

I am fortunate to have had the opportunity to interact with exceptional researchers outside of PI. I am particularly thankful to Yaodong Li for teaching me about monitored quantum dynamics and sharing his insights on a variety of other topics. I also extend my thanks to Tarun Grover for stimulating discussions and encouragement when I visited UCSD, and to Yuhan Liu for an invited talk at MPQ. Additionally, I am grateful to Tomotaka Kuwahara and Yusuke Kimura for an ongoing collaboration.

I thank my parents and grandparents for their overwhelming love, without which I could not be who I am today. Finally, I thank my wife Hao Xu for her love and companionship in this journey.

Table of Contents

Examining Committee Membership	ii
Author's Declaration	iii
Statement of Contributions	iv
Abstract	v
Acknowledgments	vi
List of Figures	xi
1 Introduction	1
1.1 Dynamical phases in monitored quantum circuits	2
1.1.1 Relation to later chapters	5
1.2 Quantum phases of many-body mixed states	5
1.2.1 Relation to later chapters	8
2 Measurement protected quantum phases	10
2.1 \mathbb{Z}_2 symmetric monitored circuit model	10
2.2 Phase Diagram	12
2.3 Higher dimensions and other architectures	18
2.4 Discussions and outlook	21

3	Information dynamics in weakly monitored quantum circuits	22
3.1	Main results	22
3.2	Entanglement Dynamics	25
3.2.1	Stabilizer length distribution in clipped gauge	25
3.2.2	Entropy of a contiguous region	28
3.2.3	Multipartite entanglement generation	30
3.2.4	Code distance growth	32
3.2.5	Code equilibrium v.s. entanglement equilibrium	35
3.2.6	Pure v.s. mixed initial state	36
3.3	Information dynamics	38
3.3.1	Input-Output correlation	38
3.3.2	Isomorphism between quantum codes	39
3.3.3	Logical operator growth	40
3.3.4	Loss of local information	42
3.3.5	Information spreading	44
3.3.6	Partially fixing the input state	46
3.4	domain-wall Picture	48
3.4.1	Review of domain-wall picture	48
3.4.2	Domain-wall interpretation of S_A	50
3.4.3	Domain-wall interpretation of $I_{A:B}$	52
3.4.4	Domain-wall interpretation of $I_{A_R:B_P}$	53
3.5	Discussions and outlook	54
4	Real-space renormalization group for quantum mixed states	57
4.1	Real-space RG of quantum mixed-states	58
4.1.1	From pure-state RG to mixed-state RG	58
4.1.2	Correlation-preserving map	60
4.1.3	Ideal mixed-state RG	62

4.1.4	From mixed-state RG to mixed-state quantum phases	64
4.2	Overview of examples	66
4.3	Noisy GHZ states	67
4.3.1	Bit-flip noise	68
4.3.2	Phase-flip noise	71
4.4	Thermal toric code state	72
4.4.1	Review of the toric code model	72
4.4.2	RG of the thermal toric code state	73
5	Mixed-state phases and quantum error correction	77
5.1	Logical information and long-range entanglement	77
5.2	LC transformation from the Harrington decoder	81
5.3	Truncated minimal weight perfect matching channel	85
5.4	Discussion and outlook	88
6	Markov length and mixed-state quantum phases	90
6.1	Quantum conditional mutual information and Markov length	90
6.2	Reversing a local quantum operation	92
6.3	Example: dephased toric code	94
6.4	$\tilde{\mathcal{G}}$ as a quasi-local decoder	98
6.5	Discussions and outlook	99
	References	100
	APPENDICES	120
A	Appendix for Chapter.1	121
A.1	Relation between pure- and mixed- state phase equivalence	121

B	Appendix for Chapter.2	123
B.1	Clifford Circuits with Symmetry	123
B.2	Details of sampling procedure	126
B.3	Entanglement entropy on other cross sections	127
B.4	Data for the Alternative Architecture	127
B.5	Further data for (2+1)D circuit at $p = 0.3$	127
C	Appendix for Chapter.3	132
C.1	Monitored dynamics as a quantum channel	132
C.2	Details about random polymer simulation	135
D	Appendix for Chapter.4	136
D.1	Various short proofs	136
D.1.1	Derivation of Eq.(4.11)	136
D.1.2	Derivation of Eq.(4.22)	137
D.1.3	Derivation of Eq.(4.39)	137
D.2	Convergence of real-space RGs	138
D.2.1	Classical statistical mechanics models	139
D.2.2	Noisy GHZ state in Sec.4.3	140
D.2.3	Thermal toric code state in Sec.4.4.2	142
D.3	Symmetric RG of $\mathbb{Z}_2 \times \mathbb{Z}_2$ cluster state	142
E	Appendix for Chapter.6	146
E.1	Petz recovery map	146
E.2	Derivation of Eq.(6.8)	147
E.3	Derivation of Eq.(6.12)	148
E.4	Tensor network technique for simulating $H(\mathbf{m})$	149
E.5	Details on numerical simulation in Fig.6.3	151
E.6	Mapping to RBIM's free energy	151
E.7	Convergence of dephasing Lindbladian	153

List of Figures

1.1	An illustration of (1+1)D monitored quantum circuit. Each blue block represents a random unitary gate drawn from the 2-qubit Clifford group. On each vertical bond, a projective measurement (represented as a green dot) in the Pauli- Z basis is applied with a probability p	3
1.2	A circuit of local channel gates represented as an LC transformation. . . .	6
2.1	Phase diagram of steady state of monitored circuit, which consists of brick-wall 2-qubit operations: measurement or Z_2 -symmetric Clifford unitary with probability p or $1-p$, respectively. Given measurement, it is either $M_1 = ZZ$ or $M_2 = XI$ measurement with probability r or $1-r$. The central portion is a critical regime, based on our (finite size $L = 768$) numerics, discussed in main text.	11
2.2	(a) The 2-qubit measurements are fermion parity measurements (denoted by the pair of arcs) on the 4 corresponding Majorana modes. The 2-qubit unitary acts locally on the 4 modes because it preserves fermion parity. A circuit with only measurements maps to loops of Majorana worldlines, as noted in [5]. (b) A circuit with only ZZ measurements and unitaries, and the minimal cut (blue line) for an interval with endpoint qubits (a, b) . A minimal cut in the area law phase also mediates spin glass correlation between a, b via the ZZ measurements traversed.	13
2.3	$r = 0.5$ cross section (equal probability for ZZ and X measurements). (left) Entanglement entropy versus log of partition size, for various p . (right) Mutual information decay in log-log plot. Total system size is $L = 768$	14
2.4	$r = 1$ cross section (unitaries and only ZZ measurements with probability p). (top) Entanglement entropy versus log of partition size for total system size $L = 768$ and spin glass order parameter versus log of system size, for various p . At $p_c \approx 0.38, 0.39$, the two exhibit log scaling. (bottom) Scaling collapse of both quantities with $\nu_S \approx 1.3, \nu_O \approx 1.5$	16

2.5	(left) Antipodal geometry. Intervals A and B are of the same size and centered on two antipodal points of the periodic qubit chain of length L . (right) Simulated mutual information $I(A, B)$ as a function of the ratio $ A /L$ at critical points corresponding to $r = 0$ (Z_2 -Clifford unitaries + X measurement) and $r = 1$ (Z_2 -Clifford unitaries + ZZ measurement).	17
2.6	(left) A cross section of the $(2 + 1)$ d circuit architecture. Black dots are qubits and each colored square denotes an operation acting on qubits within the square. An operation is either a random Ising-symmetric 4-qubit Clifford gate (yellow) or a series of 3 two-qubit measurements Z_1Z_2, Z_2Z_3, Z_3Z_4 (blue), with probability $1 - p$ or p . The circuit alternates between the background and foreground, which consist of two distinct partitions into sets of four. (right) The two order parameters $O(L, p)$ and $S_A(L, p)$ as functions of p . For the simulation of $S_A(L, p)$ the total system size is fixed to be $L = (L_x, L_y) = (60, 20)$	18
2.7	Alternative class of circuits with Z_2 -symmetric random unitaries always applied in brick-wall fashion, with in-between layers of $M_1 = Z_iZ_{i+1}$ measurements for every i , each applied with probability p . Phase diagram has a paramagnetic volume law phase, a critical regime, and spin glass area law phase. $p_{c,S} \approx 0.52, p_{c,O} \approx 0.58,$	20
3.1	An illustration of the spreading and decay of local information.	24
3.2	(a) Stabilizer length distribution $h(\ell, t)$ in an $L = 512$ circuit with open boundary condition. (b) The same data after rescaling the x and y axes by $t^{-\nu}$ and t^μ , respectively. The inset shows the same plot on a log-log scale.	27
3.3	(a) Dynamics of conditional mutual information $I_{A:B C}(t)$, on a periodic spin chain for various L . Inset shows the geometry of A, B and C , whose sizes are $ A = B = \frac{5}{24} C = \frac{1}{8}L$ (b) The collapse of $I_{A:B C}$'s data using the scaling form Eq. (3.32), with $(\mu, \nu) = (1.66, 1.5)$	33
3.4	Contiguous code distance, as defined in Eq. (3.39), plotted in the log-log scale. ϵ is taken to be 1.	35
3.5	Numerical results for a pure initial state. (a) Stabilizer length distribution $h(l, t)$ with $L = 512$ and open boundary condition, within the same time period as in Fig. 3.2 (b) Dynamics of $I_{A:B C}(t)$, with A, B and C arranged in the same manner as in Fig. 3.3(a). The inset shows the same data but with both axes rescaled by a factor of L^{-1}	36

3.6	A visualization of $ \phi_{\mathbf{m}}(t)\rangle$ defined in Eq. (3.43). Physical qubits (P , blue dots) and reference qubits (R , yellow dots) are initially maximally entangled and the circuit acts on the physical qubits only.	38
3.7	Arrangement of $A_R = [-a, a]_R$ and $B_P = [-d, d]_R$ in the numerical simulation. The figure shows the special case of $a = 1$ and $d = 3$	42
3.8	Decay of the remaining \mathcal{I}_A within the system for various different A 's sizes.	43
3.9	Simulation results for $I_{A_R:B_P}(t)$ in a system with $L = 768$ qubits. (a)(b) Heatmaps of the normalized mutual information μ_{A_R,B_P} , as a function of t and $ B = 2d$, for unitary and monitored dynamics respectively. (c) The growth of $d_\epsilon(t)$ and $D_\epsilon(t)$ with $\epsilon = 0.01$. Both quantities develop power-law growing behaviors at late time. The D_ϵ curve has a plateau at late time as they reach the boundary of the simulated system.	45
3.10	(a) The circuit configuration for the alternative setting to characterize information spreading discussed in Sec. 3.3.6, where $A = \{3, 4\}$ (b) Decay of $A = [-a, a]$'s initial information with time t . (c) Heatmap of the normalized mutual information $\mu(d, t)$ in the alternative setting	47
3.11	Numerical result for the shortest path simulation. (a) Heatmap of the simulated $[\mu_{A_R,B_P}(t)]$. The figure should be compared with its counterpart in the Clifford simulation Fig. 3.9(b). (b) $[d_\epsilon(t)]$ and $[D_\epsilon(t)]$ extracted from the simulation data, with $\epsilon = 0.01$. The black dashed lines are power-law fittings, with fitted exponents shown in Eq. (3.81)	56
4.1	Real-space RG transformation of pure states – Circuit representation of two iterations of pure state RG transformation. At the ℓ -th iteration, the coarse-graining isometry $w^{(\ell)}$ is determined by the level's input state $ \psi^{(\ell)}\rangle$ using Eq.(4.1). By applying the circuit from bottom to top (red arrows), all the short-range features of the initial UV state are gradually discarded, and only long-range ones are kept in the IR state $\rho^{(\ell \rightarrow \infty)}$. By applying the circuit from top to bottom (blue arrows), the circuit generates the UV state $ \psi^{(1)}\rangle$	59
4.2	Tree tensor network of a GHZ state with $L = b^\ell = 9$, $b = 3$, $\ell = 2$. Each triangle represents an isometry w (Eq.(4.30)). By replacing the state at the top with a generic single qubit state $ \psi\rangle$, the same tensor network encodes $ \psi\rangle$ into a codeword state of the quantum repetition code.	67

4.3	RG scheme for the thermal toric code state – In all panels, a plaquette (vertex) is shaded (dotted) if has a non-zero probability of holding an m - (e -) anyon, and physical qubits are associated with edges of the lattice and drawn as circles. (left→mid) \mathcal{E}^X and \mathcal{E}^Z (see Eq.(4.62) and Eq.(4.64)) acts on each 2×2 block of plaquettes and vertices, respectively. The resulting state has anyons on one of its sublattices’ plaquettes and vertices. (mid→right) After disentangling with the unitary \mathcal{U} depicted in Eq.(4.65) and discarding the decoupled qubits, the new state is still a toric code Gibbs state, but with renormalized temperature p' (Eq.(4.67)) supported on a coarse-grained lattice.	75
5.1	Geometry of operators L_1 , L_2 , and K	79
5.2	RG of the dephased toric code state – (a) In each RG iteration, \mathcal{G} is applied in parallel to all the odd blocks (blue), then \mathcal{E}^X is applied to all the even blocks (green). Finally disentangling unitaries (see Eq.(4.65), not drawn in the figure) are applied to reduce the lattice size by half. (b) RG flow of the anyon density $q_p^{(\ell)}$. (c) Iteration relation of $q_p^{(\ell)}$ when approaching 0, for various choices of p	83
5.3	A sample anyon configuration for noisy toric code – A dashed line on an edge denotes the corresponding qubit’s phase is flipped by an Z operator. Anyons are created in plaquettes (shaded) where an odd number of dashed lines meet.	84
5.4	Truncated minimum weight perfect matching channel – (a) For a given block B , the corresponding channel $\mathcal{E}_{B,a}$ acts on both B and a buffer region F of a width a . (b) $\mu(a, p)$ is the probability that the truncated and global MWPM algorithms produce the same anyon pairings. It is plotted against p for various choices of a	86
6.1	(left) Quantum conditional mutual information $I(A : C B)$ quantifies how non-local is the correlation between A and its complement. When $I(A : C B)$ decays exponentially with B ’s width r , we call the corresponding length scale the Markov length ξ . (right) The dark grey line is a path of mixed-states generated from local Lindbladian evolution, <i>i.e.</i> $\rho_t = \mathcal{T} \exp(\int_0^t \mathcal{L}(\tau) d\tau)[\rho_0]$. For each segment in which ξ remains finite, <i>e.g.</i> below (above) the dashed line, we argue there exists a quasi-local Lindbladian $\tilde{\mathcal{L}}_{1(2)}$ that reverses \mathcal{L} ’s action. Thus states within each segment are in the same mixed-state phase.	91

6.2	Reversal circuit for continuous evolution — (top left) Two layers of the forward circuit \mathcal{G} acting from bottom to top. Each box is a quantum channel $\mathcal{E}_{x,t} = \exp(\delta t \mathcal{L}_{x,t})$. (top right) Gates in each layer are reorganized into multiple layers so that any two gates in a layer are at least distance $2r$ separated (in the figure $r = 2$). (bottom) The reversal circuit $\tilde{\mathcal{G}}$ constructed from the reorganized \mathcal{G} by replacing each $\mathcal{E}_{x,t}$ with its reversal $\tilde{\mathcal{E}}_{x,t}$ (grey box) defined in Eq.(6.7). The reversal circuit acts from top to bottom.	93
6.3	CMI of dephased toric code state — (a) Partition with A fixed and varying r (width of B, C). (b) $I(A : C B)$ peaks around $p_c \approx 0.11$ and peak size decays with r . (c) Finite-size collapse with the scaling ansatz Eq.(6.14), with $(p_c, \nu, \alpha) = (0.11, 1.8, 1.1)$. (d) Above ($p = 0.15$) or below ($p = 0.05$) the critical point, CMI decays exponentially with r , in contrast to power-law decay at the critical point $p_c \approx 0.11$	95
B.1	Spin glass order parameter O as a function of time for a system of 512 spins at $r = 1, p = p_c = 0.39$	126
B.2	Entanglement entropy versus log of partition size near the critical points at $r = 0.25$ (top) and $r = 0.75$ (bottom). $L = 768$	128
B.3	Entanglement entropy versus log of partition size near the critical points at $p = 0.75$, two figures for two different ranges of r . $L = 768$	129
B.4	Entanglement entropy versus log of partition size, for various p , for the alternative architecture.	130
B.5	Spin glass order parameter versus log of system size, for various p , for the alternative architecture.	130
B.6	Simulated bipartite entanglement entropy $S_A(L, p)$ at $p = 0.3$ in (2+1)D circuit with varying partition size $A = (A_x, A_y)$. The total system size $L = (L_x, L_y) = (60, 20)$ and $A_y = 20$ are fixed while A_x is varying. For dashed line $(a_S, b_S) = (4.87, 35.85)$	131
B.7	Simulated spin-glass order parameter $O(L, p)$ at $p = 0.3$ in (2+1)D circuit with $L_y = 20$ fixed and L_x varying. For dashed line $(a_O, b_O) = (0.33, 0.67)$	131
E.1	Illustration of a non-simply connected region Q . Only qubits (edges) that belong to Q is drawn. Supports of the two non-local operators $A_{\bar{\square}}$ and $B_{\bar{\square}}$ surrounding the hole are denoted with green and blue edges, respectively.	148

Chapter 1

Introduction

Quantum computers, programmable devices that process quantum information, represent one of the most exciting applications of quantum mechanics. After decades of development, intermediate-scale devices nowadays are capable of supporting several hundred qubits. Despite challenges like short coherence times and limited qubit counts, these devices can already execute complex tasks, including preparing exotic many-body states [6, 7, 8], simulating quantum dynamics [9, 10, 11, 12], and demonstrating competitive computational power in specific tasks [13, 14, 15]. This raises intriguing questions about the capabilities of these devices, both in computational tasks and in probing novel quantum many-body phenomena.

These programmable quantum devices differ in several key aspects from other quantum many-body systems, particularly those in condensed matter. They enable controlled operations and measurements of individual qubits, providing the flexibility to generate highly-entangled states that are inaccessible in condensed matter systems. However, these devices are also subject to consistent decoherence due to environmental coupling, which impairs the 'quantumness' of any generated state. Although this adverse effect can be minimized, it can never be completely eliminated and tends to worsen with larger system sizes and an increased number of operations. The interplay between controlled operations and decoherence gives rise to a wide range of open system quantum phenomena and presents many interesting theoretical challenges.

This thesis studies two topics within this broad context. In Chapters 2 and 3, we explore the properties of quantum dynamics involving projective measurements. Subsequently, in Chapters 4, 5, and 6, we consider how to extend the concept of quantum phases of matter to mixed states. We first review necessary background on both topics to set the stage for

later chapters.

1.1 Dynamical phases in monitored quantum circuits

Unlike classical systems, where measurements solely extract information, in quantum systems, measurements also non-trivially alter the state of the system. Consider a quantum state ρ measured in a basis $\mathcal{M} = \{P_1, P_2, \dots, P_k : \sum_{\alpha} P_{\alpha} = \mathbb{I}\}$. If the measurement outcome is $\alpha \in \{1, \dots, k\}$, the state of the system changes according to:

$$\rho \rightarrow \frac{P_{\alpha}\rho P_{\alpha}}{\text{tr}(P_{\alpha}\rho)} \tag{1.1}$$

This transformation occurs with a probability $\text{tr}(P_{\alpha}\rho)$. It is important to note that randomness is an inherent aspect of projective measurements and cannot be eliminated by any physical means. Quantum dynamical processes that involve both unitary evolution and measurement are vividly termed 'monitored quantum dynamics'.

Many crucial protocols in quantum information science are examples of monitored dynamics. For instance, active quantum error correction [16] involves periodic measurements on a quantum memory to detect the type of error occurring during computation. Based on the outcomes of these measurements, specific unitary operations are executed to mitigate the effects of the error. Another example is Measurement-based Quantum Computation (MBQC) [17]. In MBQC, using an entangled many-body state (cluster state) as a resource state, quantum computation is driven entirely by single-qubit measurements and subsequent feedbacks.

These protocols represent finely-tuned monitored dynamics, designed to fulfill specific tasks in quantum information processing. Conversely, from the standpoint of many-body physics, it is more desirable to explore the common properties of generic monitored dynamics. The monitored quantum circuit serves as a toy model for investigating these properties.

For concreteness, in the rest of this section we focus on a prototypical monitored quantum circuit, independently proposed in [18, 19, 20, 21]. The circuit is defined on an array of qubits. At the t -th time steps, two sub-steps happen sequentially:

1. Depending on whether t is odd or even, an array of two-qubit quantum gates $\{U_{12}^{(t)}, U_{34}^{(t)}, \dots\}$ ($\{U_{23}^{(t)}, U_{45}^{(t)}, \dots\}$) is applied to all odd (even) pairs of qubits. These unitaries are randomly and independently selected from a certain unitary ensemble.

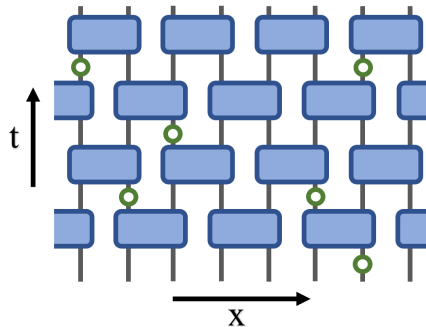


Figure 1.1: An illustration of (1+1)D monitored quantum circuit. Each blue block represents a random unitary gate drawn from the 2-qubit Clifford group. On each vertical bond, a projective measurement (represented as a green dot) in the Pauli- Z basis is applied with a probability p .

2. Each qubit is subjected to a projective measurement in the Pauli- Z basis with a probability p . Based on the measurement outcome, the quantum wavefunction collapses in accordance with rule 1.1.

An example of the circuit is depicted in Fig.1.1. We note that the dynamics involve both classical randomness, due to the random selection of unitary gates and measurement locations, and quantum randomness from measurement outcomes. We are interested in the behavior of typical dynamics for both types of randomness. Two ensembles of unitary gates are commonly considered in the literature: the Haar unitary ensemble and the Clifford unitary ensemble. The former is the most generic ensemble of unitary gates and facilitates theoretical analysis. The latter, however, can be efficiently simulated owing to the Gottesman-Knill theorem[22, 23, 24]. The most universal properties of the dynamics, as reviewed below, are largely insensitive to the choice of ensemble.

Entanglement provides a crucial lens to understand monitored quantum circuits[25, 20]. For a quantum state $|\psi\rangle$, the amount of quantum entanglement between a region A and its complement \bar{A} is quantified by von Neumann entropy:

$$S_A = -\text{tr}(\rho_A \log \rho_A) \tag{1.2}$$

where $\rho_A := \text{tr}_{\bar{A}}(|\psi\rangle\langle\psi|)$ is the reduced density matrix for the region A .

Unitary gates and measurements has opposite effects on a state's entanglement structure. To understand this we consider limiting points of monitored circuits. When $p = 0$ the dynamics is free from measurements and reduces to a random unitary circuit, which tends

to generate entanglement across different parts of the qubit chain. In this limit, any input pure state rapidly thermalizes, and becomes indistinguishable from a typical random state on the spin chain. In particular, a subregion A 's von Neumann entropy is proportional to the region's size, *i.e.* $S_A = O(|A|)$. Conversely, at the other extreme where $p = 1$, measurements are deterministically applied to every single qubits at each time step. Each measurement collapses the qubit into either $|0\rangle$ or $|1\rangle$, thus regardless of the initial state, it is 'frozen' to a product state at all time steps and has no entanglement.

Away from limiting points, the competition between unitary evolution's entangling power and measurements' collapsing power leads to two phases, a weakly monitored phase and a strongly monitored one, separated by a phase transition occurring at a critical measurement frequency p_c . The transition is usually called the measurement-induced phase transition.

In the weakly monitored phase (also referred to as the volume-law phase in this context), the entangling power dominates the collapsing power, leading to entanglement among extensive degrees of freedom. A pure steady state in this regime is volume-law entangled: for a contiguous regime A much smaller than the total system size, its von Neumann entropy is:

$$S_A = a_1|A| + a_2|A|^\beta + \dots \quad (1.3)$$

where $\beta \approx 0.33$. The presence of the sub-leading term distinguishes the state from a typical random state and has deep connection to the Kardar-Parisi-Zhang (KPZ) universality class [26]. Conversely, in the strong monitored phase (or the area-law phase), single site measurements are so frequent that unitary gates do not have chance to generate much entanglement. More specifically, steady states in this regime are area-law entangled, *i.e.*

$$S_A = O(|\partial A|) = O(1) \quad (1.4)$$

throughout the dynamics, which resembles entanglement structure of gapped ground states. Exactly at the measurement-induced transition point, entanglement scales logarithmically with L , can be describable by a conformal field theory [27, 28].

An alternative method to describe two phases involves their capability to purify a maximally mixed initial state [29]. Measurement can extract entropy from a physical system. Indeed, in the strongly monitored phase, $O(1)$ -time monitored dynamics are sufficient to extract all entropy from the system. However, this process is significantly hindered if unitaries occur frequently: in the weakly-monitored phase, an $O(L)$ amount of entropy persists for an exponentially long time, despite continuous measurements. This phenomenon can be understood through the lens of quantum error correction [30, 31]: rapid unitary dynamics scrambles local information and 'hides' it within a dynamically generated quantum

error correcting code. Consequently, a substantial amount of information survives local measurements, resulting in a very long purification time.

1.1.1 Relation to later chapters

Since steady states of strongly monitored phase has similar entanglement structure as ground states, one naturally wonders whether familiar ground state quantum phases can appear as steady states. In Chapter.2, we give an affirmative answer by introducing a class of monitored quantum circuits which host long-range order in its strongly monitored phase. The circuit has unitaries respecting a global Ising symmetry and two competing types of measurements. The phase diagram has an area law phase with spin glass order, which undergoes a direct transition to a paramagnetic phase with volume law entanglement, as well as a critical regime.

In Chapter.3, we study behavior of the weakly monitored phase well before the equilibrium is reached. We show that, due to measurements, the entanglement dynamics in monitored circuits is indeed “faster” than that of unitary ones in several ways. Specifically, we find that a pair of well-separated regions can become entangled in a time scale $\ell^{2/3}$, sub-linear in their distance ℓ . In addition, we find initially local information can spread super-linearly with time as $t^{3/2}$. Furthermore, by viewing the dynamics as a dynamical encoding process, we show that the super-ballistic growing length scale relates to an encoding time that is sublinear in system size.

1.2 Quantum phases of many-body mixed states

Understanding quantum phases of matter is a central task of quantum many-body physics. The traditional focus is on pure states, which are typically ground states of local Hamiltonians. However, in actual quantum systems with inevitable decoherence, one always needs to deal with mixed-states. It is thus natural to ask how the notion of phase of matter can be generalized to cover these states.

One way of defining *pure-state* phases is via local unitary (LU) circuits [32]: two states are in the same phase if there is a short-depth LU circuit that connects them. This is based on the physical intuition that phases should be defined by long-range properties and representatives only differ in their local properties. For mixed states, an analogous definition was proposed by Coser and Perez-Garcia [33]: two mixed states ρ_1 and ρ_2 are in the same phase if there exists a pair of short-time local channel transformations bringing

ρ_1 to ρ_2 and from ρ_2 to ρ_1 . In this section, we formalize the definition provided above, elucidate the intuitions underlying it, and review some straightforward conclusions that follow from the definition. We emphasize that the differences between our definition and the one described in [33] are technical rather than fundamental.

We start by introducing a formal definition of local channel transformations, which follows the proposal in [34].

Definition 1 (Local channel (LC) transformation). On a given lattice of linear dimension L , a range- r LC transformation is a quantum channel composed of the following steps:

- (1) Adding qubits to each lattice site, all initialized in the $|0\rangle$ state;
- (2) Applying a range- r unitary circuit U on the lattice;
- (3) Tracing out some qubits on each lattice site.

The range of a circuit is defined as the maximal range of each unitary gate times the depth of the circuit. Henceforth if r is not specified for an LC transformation, it is assumed that $r/L \rightarrow 0$ in the thermodynamic limit.

The major difference between local channel transformations and local unitary ones (LU) [32] is step (3). In local unitary transformations, a qubit can be discarded only when it is disentangled from the rest of the system. In that context, (1) and (3) are inverse operations, and hence LU transformations are invertible. In contrast, LC transformations allow discarding a qubit that is still entangled with the rest of the system, *i.e.* $\rho_{i,\bar{i}} \neq \rho_i \otimes \rho_{\bar{i}}$ with i being the qubit to be discarded and \bar{i} being the rest of the system. As a result, LC transformations are generically non-invertible.

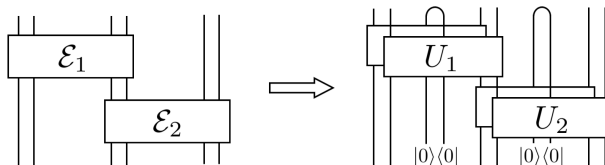


Figure 1.2: A circuit of local channel gates represented as an LC transformation.

LC transformations constitute a broad class of operations including any circuit composed of local channel gates, *i.e.* channels that only act on local domains of sites. To show this, one needs the Stinespring dilation theorem: any quantum channel $\mathcal{E}_{X \rightarrow Y}$ can be rewritten as:

$$\mathcal{E}(\cdot) = \text{tr}_{A'} (U((\cdot) \otimes |0\rangle\langle 0|_A)U^\dagger) \quad (1.5)$$

where U is a unitary map from $X \cup A$ to $Y \cup A'$. In other words, any quantum channel can be implemented by adding some degrees of freedom, applying a unitary on the joint system,

and discarding some degrees of freedom. Applying the theorem to a circuit of channel gates, one can first replace each channel gate with its Stinespring dilation form. Then one can move forward all the ancillae addition to the beginning of the circuit and postpone all the tracing-out to the end of the circuit. We graphically illustrate this in Fig.1.2. Furthermore, any finite-time local Lindbladian evolution can also be approximated by LC transformations by trotterizing the continuous dynamics.

The circuit definition of pure state phases reflects the idea that phases of matter should be characterized by long-range properties of the state, and should remain unchanged under reversible local modifications. LC transformations, albeit local, are generally not reversible and can destroy long-range correlations. As an example, if one starts from an arbitrary state $|\psi\rangle$ and applies the amplitude damping channel $\mathcal{E}_{\text{damping}}(\cdot) := \text{tr}(\cdot) |0\rangle\langle 0|$ to each qubit in the system, the resulting state would be a product state $|0\rangle^{\otimes L}$ without any non-trivial long-range correlation. On the other hand, an LC transformation's ability to create correlations is no stronger than LU ones. This follows from the fact that an LC transformation is some LU followed by discarding some degrees of freedom.

Thus the connectivity under LC transformations induces a partial order relation among mixed-states. States are ordered according to the amount of long-range correlation they possess: if $\rho_2 = \mathcal{C}(\rho_1)$ for some LC transformation \mathcal{C} , then ρ_1 has at least as much long-range correlation as ρ_2 . This naturally leads to the following definition of mixed-state phase equivalence ¹

Definition 2 (Mixed-state phase equivalence). On a given lattice, two many-body mixed states ρ_1 and ρ_2 are in the same phase if there exists a pair of LC transformations C_1 and C_2 such that $C_1(\rho_1) \approx \rho_2$ and $C_2(\rho_2) \approx \rho_1$.

Several clarifications regarding the definition:

- **Mixed-states of interest:** Though the definition above does not assume any restrictions on states $\rho_{1,2}$, we are interested in physically relevant mixed states such as local Hamiltonian Gibbs states at finite temperature, gapped ground states subject to decoherence, and steady states of local Lindbladians.
- **The precise meaning of ‘ \approx ’:** This requires some distance measure of mixed states. For instance, we could define two mixed states $\rho \approx \sigma$ if and only if $F(\sigma, \rho) > 1 - \epsilon$ for some small $\epsilon > 0$, where $F(\sigma, \rho) := \|\sqrt{\sigma}\sqrt{\rho}\|_1$ is the (Uhlmann) fidelity.

¹The definition resembles the one taken in [33], where a pair of LC transformations is replaced by a pair of (quasi-)local Lindbladian evolutions. A similar definition also appears in [35] when defining mixed-state symmetry-protected topological orders.

- **Ranges of LC transformations $C_{1,2}$:** In general we only require the range to be much smaller than the linear size of the lattice $\rho_{1,2}$ is defined on. But as we will see later, it will be sufficient to have a range $r = O(\text{polylog}(L/\epsilon))$ when $\rho_{1,2}$ have finite correlation length.

The definition is a generalization of pure-state phase equivalence defined through LU transformations. When restricting to pure many-body states, one can show that two states $|\psi_1\rangle$ and $|\psi_2\rangle$ are of the same mixed-state phase if and only if $|\psi_1\rangle$ and $|\psi_2\rangle \otimes |\phi\rangle$ are of the same pure-state phase for some invertible state $|\phi\rangle$. We provide a proof in App.A.1.

Product states, *e.g.* $|0\rangle^{\otimes L}$, are states without any long-range correlations. This is also reflected by the partial order relation under LC circuits: any state can be turned into the product state by a LC transformation which only consists of the amplitude damping channel. Thus we identify the *trivial phase* as the set of states that can be LC transformed from the product state. In other words, a mixed state is in the trivial phase if it can be written as $\rho_{\text{trivial}} = \mathcal{C} \left[|0\rangle^{\otimes L} \langle 0|^{\otimes L} \right]$ for some LC transformation \mathcal{C} . This is equivalent to requiring that the state can be locally purified into a short-range entangled pure state.

We comment that the above definition treats quantum and classical correlations on the same footing. As an example, the state $\rho = \frac{1}{2}(|0^{\otimes L}\rangle \langle 0^{\otimes L}| + |1^{\otimes L}\rangle \langle 1^{\otimes L}|)$ is a classical ensemble of L spins which is non-trivial under the above definition, because it has classical long-range correlation. To single out states that contain long-range classical correlation only, we can define a state to be in a *classical phase* if it can be written as $\rho_{\text{classical}} = \mathcal{C}(\rho_{\text{Pr}(\mathbf{s})})$ for some LC transformation \mathcal{C} . Here $\rho_{\text{Pr}(\mathbf{s})} := \sum_{\mathbf{s}} \text{Pr}(\mathbf{s}) |\mathbf{s}\rangle \langle \mathbf{s}|$ is a classical distribution $\text{Pr}(\mathbf{s})$ of product states $\{|\mathbf{s}\rangle : \mathbf{s} \in \{0, 1\}^L\}$ represented as a density matrix.

1.2.1 Relation to later chapters

In chapters 4, 5 and 6, we leverage the definition Def.2 in identifying mixed-state phases and characterizing their properties.

In Chapter 4, we propose a real-space renormalization group (RG) scheme for identifying mixed-state phases. We show that if the RG's coarse-graining maps preserve correlations with the complementary systems, then the state before and after the RG must be of the same phase. As an application, we demonstrate an exact RG flow of finite temperature toric code in two dimensions to infinite temperature, thus proving it is in the trivial phase.

In Chapter 5, we discuss connections between quantum error correction and mixed-state phases. We prove a precise relation between toric code's mixed state phase and decodability, by proving that local noise acting on toric code cannot destroy logical information

without bringing the state out of the toric code phase. We also show how decoders can be used to construct LCs for proving mixed-state phase equivalence.

In Chapter 6, we propose criteria for the stability of mixed-state quantum phases. We define Markov length – the length scale at which the conditional mutual information decays exponentially. We show that when evolving a mixed-state with a local Lindbladian evolution, the state’s Markov length remaining finite implies the state’s phase of matter is unchanged. We then demonstrate our general result with a concrete example, the dephased toric code state.

Chapter 2

Measurement protected quantum phases

In this chapter, we study whether area-law phase of monitored circuits can host area-law state with long-range order. We focus on a class of monitored quantum circuits with \mathbb{Z}_2 global symmetry. The model has a phase diagram which contains both a direct transition between spin-glass area law phase and paramagnetic volume law phase as well as a critical regime. The mutual information at these entanglement transitions exhibits distinct power law scaling, indicating new universality classes due to the global symmetry. We also analyze a two-dimensional version of the monitored circuit which enables coexistence of spin-glass order and volume law entanglement.

2.1 \mathbb{Z}_2 symmetric monitored circuit model

We focus on an ensemble of circuits C acting on a one-dimensional chain of qubits of length L with periodic boundary conditions. The circuit architecture consists of a brick-wall pattern of two-qubit operations (Fig. 2.1). Each operation is either a measurement (M), with probability p , or a random unitary (U), with probability $1 - p$. Given that an operation is a measurement, there are two types of measurements M_1 and M_2 , with probability r and $1 - r$. For two neighboring qubits $i, i + 1$, we define M_1 to be the projective measurement of $Z_i Z_{i+1}$ and M_2 to be the projective measurement of X_i .

It is convenient for scalable simulation to choose the random unitary from an ensemble of Clifford gates, which have the property of mapping a string of Pauli operators to another

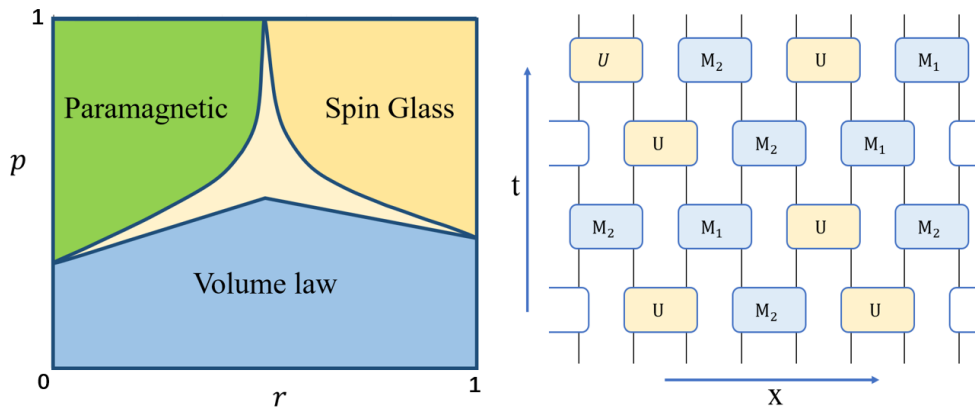


Figure 2.1: Phase diagram of steady state of monitored circuit, which consists of brickwall 2-qubit operations: measurement or Z_2 -symmetric Clifford unitary with probability p or $1 - p$, respectively. Given measurement, it is either $M_1 = ZZ$ or $M_2 = XI$ measurement with probability r or $1 - r$. The central portion is a critical regime, based on our (finite size $L = 768$) numerics, discussed in main text.

Pauli string (in the Heisenberg picture). This enables via the Gottesman-Knill theorem the efficient simulation of the circuit dynamics [22, 23, 24], as one need only track the evolution of polynomially many Pauli strings as opposed to an exponentially large wavefunction. It is important that we add an additional symmetry criteria to this ensemble: each Clifford gate U should map $X_i X_{i+1}$ to itself; this is sufficient and necessary for preserving a global Ising symmetry given by $\prod_{i=1}^L X_i$. Thus, both unitaries and measurements in the circuit commute with the Ising symmetry, which is clearly essential for defining any symmetry-breaking order. Details of this ensemble and Clifford/stabilizer technology can be found in the appendix B.1.

The initial state is the product state $|\psi_0\rangle = \otimes|+\rangle$, where $X|+\rangle = |+\rangle$. We are interested in the long time steady state properties after the initial state has been evolved with a deep random circuit $|\psi\rangle = C|\psi_0\rangle$. In our simulations, we average target quantities over both different realizations of the circuits and different time slices of a given realization at long time; we hereafter refer to this as “averaging over the circuit ensemble”. In particular, to distinguish area and volume law scaling of entanglement, we will compute the Renyi entanglement entropy of ψ after a bipartition into A and \bar{A} :

$$S_A = -\log \text{Tr}(\rho_A^2), \quad (2.1)$$

averaged over the circuit ensemble. Here $\rho_A = \text{Tr}_{\bar{A}}|\psi\rangle\langle\psi|$ and as different Renyi entropies

are identical for stabilizer states, we have specified without loss of generality the second Renyi.

We will also compute the spin glass order parameter

$$O = \frac{1}{L} \sum_{i,j=1}^L \langle \psi | Z_i Z_j | \psi \rangle^2 - \langle \psi | Z_i | \psi \rangle^2 \langle \psi | Z_j | \psi \rangle^2 \quad (2.2)$$

again averaged over the circuit ensemble. Given the Ising symmetry $\prod X$, the subtracted piece is always zero. This order parameter probes long-range entanglement in the following sense. For a product state, it is manifestly constant (unity), and the application of finite depth circuits can only lead to exponentially decaying correlators $\langle Z_i Z_j \rangle \approx e^{-|i-j|/\xi}$ from Lieb-Robinson bounds [36, 37]. Hence, in the trivial phase of product-like states, this order parameter is constant (independent of system size). On the other hand, consider an ideal spin glass state: a random cat or Greene-Horne-Zeilinger (GHZ) type state $|s\rangle + (\prod X)|s\rangle$, where s is a random spin configuration in the z -basis; for this state the order parameter grows linearly with L because $\langle Z_i Z_j \rangle^2 = 1$ for every i, j . Thus, the scaling of this order parameter with system size (constant versus linear) can be used to identify the spin glass phase.

After averaging, these quantities S_A, O depend only on the parameters of the circuit ensemble p, r .

2.2 Phase Diagram

We begin by analyzing several cross-sections of the phase diagram.

First consider the $p = 1$ cross section (circuits with measurement only). For $r = 1$ (ZZ measurement only), the final state has random $Z_i Z_{i+1} = \pm 1$ for each pair of qubits and is thus a random cat state described above (due to the Ising symmetry). The other extreme $r = 0$ yields random paramagnetic product states. Both spin glass and trivial phases are perturbatively stable to competing measurements respecting the Ising symmetry. For example, an X measurement on a single qubit j of a cat state will disentangle the qubit and leave the remaining system in a cat state; this is because the stabilizers $Z_{j-1} Z_j, Z_j Z_{j+1}$ become $Z_{j-1} Z_{j+1}, X_j$ after the measurement and the cat heals across j . Note that the Ising symmetry is essential here; a Z measurement on a single qubit of a cat state would collapse it into a product state.

This ensemble of measurement only circuits has a duality between ZZ, X measurements that is manifest after performing a Jordan-Wigner mapping from spins to Majorana modes.

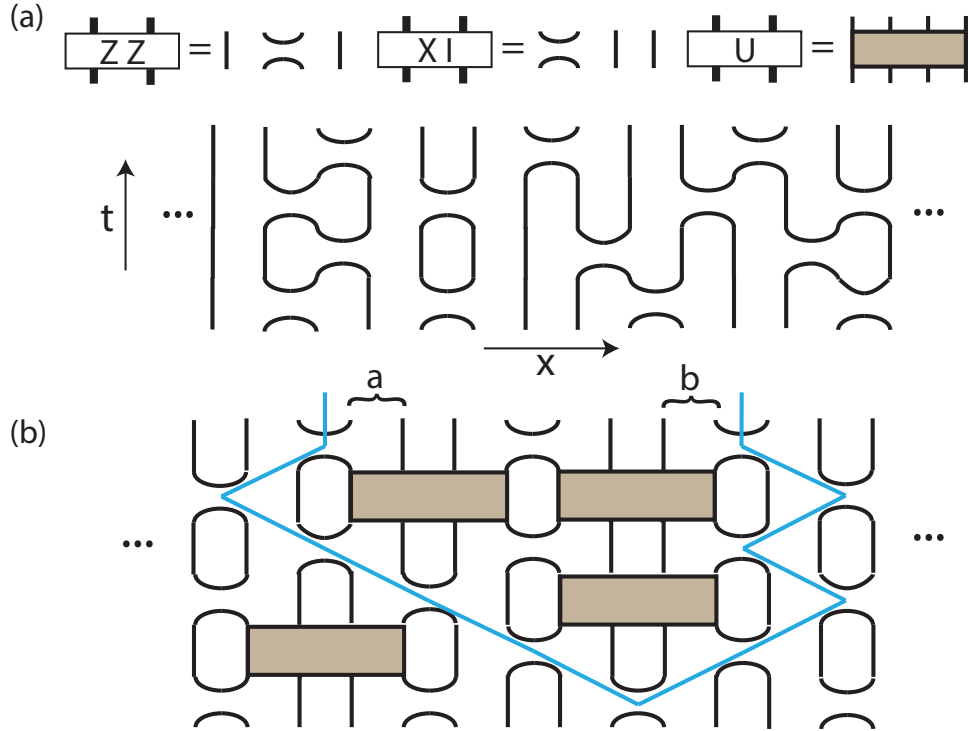


Figure 2.2: (a) The 2-qubit measurements are fermion parity measurements (denoted by the pair of arcs) on the 4 corresponding Majorana modes. The 2-qubit unitary acts locally on the 4 modes because it preserves fermion parity. A circuit with only measurements maps to loops of Majorana worldlines, as noted in [5]. (b) A circuit with only ZZ measurements and unitaries, and the minimal cut (blue line) for an interval with endpoint qubits (a, b) . A minimal cut in the area law phase also mediates spin glass correlation between a, b via the ZZ measurements traversed.

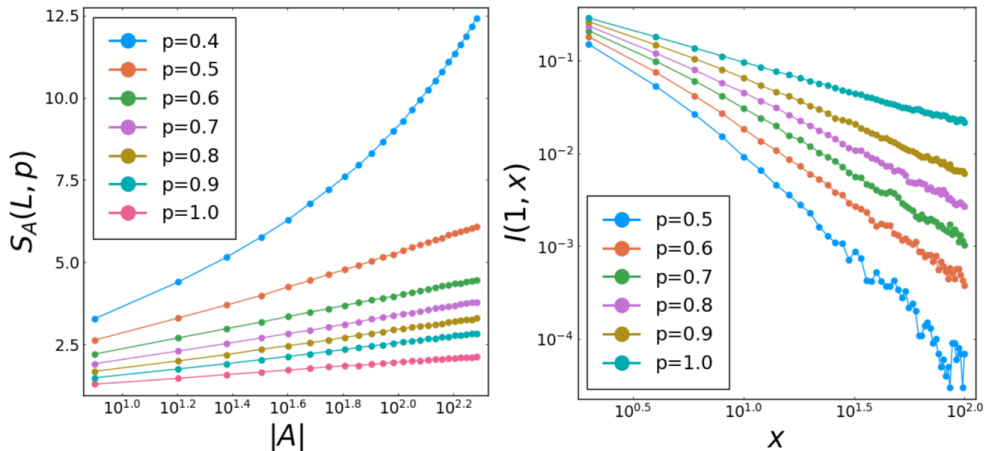


Figure 2.3: $r = 0.5$ cross section (equal probability for ZZ and X measurements). (left) Entanglement entropy versus log of partition size, for various p . (right) Mutual information decay in log-log plot. Total system size is $L = 768$.

In the latter representation, each spin corresponds to two Majorana modes, and in the resulting Majorana chain, the two types of measurement correspond to fermion parity measurements between pairs of Majoranas on even and odd bonds (Fig. 2.2a). The duality fixes a phase transition between spin glass and paramagnetic phases at $r = 0.5$, and this critical point in the Majorana representation is explicitly described by a 2d classical loop model at its corresponding critical point; this mapping was detailed in [5]. See Fig. 2.2a for an example of loops arising from Majorana worldlines.

Next, we consider the cross section with fixed $r = 0.5$ and variable p . Remarkably, we find (Fig. 2.3) that in the range $p \in [0.5, 1]$, the entanglement scales with subsystem size as $S_A = c(p) \log |A|$, with coefficient increasing continuously from $c(p = 1) \approx 0.27$ (consistent with the loop model prediction $\sqrt{3}/2\pi$ [38]). For $p < 0.5$, the entanglement exhibits volume law scaling. We also compute the mutual information $I(a, b) = S_a + S_b - S_{a \cup b}$ between two qubits a, b and find that in the critical regime, I decays as a power law with $|b - a|$; the power also varies continuously with p .

Another important cross section is $r = 1.0$ and variable p , in which unitaries compete with exclusively ZZ measurements. We find evidence of a critical point at $p_c \approx 0.38$, in which there is a simultaneous transition from a spin glass area law phase above p_c to a paramagnetic volume law phase below p_c . This is supported by Fig. 2.4, which depicts a transition of entanglement scaling from area to volume law at $p_c \approx 0.38$ and a transition of spin glass order parameter from linear scaling with L to constant scaling at

$p_c \approx 0.39$ (the two points are within numerical error). It is evident from the figures that both entanglement and order parameter exhibit log scaling at the critical point and scaling collapse near the critical point:

$$\begin{aligned} S_{L/4}(L, p) - S_{L/4}(L, p_c) &= F((p - p_c)L^{1/\nu_S}) \\ O(L, p) - O(L, p_c) &= G((p - p_c)L^{1/\nu_O}) \end{aligned} \tag{2.3}$$

with $\nu_S \approx 1.3, \nu_O \approx 1.5$. The critical exponent $\nu_S \approx 1.3$ is comparable to the value $(4/3)$ expected for the percolation transition in two dimensions.

Some intuition for this phase transition can be obtained from the Majorana representation, in which a two-qubit unitary acts locally on the four corresponding Majoranas because the unitary respects the Ising symmetry (fermion parity). In particular, the symmetric 2-qubit Clifford gate is generated by (non-interacting) Majorana swap operations and (interacting) multiplication by the local fermion parity (see Appendix B.1). As suggested in [39], it is helpful to consider a minimal cut picture which yields the final state's zeroth Renyi entanglement entropy for an interval with endpoints at qubits a, b . We expect the latter to be proportional to the minimum number of unitaries cut by a curve through the circuit with endpoints fixed to be a, b at the final time slice (see Fig. 2.2b). Within this picture, the area-law S_0 phase corresponds to minimal cuts which pass through a constant number of unitaries as $|b - a| \rightarrow \infty$. Though the minimal cut picture is only strictly valid for the zeroth Renyi entropy of a circuit with Haar random unitaries, we use it as a heuristic for understanding the transition in the Clifford circuit.

Such a minimal cut in the area law phase also implies that the spin glass correlation $\langle Z_a Z_b \rangle^2$ is constant as $|b - a| \rightarrow \infty$, yielding a long-range spin glass. This arises from the product of ZZ s from the measurements along the minimal cut, which is attenuated by only a constant number of unitaries traversed by the cut. The ZZ correlation begins with the bottom two qubits of the minimal cut, and as the next measurements along the minimal cut are performed, the pair of qubits which are correlated propagates outward in both directions until it reaches a, b .

Hence, the minimal cut links the area law phase and spin glass order, at least for $r = 1$. A minimal cut through only a constant number of unitaries is no longer possible when the unitary cluster percolates. Hence, we expect that the area law spin glass is destroyed near the site percolation threshold of the square lattice 0.59. Our numerical results indicates $1 - p_c \approx 0.62$, which is close to the value 0.59 given by the minimum cut picture.

A useful probe of the critical point is the mutual information between two antipodal intervals A, B of equal size $|A|$ (see Fig. 2.5). In previous studies without a global symmetry, including both Haar and Clifford random circuits, the mutual information scales as

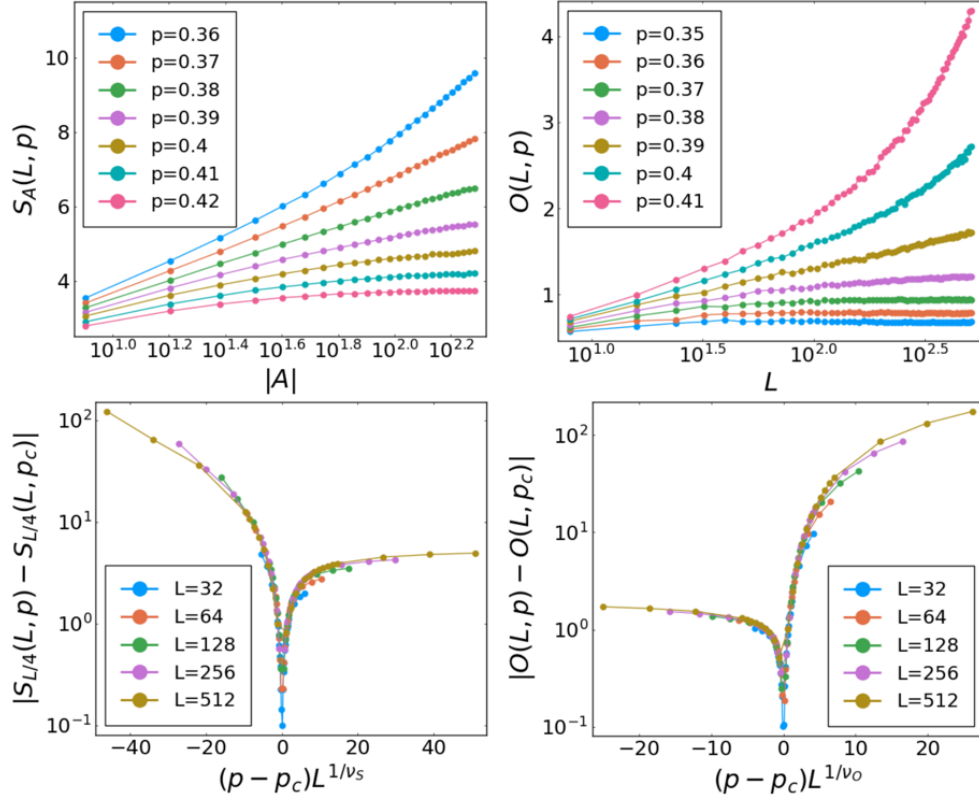


Figure 2.4: $r = 1$ cross section (unitaries and only ZZ measurements with probability p). (top) Entanglement entropy versus log of partition size for total system size $L = 768$ and spin glass order parameter versus log of system size, for various p . At $p_c \approx 0.38, 0.39$, the two exhibit log scaling. (bottom) Scaling collapse of both quantities with $\nu_s \approx 1.3, \nu_o \approx 1.5$.

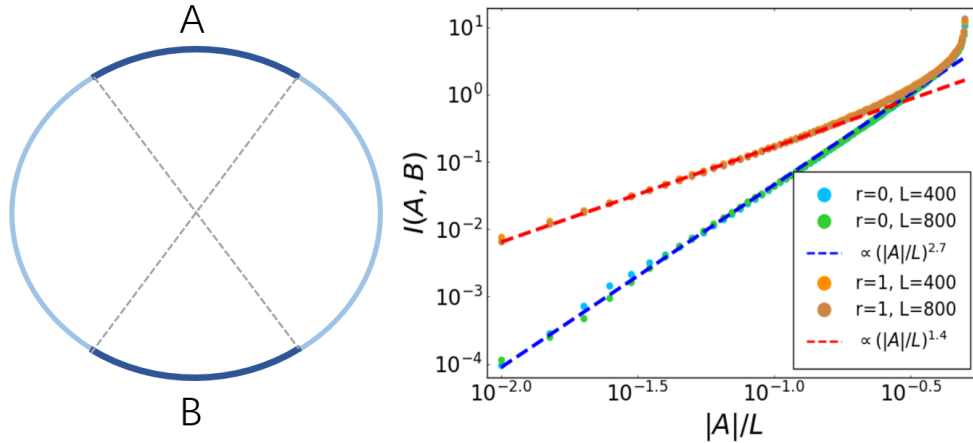


Figure 2.5: (left) Antipodal geometry. Intervals A and B are of the same size and centered on two antipodal points of the periodic qubit chain of length L . (right) Simulated mutual information $I(A, B)$ as a function of the ratio $|A|/L$ at critical points corresponding to $r = 0$ (Z_2 -Clifford unitaries + X measurement) and $r = 1$ (Z_2 -Clifford unitaries + ZZ measurement).

$I_{A,B} \propto (|A|/L)^4$ [40, 39] in the regime of $(|A|/L) \ll 1$. In contrast, in our symmetric monitored circuit, at the spin glass area-law to paramagnetic volume-law transition described above, we find $I_{A,B} \propto (|A|/L)^{1.4}$. Moreover, in the $r = 0$ cross section (which involves X measurement only), there is a direct transition between paramagnetic area-law and paramagnetic volume-law, at which we find $I_{A,B} \propto (|A|/L)^{2.7}$ (Fig. 2.5). These indicate that the entanglement transitions in the presence of a global symmetry are in distinct universality classes than those without symmetry.

The full phase diagram is presented in Fig. 1 and obtained from both cross sections presented. The shaded central portion is a critical regime including the segment of the $r = 0.5$ cross section discussed earlier, with logarithmic entanglement scaling in our current system sizes. One possibility is that the segment at $r = 0.5$ closely borders two phase boundaries and thus appears critical in finite systems. However, both the large range of the log scaling observed ($p \in [0.5, 1]$) as well as the sharp transition from log to volume law scaling (Fig. 2.3) (as opposed to a smooth crossover) are surprising. In short, the critical phase in the thermodynamic limit either (1) persists as a critical phase (2) disappears, resulting in two critical lines separating volume law from paramagnetic and spin glass or (3) disappears, resulting in three critical lines meeting at a point.

For understanding the critical regime, one may consider loop models with crossings

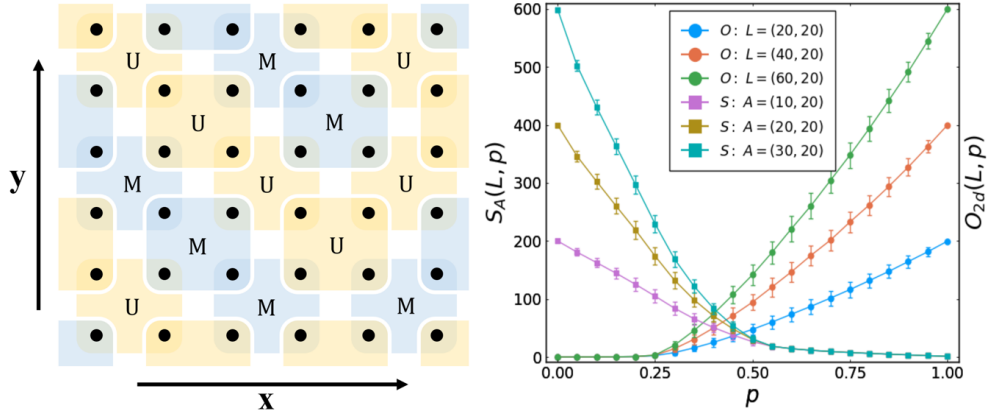


Figure 2.6: (left) A cross section of the $(2+1)d$ circuit architecture. Black dots are qubits and each colored square denotes an operation acting on qubits within the square. An operation is either a random Ising-symmetric 4-qubit Clifford gate (yellow) or a series of 3 two-qubit measurements Z_1Z_2, Z_2Z_3, Z_3Z_4 (blue), with probability $1 - p$ or p . The circuit alternates between the background and foreground, which consist of two distinct partitions into sets of four. (right) The two order parameters $O(L, p)$ and $S_A(L, p)$ as functions of p . For the simulation of $S_A(L, p)$ the total system size is fixed to be $L = (L_x, L_y) = (60, 20)$.

[41, 42, 43, 44, 45, 46, 47, 48] as toy models for our monitored circuit. As mentioned, the $r = 0.5, p = 1$ critical point is described by non-intersecting loops, and loop crossings represent unitaries which swap Majoranas; these serve as bottlenecks in the circuit/loop configuration which lengthen the minimal cut and increase entanglement. Interestingly, for finite crossing probability, loop models have a critical “Goldstone phase” [41, 42, 43, 44, 45, 46, 47, 48], referring to a sigma model description in the continuum. Indeed, the phase diagram in [41] bears much similarity to ours, and it would be interesting to understand in detail the connection. This Goldstone phase has also been discussed in the context of entanglement transitions in random tensor networks [49].

2.3 Higher dimensions and other architectures

In contrast to one dimension, higher-dimensional circuit architectures allow for the possibility that both measurement and unitary clusters can percolate in a parameter range. In such a range, the final state consists of an extensive subset of spins connected in the past by a measurement cluster, enabling spin-glass order. On the other hand, the percolating

unitary cluster may intersect a minimal surface an extensive number of times, leading to volume law entanglement scaling.

This can be verified by simulating a generalization of our architecture to a two-dimensional system using the generalized order parameter

$$O_{2d}(L, p) = \frac{1}{L_x L_y} \sum_{\mathbf{m}i, \mathbf{m}j} \langle \psi | Z_{\mathbf{m}i} Z_{\mathbf{m}j} | \psi \rangle^2 - \langle \psi | Z_{\mathbf{m}i} | \psi \rangle^2 \langle \psi | Z_{\mathbf{m}j} | \psi \rangle^2 \quad (2.4)$$

The left panel of Fig. 2.6 shows a temporal cross-section of our $(2+1)d$ circuit; the circuit alternates between the background and foreground, which involve two distinct partitions into sets of 4-qubit operations. Each operation is, with probability $1 - p$ or p , either a random 4-qubit Clifford gate commuting with $X_1 X_2 X_3 X_4$, or 3 consecutive measurements in bases $Z_1 Z_2$, $Z_2 Z_3$ and $Z_3 Z_4$. Our result (right panel of Fig. 2.6) shows that the entanglement transition and the spin glass transition respectively happen at $p_{c,S} \approx 0.5$ and $p_{c,O} \approx 0.25$. The parameter range between them corresponds to a volume-law, spin-glass-ordered phase.

We expect that replacing symmetric Clifford with symmetric Haar random unitaries will not change the qualitative aspects of the phase diagrams. The stability of the ordered phase derives from the inability of finite depth circuits to destroy the order, and this holds for any symmetric unitary circuit.

Furthermore, the monitored circuits considered in the literature can also support spin glass order, after a small but important modification. Such circuits are brick walls of operations that have probability $1 - p$ of being a random unitary and probability p of being a projective measurement followed by a random unitary, and previous work has considered this setup with ZZ measurements as the projective measurement [50]. However, both the fact that a unitary is *always* applied, even after a measurement is made, and the fact that each measurement layer was restricted to either even bonds or odd bonds of qubits [50], implies that the measurement basis is irrelevant and no spin-glass order can exist.

Consider a very similar setup in which random unitaries are always applied in a brick wall pattern, but between each layer of unitaries, ZZ measurements on *any* neighboring qubits are performed with probability p (see Fig. 2.7). In this case, for large p , connected clusters of ZZ measurements are performed, and the subsequent (single) layer of unitaries cannot destroy the spin-glass order as long as the Lieb-Robinson length is shorter than the typical measurement cluster size. As before, it is essential that each random unitary respect the global Ising symmetry.

We find that the volume law phase persists up to $p \approx 0.52$ and the spin glass order begins at $p \approx 0.58$. Based on our numerics, the interval between these points appears to

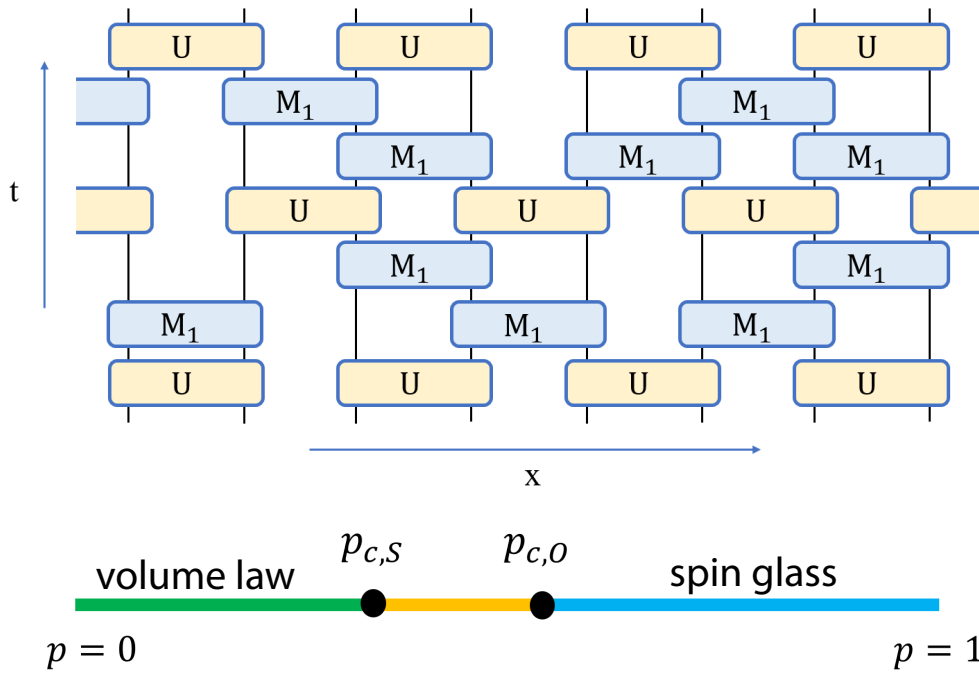


Figure 2.7: Alternative class of circuits with Z_2 -symmetric random unitaries always applied in brick-wall fashion, with in-between layers of $M_1 = Z_i Z_{i+1}$ measurements for every i , each applied with probability p . Phase diagram has a paramagnetic volume law phase, a critical regime, and spin glass area law phase. $p_{c,S} \approx 0.52, p_{c,O} \approx 0.58,$.

be critical (entanglement scaling is not strictly area or volume law), but we cannot rule out finite size effects masking a direct transition between the two phases. Nonetheless, the existence of the spin glass phase is unambiguous.

2.4 Discussions and outlook

The measurements in the monitored circuit can be generalized to stabilize other types of quantum order. For example, measurements of the (commuting Pauli) operators in the toric code Hamiltonian [51] would stabilize a random topologically ordered state. One could use the same type of order parameter as Eq. (2.2), with the Z operator replaced by a string operator (one of the Wilson lines). In contrast to the spin glass order, the unitaries in this monitored circuit need not respect any global symmetry for the stability of topological order.

The use of measurements to protect against random operations also forms the basis of active quantum error correction. An important difference is that active quantum error correction seeks to reverse errors by applying operations depending on the error syndromes are obtained. In contrast, in our setup, while the measurement operations are essential, their outcomes are not important (our scheme has no feedback). This is because the protocol does not preserve a particular quantum state but instead a particular long-range entanglement structure. Hence the name measurement protected quantum *phases*.

Nonetheless, it would be interesting to incorporate conditioning on measurements. More generally, can the hybrid unitary and measurement circuits lead to new quantum orders beyond the critical points? And how can these new universality classes with symmetry be understood? We leave these explorations for the future.

Chapter 3

Information dynamics in weakly monitored quantum circuits

In this chapter, we study behavior of the weakly monitored phase well before the equilibrium is reached. Specifically, we consider the following two complementary aspects of entanglement dynamics.

- (a) How does the entanglement structure evolve with time starting from an unentangled (maximally mixed or pure product) initial state?
- (b) How does the monitored dynamics spread and forget the input information?

Our main findings are summarized as follows.

3.1 Main results

Entanglement dynamics: In Sec. 3.2, we study how the entanglement structure of a trajectory state $\rho_{\mathbf{m}}(t)$ evolves with time until its saturation.

Stabilizer growth: We start by considering the dynamics with a maximally mixed initial state. The length distribution of the stabilizer generators provides an informative proxy for the underlying entanglement structure. In Sec. 3.2.1, we find that the evolution of stabilizer length distribution takes the following form:

$$h(\ell, t) \simeq \frac{e^{-\ell/\ell^*(t)}}{\ell^{5/3}}, \quad (3.1)$$

with a time-dependent soft cutoff $\ell^*(t)$ which exhibits a super-linear growth:

$$\ell^*(t) \propto t^{\frac{3}{2}}, \quad (3.2)$$

indicating that there is a small fraction of stabilizers that grows super-linearly with time, as conjectured in [52].

Entanglement growth: The fast-growing stabilizers leave important imprints on $\rho(t)$'s entanglement evolution. In Sec. 3.2.3, we show that they can be detected by a tripartite entanglement measure, namely the conditional mutual information:

$$I_{A:B|C} \equiv S_{AC} + S_{BC} - S_{ABC} - S_C, \quad (3.3)$$

where A and B are two regions separated by another large region C . We show that $I_{A:B|C}$ exactly measures the number of nonlocal stabilizer generators connecting A and B . Eq. (3.1) then implies that $I_{A:B|C}$ starts to take non-zero values at a time scale

$$t^* \simeq \text{dist}(A, B)^{\frac{2}{3}}; \quad (3.4)$$

which suggests that, at time t , non-trivial entanglement at the distance scale of $O(t^{3/2})$ will be generated.

Code growth: The super-linear growth of entanglement naturally gives rise to a new sublinear time scale of $O(L^{2/3})$ when the cutoff $\ell^*(t)$ reaches the system size L . In Sec. 3.2.4, we argue that the $O(L^{2/3})$ time scale coincides with the encoding time of a monitored circuit when it is regarded as a dynamically generated quantum error-correcting code whose code subspace is supported on $\rho(t)$. Furthermore, we show that the $\rho(t)$'s (contiguous) code distance grows as

$$d_{\text{code}} \propto t^{\frac{1}{2}}, \quad (3.5)$$

until it reaches its steady value $\simeq O(L^{1/3})$ [30], which occurs at $t \simeq O(L^{2/3})$.

Pure initial state: In Sec. 3.2.6, we extend the discussion to the dynamics starting from a pure initial state. We find that the entanglement dynamics is qualitatively similar to that of unitary-only dynamics and does not display any super-linearly growing length scale.

Information dynamics: In Sec. 3.3, we switch our attention from an evolving trajectory state $\rho(t) \propto C(t)\rho_0 C^\dagger(t)$ to the circuit itself and study the fate of initially local information. To quantify information spreading, we introduce a reference system R which is initially maximally entangled with the physical qubits in the circuit, referred to as P (Fig. 3.6). After acting the monitored dynamics on P for time t , we use the following

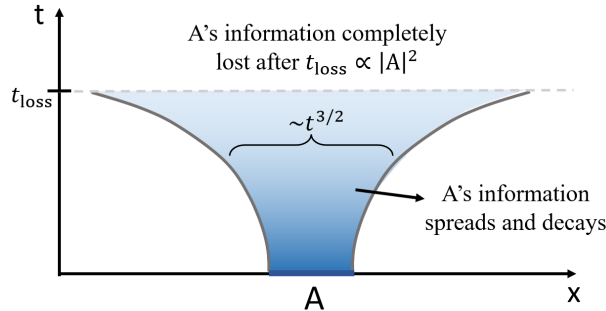


Figure 3.1: An illustration of the spreading and decay of local information.

quantity to measure how much information within region A_P at input is detectable within region B_P at output:

$$I_{A_R:B_P}(t) \equiv S_{A_R}(t) + S_{B_P}(t) - S_{A_R \cup B_P}(t), \quad (3.6)$$

where A_R is the part of the reference system corresponding to A_P .

In Sec. 3.3.2, we show that any Clifford monitored dynamics can be treated as a map between two quantum code spaces. We introduce the notion of *logical operator transferring*, which is a natural generalization of operator evolution in unitary dynamics. Furthermore, we show that $I_{A_R:B_P}(t)$ exactly counts how many logical operators are transferred from region A to the region B by the dynamics $C(t)$ (Thm.1).

Then we focus on the behavior of information spreading in a monitored circuit. Our findings are graphically illustrated in Fig. 3.1. Roughly, local information undergoes a combination of two types of dynamics, decay and spreading, as summarized in the heat map.

Decay of local information: Measurements can destroy the input information. In Sec. 3.3.4, we show that the information within an interval A will be completely destroyed at a time scale:

$$t_{\text{loss}} \propto |A|^2, \quad (3.7)$$

with $I_{A_R:P}(t) = 0$ for $t > t_{\text{loss}}$. In fact, this relation is fundamentally equivalent to Eq. (3.5) due to a statistical time-reversal symmetry of the dynamics, as further discussed in Sec. 3.3.4.

Spreading of local information: Before the time t_{loss} , local information gradually delocalizes. In Sec. 3.3.5, we numerically find that the remaining part of initially local information

is contained within a region of the size

$$D(t) \propto t^{\frac{3}{2}}. \tag{3.8}$$

This super-ballistic information spreading again originates from the nonlocal effects of measurements. We also confirm that it is ballistic in unitary circuits.

Initial state dependence: In Sec. 3.3.6, we discuss how the behavior of information spreading changes if we fix a part of the input state. Specifically, we consider the setting where only a subsystem $A \subseteq P$ is considered as the *variable* input, while the rest of the system $A^c = P - A$ has a *fixed* initial state. We find that the spreading of A 's information depends on the choice of the initial state for A^c . Namely, if A^c is initially in a pure product state, then the spreading becomes linear instead of super-linear.

Comparison with DRPE: In Sec. 3.4, we discuss the relation between our results and the statistical mechanics of directed polymers in random environment (DRPE), an effective theory recently proposed for the entanglement dynamics in weakly monitored circuits [26]. We demonstrate that some of our results can be derived using DPPE, while the rest are numerically consistent with DPPE.

3.2 Entanglement Dynamics

In this section, we study the dynamics of the stabilizer length distribution in weakly monitored circuits and then discuss its implications for the evolving state's entanglement structure and the contiguous code distance growth. We will also discuss the initial state dependence of these properties.

3.2.1 Stabilizer length distribution in clipped gauge

An L -qubit stabilizer state ρ , associated with a set of mutually commuting Pauli operators (dubbed stabilizers) $\mathcal{S} = \{g_1, g_2, \dots, g_m\}$, is defined as:

$$\rho = \frac{1}{2^L} \sum_{g \in G} g, \tag{3.9}$$

where $G = \langle \mathcal{S} \rangle$ is the stabilizer group: the Abelian group generated by all possible products of the operators in \mathcal{S} . If $m = L$, then the state ρ will be a pure state.

Since two different sets of stabilizer generators could generate the same stabilizer group, there is a gauge degree of freedom in choosing \mathcal{S} for a given state ρ . When the qubits are arranged in a 1D chain, there is a gauge choice called *clipped gauge* [53, 25], that is particularly suitable for studying the entanglement structure. The clipped gauge is defined as follows. We denote the left endpoint and right endpoint of each generator $g \in \mathcal{S}$, a Pauli string operator, as $l(g)$ and $r(g)$. We say \mathcal{S} is in the clipped gauge if the following two conditions are satisfied:

- $|\{g \in \mathcal{S} : l(g) = i\}| + |\{g \in \mathcal{S} : r(g) = i\}| \leq 2 \quad \forall i$;
- if one of the two terms above equals 2, then two left (or right) endpoints at position i must be different Pauli operators.

For any stabilizer state ρ , a clipped-gauged \mathcal{S} always exists, but may not be unique. However, the set of end-points pairs defined below is unique

$$\mathcal{B}(\rho) \equiv \{(l(g), r(g)) : g \in \mathcal{S}\}. \quad (3.10)$$

See the appendix of Ref. [25] for details.

The clipped gauge and the set \mathcal{B} are particularly useful for studying the entanglement structure. Specifically, for any contiguous region A , we have [25, 53]:

$$S_A = |A| - |\{g \in \mathcal{S} : \text{supp}(g) \subseteq A\}|; \quad (3.11)$$

where $\text{supp}(g)$ is the interval $[l(g), r(g)]$. Therefore for two neighboring contiguous regions A and B ,

$$\begin{aligned} I_{A:B} &\equiv S_A + S_B - S_{AB} \\ &= |\{g \in \mathcal{S} : l(g) \in A, r(g) \in B\}|. \end{aligned} \quad (3.12)$$

Namely, for questions involving contiguous regions only, clipped-gauged stabilizer generators can be thought of as “generators of entanglement” where entanglement across a cut is proportional to the number of bridging generators.

Even when A and B are not neighboring, a certain useful entanglement measure can be explicitly computed. Suppose that A and B are separated by some interval C . Using Eq. (3.11) four times, we find that the conditional mutual information is given by

$$\begin{aligned} I_{A:B|C} &\equiv I_{A:BC} - I_{A:C} \\ &= S_{AC} + S_{BC} - S_{ABC} - S_C \\ &= |\{g \in \mathcal{S} : l(g) \in A, r(g) \in B\}|. \end{aligned} \quad (3.13)$$

This relation tells us $I_{A:B|C}$ directly measures the sizes of the stabilizers. Namely, the number of long stabilizers starting from A and ending in B exactly equals the conditional mutual information.

Returning to the setting of (1+1)D monitored quantum circuits, for the evolving stabilizer state $\rho(t)$, we define its stabilizer length distribution as:

$$h(\ell, t, x) = |\{g \in \mathcal{S}(\rho(t)) : \text{len}(g) = \ell, \text{mid}(g) = x\}|, \quad (3.14)$$

where $\mathcal{S}(\rho(t))$ is a clipped-gauged set of generators for $\rho(t)$, while $\text{len}(\cdot)$ and $\text{mid}(\cdot)$ are defined as:

$$\begin{aligned} \text{len}(g) &= r(g) - l(g) + 1 \\ \text{mid}(g) &= \left\lfloor \frac{r(g) + l(g)}{2} \right\rfloor. \end{aligned} \quad (3.15)$$

Evidently, $h(\ell, t, x)$ only depends on $\mathcal{B}(\rho(t))$, thus is well-defined for a given $\rho(t)$. In the thermodynamic limit $L \rightarrow \infty$, the distribution should be independent of x as the dynamics is statistically translational invariant. In numerical simulations where system size is always finite, we expect this to still be the case, especially when the typical stabilizers' endpoints $x \pm \ell/2$ are far from the system's boundary. We omit the x dependence of h from now on.

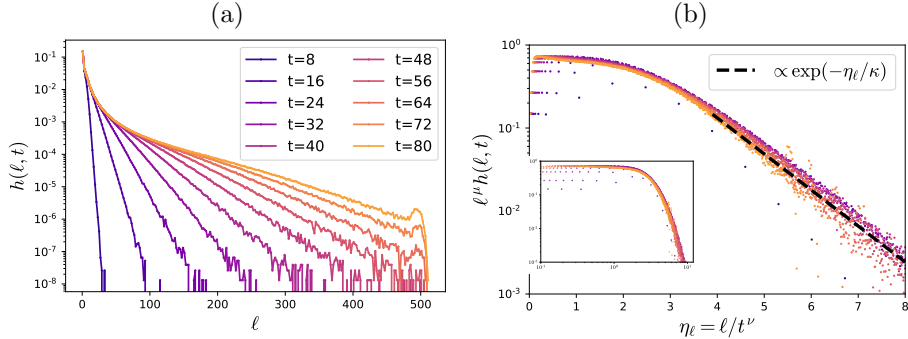


Figure 3.2: (a) Stabilizer length distribution $h(\ell, t)$ in an $L = 512$ circuit with open boundary condition. (b) The same data after rescaling the x and y axes by $t^{-\nu}$ and t^μ , respectively. The inset shows the same plot on a log-log scale.

We now study how the distribution evolves with time before the system reaches steady states with a maximally mixed initial state $\rho(0) = \frac{1}{2^L} \mathbb{I}$. The simulation result, shown in Fig. 3.2(a), leads us to the following scaling form for $h(\ell, t)$:

$$h(\ell, t) = c(\ell/\ell^*(t)) \frac{e^{-\ell/\ell^*(t)}}{\ell^\mu}, \quad (3.16)$$

with $c(x)$ is a slow varying function that takes non-vanishing $O(1)$ value for any $x \in (0, \infty)$. Namely, below the length scale $\ell^*(t)$, the distribution has an equilibrium form that possesses a time-independent power-law tail. On the other hand, above the length scale $\ell^*(t)$, the distribution exhibits an exponential tail, indicating that stabilizer generators of size larger than $\ell^*(t)$ are extremely rare and are essentially negligible.

Furthermore, we find that the cutoff $\ell^*(t)$ grows according to a power law in time:

$$\ell^*(t) \propto t^\nu. \quad (3.17)$$

This observation, together with the validity of the scaling form in Eq. (3.16), is reflected by the data collapse of $h(\ell, t)$ at different time t , shown in Fig. 3.2(b). The best collapse is given by $\mu = 1.66$ and $\nu = 1.5$, telling us that $\ell^*(t) \propto t^\nu$ grows super-linearly with time. As we will discuss later in Sec. 3.4, these results are consistent with the domain-wall picture which predicts $\mu = \frac{5}{3}$ and $\nu = \frac{3}{2}$.

These results suggest that a small but non-negligible fraction of stabilizer generators will grow super-linearly, namely $\sim t^{3/2}$. We will later demonstrate that these fast-growing stabilizer generators can be indeed detected by a multipartite entanglement measure, namely the conditional mutual information $I_{A:B|C}$.

3.2.2 Entropy of a contiguous region

We have seen that the distribution $h(\ell, t)$ possesses a super-linear length scale $\ell^*(t) \propto t^\nu$. Given the close relation between $h(\ell, t)$ and the $\rho(t)$'s entanglement structure, we expect the length scale to leave some imprint on the $\rho(t)$'s entanglement structure. In this subsection we analyze the simplest case: the entanglement entropy S_A of a contiguous subsystem A .

Recalling that the stabilizer distribution $h(\ell, t)$ contains information about $\rho(t)$'s entanglement structure Eq. (3.11), we have:

$$\begin{aligned} S_A(t) &\equiv |A| - |\{g \in \mathcal{S} : \text{supp}(g) \subseteq A\}| \\ &= |A| - \sum_{\ell=1}^{|A|} (|A| - \ell) h(\ell, t) \\ &\approx |A| - \int_a^{|A|} (|A| - \ell) h(\ell, t) d\ell. \end{aligned} \quad (3.18)$$

In the last (approximate) equality, we introduced a UV cutoff $a = O(1)$ in order to regularize the integral.

To build some intuition, let us begin by studying late-time cases with $\ell^*(t) \gg |A|$. Then, the distribution $h(\ell, t)$ in the above integral is proportional to $\ell^{-\mu}$. Performing the integral, we find that the entanglement entropy S_A approaches to the following steady form for $t \gg |A|^{1/\nu}$:

$$S_A \approx b_1|A| + b_2|A|^{2-\mu}, \quad (3.19)$$

where $b_1, b_2 \geq 0$ are some constants. Hence, we find that the entanglement entropy consists of the leading volume-law term as well as a sub-leading correction proportional to $|A|^{2-\mu}$ with $2-\mu \approx \frac{1}{3}$. Furthermore, we find that the saturation time $t \sim |A|^{1/\nu} \approx |A|^{\frac{2}{3}}$ is sublinear.

Next, let us turn our attention to the early time cases with $\ell^*(t) \ll |A|$. The scaling behavior of the integral can be analyzed by approximating the distribution $h(\ell, t)$ as $\ell^{-\nu}$ with a cutoff at $\ell^*(t)$, which leads to the following result for $t \ll |A|^{1/\nu}$:

$$S_A \approx b_1|A| + b_2^{(1)}|A|\ell^*(t)^{-(\mu-1)} + b_2^{(2)}\ell^*(t)^{2-\mu}, \quad (3.20)$$

with some constants $b_1, b_2^{(1)}, b_2^{(2)} > 0$.

Here it is worth looking at the dynamical aspect of each term. The first term obviously represents the time-independent volume-law contribution which survives at late times as well. As for the second term, we notice that it is proportional to $|A|$, and hence contributes to the volume-law entanglement. As t increases, however, the second term becomes smaller, reducing the volume-law contribution. Explicitly, the second term decays as

$$b_2^{(1)}|A|\ell^*(t)^{-(\mu-1)} \sim c_1|A|t^{-\nu(\mu-1)} \quad (3.21)$$

until it becomes order of $|A|^{2-\mu}$ at $t \sim |A|^{1/\nu}$. Here it is natural to interpret this decay as the loss of the volume-law entanglement due to projective measurements in the bulk of the interval. As for the third term, it is initially zero, and then grows as

$$b_2^{(2)}\ell^*(t)^{2-\mu} \sim c_2t^{\nu(2-\mu)} \quad (3.22)$$

until it becomes order of $|A|^{2-\mu}$ at $t \sim |A|^{1/\nu}$. Since it does not depend on $|A|$, it is natural to interpret this growth as the creation of entanglement due to projective measurements followed by unitary evolution.

Plugging $\mu = \frac{5}{3}$ and $\nu = \frac{3}{2}$ in, we obtain the following behavior for S_A when $\ell^*(t) \ll |A|$:

$$S_A \approx (b_1 + c_1t^{-1})|A| + c_2t^{\frac{1}{2}}. \quad (3.23)$$

It is worth emphasizing that, while both the c_1 and the c_2 terms eventually contribute the sub-leading terms $|A|^{1/3}$ at saturation when $t \sim |A|^{2/3}$, their origins are of different nature. It is also useful to note that the subleading term in the above equation implies that the mutual information $I_{A:B}$ between small neighboring regions A, B grows sublinearly as $t^{1/2}$ at early time, which is consistent with an observation from [26].

The time dependence of $S_A(t)$ at any time scale can also be studied by explicitly performing the integral Eq. (3.16). Since $c(x)$ takes $O(1)$ values throughout $x \in (0, \infty)$, its specific form does not change any scaling behavior of our interest. Hence, by setting $c(x) = 1$, we obtain:

$$S_A = b_1(a)|A| + b_2(\eta)|A|^{2-\mu} + o(a, |A|^0), \quad (3.24)$$

with

$$\begin{aligned} \eta &= |A|/t^\nu, \\ b_1(a) &= 1 + a^{1-\mu}/(1-\mu), \\ b_2(\eta) &= \eta^{\mu-1}\Gamma(1-\mu, 0, \eta) + \eta^{\mu-2}\Gamma(2-\mu, 0, \eta), \end{aligned} \quad (3.25)$$

where $\Gamma(z, x_1, x_2) = \int_{x_1}^{x_2} s^{z-1} e^{-s} ds$ is the generalized incomplete gamma function. The key observation is that the time-dependent part $b_2(\eta)|A|^{2-\mu}$ depends on t and A only through the ratio $\eta = |A|/t^\nu$.

3.2.3 Multipartite entanglement generation

We have observed that the stabilizer size distribution grows super-linearly and leaves some imprints on the sub-leading behavior of S_A for a contiguous subsystem A . These contributions, however, are often hidden in the sub-leading terms, and are not manifest in simple bipartite entanglement measures. In this section, we probe the super-linear stabilizer growth using multipartite entanglement measures.

The underlying difficulty in detecting the super-linear stabilizer growth is the absence of bi-partite entanglement in a weakly monitored circuit. Namely, the mutual information $I_{A:B}$ for two distant subsystems A, B remains almost zero at any time. Here, we begin by presenting a derivation of a universal expression of the mutual information from the stabilizer length distribution.

Let A, C and B be three consecutive intervals, with C separating two disjoint intervals A and B . Recall that the mutual information $I_{A:B}$ is given by

$$I_{A:B} = S_A + S_B - S_{AB}. \quad (3.26)$$

Here, S_A, S_B can be computed from the stabilizer length distributions as A, B are single contiguous regions. However, S_{AB} is the entanglement entropy for a union of two disjoint intervals and cannot be readily computed. [Note that Eq. (3.12) considers the case where A, B are neighboring.]

In order to overcome this difficulty, we shall utilize a stabilizer counting argument combined with a certain probabilistic assumption about the Pauli operator contents of stabilizers [52]. Let $\rho(t)$ be an evolving stabilizer state in a monitored circuit, with G being $\rho(t)$'s stabilizer group. In the stabilizer formalism, the mutual information between A and B is given by:

$$I_{A:B} = \log|G_{AB}| - \log|G_A| - \log|G_B|, \quad (3.27)$$

where G_X is the subgroup of G that only acts non-trivially on the subsystem X .

We now estimate $\log|G_{AB}|$, by assuming that each stabilizer in G_{ABC} has random content within its support. Requiring stabilizers to be identity on C would impose $2|C|$ independent constraints. However, since all stabilizers must commute with each other, in particular with elements in G_C , $\log|G_C|$ constraints are automatically satisfied. Hence, we arrive at the following estimation:

$$\begin{aligned} \log|G_{AB}| &\approx \log|G_{ABC}| - 2|C| + \log|G_C| \\ &= |AB| - S_{ABC} - S_C. \end{aligned} \quad (3.28)$$

The estimation combined with exact formulas for $\log|G_A|$ and $\log|G_B|$ gives rise to an unphysical negative number for $I_{A:B}$ when stabilizers with empty support on C are rare. Taking this case into consideration, we arrive at the following expression for $I_{A:B}$:

$$I_{A:B} \approx \max\{S_A + S_B - S_{ABC} - S_C, 0\}. \quad (3.29)$$

In Sec. 3.4.3 we will present another derivation of it based on the domain-wall picture.

The relation Eq. (3.29) holds regardless of C 's size. In the case of $|C| > |A|, |B|$, recalling that the single interval entropy S_X has a leading term that is linear in $|X|$ at any time, we conclude the first term in $\max\{\cdot\}$ is always negative and $I_{A:B} \approx 0$ at any time.

We now return to the discussions of multipartite entanglement measures and their relation to the sizes of stabilizer generators. The fact that $I_{A:B} \approx 0$ prompts us to consider multipartite entanglement measures. A particularly useful choice is the tri-partite information [54]:

$$I_{A:B:C} \equiv S_A + S_B + S_C - S_{AB} - S_{AC} - S_{BC} + S_{ABC}, \quad (3.30)$$

which is also known as the topological entanglement entropy in studies of topological phases of matter [55]. Roughly, the negativity of $I_{A:B:C}$ implies the presence of quantum entanglement among four subsystems A, B, C and their complement $(ABC)^c$. See [56, 57] for detailed discussions on various properties of $I_{A:B:C}$.

It turns out that, in a weakly monitored circuit, the tri-partite information is equivalent to the conditional mutual information:

$$I_{A:B:C} = I_{A:B} - I_{A:B|C} \approx -I_{A:B|C} \quad (3.31)$$

since $I_{A:B} \approx 0$. This enables us to evaluate $I_{A:B:C}$ using the stabilizer length distribution via Eq. (3.13).

Let us consider two regions A and B separated by a long interval C . For concreteness, we let $|A|=|B|=r|C|$ for some small $r \ll 1$, so that $|C|$ is the only length scale in the problem. Recalling that $I_{A:B|C}$ exactly measures the number of stabilizers that connect A and B , and the longest stabilizer at time t has a size $\ell^*(t)$, we conclude $I_{A:B|C}(t)$ should go from zero to non-zero when $\ell^* \sim |C| \Leftrightarrow t \propto |C|^{2/3}$.

An alternative and more quantitative way is the following. Using Eq. (3.18), we know that $I_{A:B|C}$ must take a form

$$I_{A:B|C}(t) = g(|C|/t^\nu)|C|^{2-\mu}. \quad (3.32)$$

This implies that the time-scale t^* for $I_{A:B:C}$ to develop must be proportional to $|C|^{1/\nu} = |C|^{2/3}$, *i.e.* t^* grows sub-linearly with the A and B 's separation.

Both analyses lead to the conclusion that: A and B start to get entangled in a time scale that is sublinear in their distance $|C|$. We verify this statement numerically by simulating $I_{A:B|C}$ explicitly, as displayed in Fig. 3.3(a). The Fig. 3.3(b) shows the collapse of the simulated $I_{A:B|C}$ according to the scaling form Eq. (3.32), showing the validity of the scale form Eq. (3.32).

3.2.4 Code distance growth

In this subsection, we study the entanglement dynamics from the perspective of quantum error-correcting codes. Namely, we argue that the sublinear time scale $t \sim L^{\frac{2}{3}}$ corresponds to the encoding time of a monitored quantum circuit.

For a stabilizer code ρ , the number of independent logical operators in a region A equals $I_{A:R}(|\rho\rangle)$, where $|\rho\rangle$ is a purification of ρ and R is the reference system [30]. Thus, the code

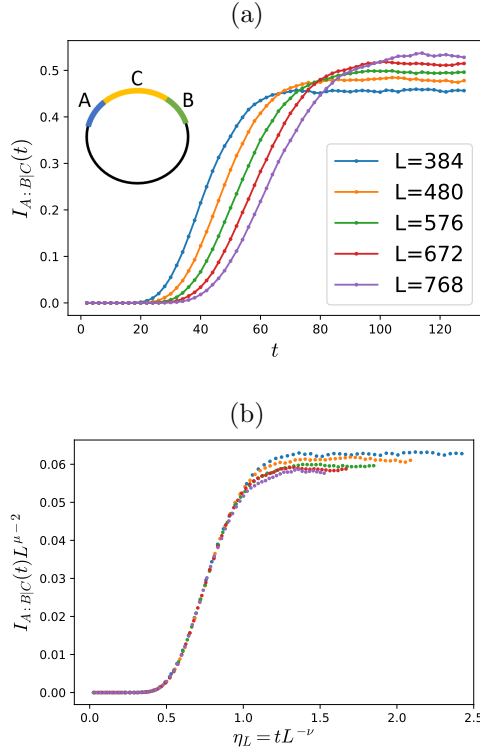


Figure 3.3: (a) Dynamics of conditional mutual information $I_{A:B|C}(t)$, on a periodic spin chain for various L . Inset shows the geometry of A , B and C , whose sizes are $|A|=|B|=\frac{5}{24}|C|=\frac{1}{8}L$ (b) The collapse of $I_{A:B|C}$'s data using the scaling form Eq. (3.32), with $(\mu, \nu) = (1.66, 1.5)$.

distance d_{code} can be expressed as:

$$d_{\text{code}} = \min\{|A| : I_{A:R}(|\rho\rangle) > 0\}. \quad (3.33)$$

In fact, $I_{A:R}(|\rho\rangle)$ can be computed from ρ directly. Denote A^c as the complement of A in the physical system and notice that $|\rho\rangle$ is a pure state on AA^cR . We then have:

$$I_{A:R}(|\rho\rangle) = 2S_A(\rho) - I_{A:A^c}(\rho), \quad (3.34)$$

where the r.h.s. can be determined by the entanglement structure of ρ .

Returning to monitored quantum circuits, recall that the evolving state $\rho(t)$ can be viewed as a stabilizer error-correcting code whose dynamical code space is the subspace where $\rho(t)$ is supported [29, 30]. The (contiguous) code distance d_{code} corresponds to the size of a minimal contiguous subsystem that supports a logical operator.

Let us begin with the equilibrium case with $t \gg L^{\frac{2}{3}}$. It has been shown that d_{code} is closely related to the subleading term of the steady state entanglement entropy in Eq. (3.19). Namely, if $d_{\text{code}} \propto L^{\gamma_{\text{code}}}$, then the entanglement entropy S_A must have a sub-leading term with $|A|^{\gamma_{\text{code}}}$ [52]. Using this observation, we obtain the following relation of scaling exponents:

$$\gamma_{\text{code}} = 2 - \mu \approx \frac{1}{3}, \quad (3.35)$$

which relates the power-law tail of the stabilizer distribution and the code distance. This is consistent with the numerical estimate of γ_{code} from [30, 26].

Next, let us consider the intermediate case with $t \ll L^{\frac{2}{3}}$. Here, we find that the code distance grows as $d_{\text{code}} \sim t^{1/2}$ before it reaches the equilibrium value of $\sim L^{1/3}$ at a time scale $t \sim L^{2/3}$. This can be derived by following an argument from [52]. Namely, we pick two equal-sized contiguous regions B_1 and B_2 to the left and right of A . When $|B_1| = |B_2|$ is sufficiently large, we have $I_{A:A^c} = I_{A:B}$ where $B = B_1 \cup B_2$. By making use of the relation Eq. (3.29), we obtain:

$$\begin{aligned} 2S_A - I_{A:B} &= S_{AB} + S_A - S_{B_1} - S_{B_2} + I_{B_1:B_2} \\ &\approx \max\{0, S_{AB} + S_A - S_{B_1} - S_{B_2}\}. \end{aligned} \quad (3.36)$$

The second term is negative when $|A|$ is small, and it gradually switches to positive values as $|A|$ increases. In this regime, we also have $I_{B_1:B_2} \approx 0$. Thus, the code distance is given by the size of A that satisfies:

$$S_{B_1} + S_{B_2} - S_{AB} - S_A \approx 0. \quad (3.37)$$

Recalling that B_1 , B_2 , and $A \cup B$ are contiguous regions, we can compute their entanglement entropies using Eq. (3.23). When $|A| \ll t^{3/2}$, we find

$$\begin{aligned} &2((b_1 + c_1 t^{-1})|B_1| + c_2 t^{1/2}) \\ &\approx (b_1 + c_1 t^{-1})(2|B_1| + |A|) + c_2 t^{1/2} + b_1 |A| + b_2 |A|^{1/3} \\ \Rightarrow d_{\text{code}} = |A| &\approx \frac{c_2 t^{1/2}}{2b_1 + c_1 t^{-1}} \sim t^{1/2}. \end{aligned} \quad (3.38)$$

We confirmed this scaling numerically, by simulating the following quantity:

$$d_{\text{code},\epsilon}(t) \equiv \operatorname{argmax}_{|A|} (I_{R:A}(t) \leq \epsilon). \quad (3.39)$$

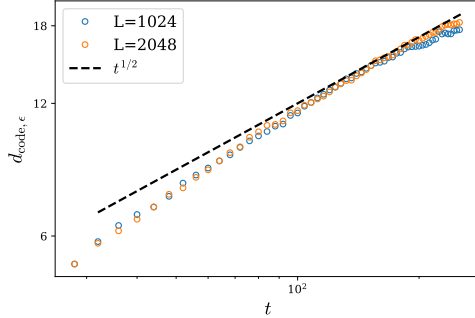


Figure 3.4: Contiguous code distance, as defined in Eq. (3.39), plotted in the log-log scale. ϵ is taken to be 1.

3.2.5 Code equilibrium v.s. entanglement equilibrium

Superlinear growth of stabilizer generators leads to a new sublinear time scale $t \simeq L^{\frac{2}{3}}$ which can be identified as an encoding time of a dynamically generated stabilizer code. Indeed, we have seen that the stabilizer length distribution, as well as the contiguous code distance, reaches a steady form after $t \simeq L^{\frac{2}{3}}$. This suggests that the resulting output state $\rho(t)$ is close to a maximally mixed state inside the dynamically generated code subspace after the code equilibrium time of $t \simeq L^{\frac{2}{3}}$.

This observation, however, appears to be in tension with previous results on monitored quantum circuits. Namely, if one starts the circuit from states with low entanglement (such as product states), the evolving state will acquire a steady form of entanglement structure and reach the volume-law entanglement only at a much later time of $t \simeq L$ [20]. Some readers might wonder if this suggests that the encoding time would actually be $t \simeq L$ instead of $t \simeq L^{\frac{2}{3}}$.

The key to resolving this apparent puzzle is to observe that not all the states in the code subspace possess volume-law entanglement. To understand this point, let us consider the entanglement entropy $S_A(t)$ for different initial states at the encoding time $t \simeq L^{\frac{2}{3}}$. When the initial state of the circuit is a product state, the output state $|\psi_{\text{prod}(t)}\rangle$ does not possess a volume-law entanglement. Namely, we have $S_A(t) \simeq |A|$ only up to $|A| \lesssim L^{\frac{2}{3}}$, and $S_A(t) \simeq L^{\frac{2}{3}}$ for $|A| \gtrsim L^{\frac{2}{3}}$. These output states $|\psi_{\text{prod}(t)}\rangle$, however, are still in the code subspace. Next, when the initial state of the circuit is a Haar random state, the output state $|\psi_{\text{Haar}(t)}\rangle$ has a volume-law entanglement. Namely, one can show that S_A for $|\psi_{\text{Haar}(t)}\rangle$ behaves in a similar way to the one for the case with a maximally mixed initial state as long as $|A| \leq \frac{L}{2}$ [52]. Here, $|\psi_{\text{Haar}(t)}\rangle$ corresponds to a typical random state inside the code

subspace.

The aforementioned observation suggests that, while there exist atypical codeword states $|\psi_{\text{prod}(t)}\rangle$ with $\simeq L^{\frac{2}{3}}$ entanglement, typical codeword states indeed possess the volume-law entanglement. This resolves the puzzle concerning $t \simeq L^{\frac{2}{3}}$ v.s. $t \simeq L$; the former is the required time to reach the codeword state while the latter is the time to attain entanglement properties of typical codeword states.

3.2.6 Pure v.s. mixed initial state

So far in this section, we have focused on cases where the initial state of the circuit is the maximally mixed state. A naturally arising question concerns what will happen if we start from a pure product state instead. It has been previously noted that the two choices lead to strikingly different behaviors of the entanglement dynamics at late time [25, 29]. Here we revisit this problem, focusing on whether the super-linear growth is also present in the pure initial state case.

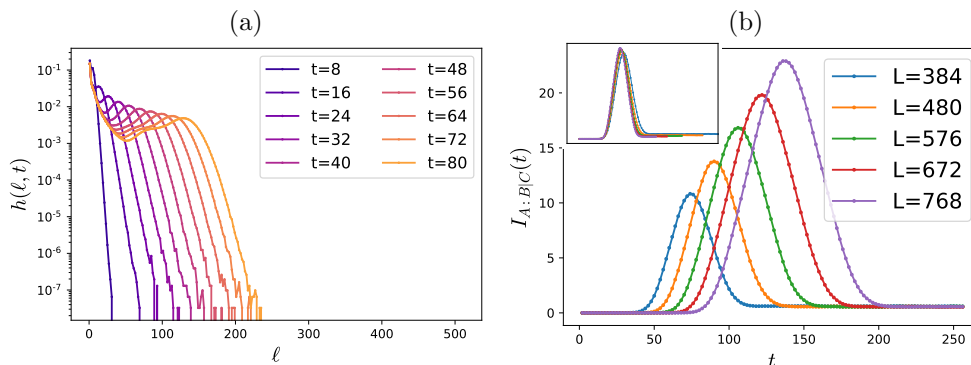


Figure 3.5: Numerical results for a pure initial state. (a) Stabilizer length distribution $h(\ell, t)$ with $L = 512$ and open boundary condition, within the same time period as in Fig. 3.2 (b) Dynamics of $I_{A:B|C}(t)$, with A , B and C arranged in the same manner as in Fig. 3.3(a). The inset shows the same data but with both axes rescaled by a factor of L^{-1} .

We present the simulated $h(\ell, t)$ for a pure product initial state in the Fig. 3.5(a). Recall that, for a pure product state, all stabilizer generators are of size one, and thus, the initial distribution is a sharp peak $h(\ell, t = 0) \propto \delta(\ell - 1)$. For $t > 0$, the short stabilizer generators will grow due to the action of unitary gates, which corresponds to a right-moving peak. On the left side of the peak, one finds a power-law decaying profile that remains unchanged

even after the peak passes. Here, the exponent $\frac{5}{3}$ is the same as the one observed in the mixed state case. This suggests that the power-law profile in $h(\ell, t)$ is present regardless of the choice of initial states. On the right side of the peak, $h(\ell, t)$ exponentially decays to zero, with an exponent that does not seem to be strongly dependent on time.

Importantly, numerical results suggest that the pure evolving state does not possess any super-linear growth. Indeed, the peak only moves linearly with t , and $h(\ell, t)$ decays quickly after the peak. This is also reflected in the simulation of $I_{A:B|C}(t)$ [Fig. 3.5(b)]. We find that the time scale for $I_{A:B|C}$ to take non-zero value scales linearly with $|C|$, in contrast to the $t \sim |C|^{\frac{3}{2}}$ in the mixed state case.

To gain some understanding of entanglement dynamics for this case, we propose the following scaling form of $h(\ell, t)$ which captures the salient features described above:

$$h(\ell, t) = c'_1 \frac{\Theta(\ell^*(t) - \ell)}{\ell^{5/3}} + c'_2 \delta(\ell - \ell^*(t)), \quad (3.40)$$

where $\ell^*(t) \approx t$ is the position of the peak. Though the peak in the figure does get broader with time, we approximate it with a delta function for ease of discussion.

By making use of Eq. (3.11) and the initial condition $S_A(0) = 0$, we derive that a contiguous region's entanglement entropy has the following form:

$$S_A(t) = \begin{cases} b_1 t + b_2 t^{\frac{1}{3}} & \ell^*(t) < |A| \\ b_1 |A| + b_2 |A|^{\frac{1}{3}} & \ell^*(t) > |A| \end{cases} \quad (3.41)$$

where the b_1 and b_2 are the same as those appeared in Eq. (3.19). This entanglement growth is similar to the one in the pure unitary dynamics starting from a pure state, where S_A typically grows linearly until saturation.

We can also use the expression above to compute $I_{A:B|C}(t)$. By keeping the leading term with b_1 only, we have

$$\begin{aligned} & I_{A:B|C}(t) \\ &= (S_{AC} + S_{BC} - S_{ABC} - S_C)(t) \\ &= \begin{cases} 0 & \frac{\ell^*(t)}{|C|} < 1 \\ b_1(t - |C|) & 1 < \frac{\ell^*(t)}{|C|} < 1 + r \\ b_1((1 + 2r)|C| - t) & 1 + r < \frac{\ell^*(t)}{|C|} < 1 + 2r \\ 0 & \frac{\ell^*(t)}{|C|} > 1 + 2r \end{cases} \quad (3.42) \end{aligned}$$

which indeed captures salient features of the simulated $I_{A:B|C}(t)$ in Fig. 3.5(b).

3.3 Information dynamics

In the previous section, we studied how the entanglement structure of the output state $\rho_{\text{out}}(t)$ evolves. In this section, we consider how local information about the input state spreads out by studying correlations between the input and the output states.

3.3.1 Input-Output correlation

In order to study information spreading, it is convenient to introduce a reference system $R = \{1_R, 2_R, \dots, L_R\}$ for the original physical system $P = \{1_P, 2_P, \dots, L_P\}$. Each qubit in R is initially maximally entangled with its partner in P , and the monitored circuit acts on the physical system only, see Fig. 3.6 for an illustration. The resulting state is

$$|\phi_{\mathbf{m}}(t)\rangle \propto \sum_{\mathbf{s} \in \{0,1\}^L} (C_{\mathbf{m}}(t) |\mathbf{s}\rangle)_P \otimes |\mathbf{s}\rangle_R \quad (3.43)$$

where $C_{\mathbf{m}}$ is defined in a way similar to and \mathbf{m} represents the measurement outcome. The output state $\rho_{\text{out}}(t)$ of a monitored circuit, when starting from a maximally mixed state, can be obtained by tracing out the reference system R as $\rho_{\text{out}}(t) = \text{Tr}_R(|\phi_{\mathbf{m}}(t)\rangle \langle \phi_{\mathbf{m}}(t)|)$.

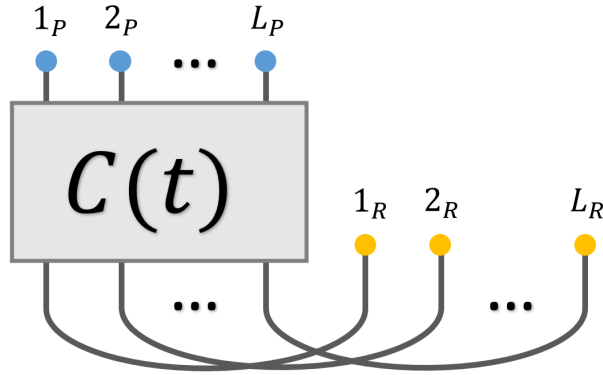


Figure 3.6: A visualization of $|\phi_{\mathbf{m}}(t)\rangle$ defined in Eq. (3.43). Physical qubits (P , blue dots) and reference qubits (R , yellow dots) are initially maximally entangled and the circuit acts on the physical qubits only.

Under the action of monitored circuits, some of the information initially contained in a subregion A_P will gradually spread without being eliminated by measurements. To

quantify this effect, we utilize the mutual information between the output and the input spaces:

$$I_{A_R:B_P}(t) = (S_{A_R} + S_{B_P} - S_{A_R \cup B_P})(|\phi_{\mathbf{m}}(t)\rangle) \quad (3.44)$$

for various subregions $B_P \subseteq P$. Intuitively, this quantity measures how much information is transmitted from A to B by the monitored circuit $C_{\mathbf{m}}(t)$.

In the remainder of this section, we will provide a physical interpretation of $I_{A_R:B_P}(t)$ and its relation to the notion of operator spreading. We then study the behavior of $I_{A_R:B_P}(t)$ in both monitored and unitary $(1+1)$ -dimensional circuits.

3.3.2 Isomorphism between quantum codes

A single trajectory of Clifford monitored quantum dynamics $C_{\mathbf{m}}$ can be viewed as an isomorphism between two quantum error-correcting codes. To see this, we perform the singular value decomposition to $C_{\mathbf{m}}$:

$$C_{\mathbf{m}} = \sum_{i=1}^K |v_i\rangle \langle u_i|. \quad (3.45)$$

Note that all the non-zero singular values of $C_{\mathbf{m}}$ are 1 as $C_{\mathbf{m}}$ is a Clifford monitored dynamics. The decomposition defines two stabilizer code subspaces: $\mathcal{H}_{\text{in}} = \langle u_1, \dots, u_K \rangle$ and $\mathcal{H}_{\text{out}} = \langle v_1, \dots, v_K \rangle$, and corresponding projectors are given by

$$P_{\text{in}} = C_{\mathbf{m}}^\dagger C_{\mathbf{m}}, \quad P_{\text{out}} = C_{\mathbf{m}} C_{\mathbf{m}}^\dagger. \quad (3.46)$$

Furthermore, the input and output stabilizer code states $\rho_{\text{in}}, \rho_{\text{out}}$ are given by maximally mixed states of $|u_i\rangle$ and $|v_i\rangle$ respectively.

Using this decomposition, we can view the dynamics $C_{\mathbf{m}}$ as a two-step process: for an incoming state $|\psi\rangle$, $C_{\mathbf{m}}$ will first discard the part of $|\psi\rangle$ that is orthogonal to \mathcal{H}_{in} :

$$|\psi\rangle \Rightarrow P_{\text{in}} |\psi\rangle, \quad (3.47)$$

then unitarily transform the remaining wavefunction into the subspace \mathcal{H}_{in} :

$$P_{\text{in}} |\psi\rangle \Rightarrow C_{\mathbf{m}} P_{\text{in}} |\psi\rangle. \quad (3.48)$$

Hence, \mathcal{H}_{in} is the input subspace whose information is preserved, while \mathcal{H}_{out} is the subspace into which the preserved information is unitarily processed.

By viewing the monitored dynamics $C_{\mathbf{m}}$ as an isomorphism between two stabilizer codes, a correspondence between logical operations for \mathcal{H}_{in} and for \mathcal{H}_{out} can be naturally defined. Assume that O and \tilde{O} are non-trivial logical operators defined on \mathcal{H}_{in} and \mathcal{H}_{out} respectively. We say that O is *transferred* to \tilde{O} by the dynamics $C_{\mathbf{m}}$ if and only if:

$$C_{\mathbf{m}}O = \tilde{O}C_{\mathbf{m}}, \quad (3.49)$$

namely, applying O on the input state is equivalent to applying \tilde{O} on the output state. It is worth noting that this is not a one-to-one correspondence as logical operators have multiple equivalent expressions which act in the same manner in code subspaces.

The notion of transferred operators, defined above, is a natural generalization of operator spreading to non-unitary settings. Note that, in the special case that C is a unitary evolution, both \mathcal{H}_{in} and \mathcal{H}_{out} are the total Hilbert spaces and any operator O is a logical operator. In particular, its transferred operator \tilde{O} is uniquely given by its unitary evolution under C as $\tilde{O} = C^\dagger O C$.

The above discussions enable us to discuss information spreading in a quantitative manner by studying the growth of logical operators under an isomorphism $C_{\mathbf{m}}$. Letting $A \subseteq P$ (input) and $B \subseteq P$ (output) be two subsets of qubits, one can ask how many inequivalent input logical operators defined on A , can be transferred to output logical operators defined on B . Namely, we are interested in the number of inequivalent O_A such that:

$$\exists \tilde{O}_B \text{ supported on } B \quad \tilde{O}_B C_{\mathbf{m}} = C_{\mathbf{m}} O_A. \quad (3.50)$$

The following theorem relates this number to the mutual information $I_{A_R:B_P}$ defined in Eq. (3.44):

Theorem 1. $I_{A_R:B_P}$ equals the number of independent and inequivalent Pauli logical operators supported on A that can be transferred by $C_{\mathbf{m}}$ to some logical operator within B .

This theorem can be easily proven using Eq. (3.11), once we notice that the expression Eq. (3.50) is equivalent to $O_A^T \otimes \tilde{O}_B |\phi_{\mathbf{m}}\rangle = |\phi_{\mathbf{m}}\rangle$, namely $O_A^T \otimes \tilde{O}_B$ is a stabilizer of $|\phi_{\mathbf{m}}\rangle$.

3.3.3 Logical operator growth

The study of operator growth plays a central role in our understanding of unitary circuits. Given the formalism developed in the previous subsection, it is natural to ask how a logical

operator's size changes in time when it is transferred in a monitored circuit. In this part, we provide an argument showing that an $O(1)$ sized logical operator will be transferred to an $O(t^{3/2})$ -sized one by t layers of circuit dynamics.

A key part of the argument is to compare output code states ρ_{out} for circuits of different depths. To do so, we deepen the circuit by adding new operations to the initial time slice C , one at a time.

First, if we add a unitary gate, then:

$$C' = CU, \quad (3.51)$$

which induces no change to the output code state:

$$\rho'_{\text{out}} \propto C' C'^{\dagger} \propto C C^{\dagger} = \rho_{\text{out}}. \quad (3.52)$$

Next, we consider the other case that a Z_i basis measurement is added to C :

$$C' = C \frac{1 + Z_i}{2}. \quad (3.53)$$

The impact on ρ_{out} depends on whether Z_i is a non-trivial logical operator of $\rho_{\text{in}} \propto C^{\dagger} C$. Namely, if Z_i is not a logical operator of ρ_{in} , or if Z_i is just a trivial logical operator of ρ_{in} , then one can show that it leaves the ρ_{out} unchanged; while if Z_i is a non-trivial logical operator of ρ_{in} , it changes ρ_{out} in the following way:

$$\rho'_{\text{out}} = \frac{1 + \tilde{Z}_i}{2} \rho_{\text{out}}, \quad (3.54)$$

where \tilde{Z}_i is a non-trivial logical operator of ρ_{out} , which is Z_i 's transferred operator as defined in Eq. (3.49):

$$C Z_i = \tilde{Z}_i C. \quad (3.55)$$

From the perspective of ρ_{out} 's stabilizers \mathcal{S}_{out} , the change Eq. (3.54) corresponds to adding a new stabilizer to \mathcal{S}_{out} :

$$\mathcal{S}'_{\text{out}} = \mathcal{S}_{\text{out}} \cup \{\tilde{Z}_i\}. \quad (3.56)$$

We can now infer the size of \tilde{Z}_i by relating our observations above to our earlier conclusion that \mathcal{S}_{out} 's stabilizer length distribution $h(\ell, t)$ follows Eq. (3.14). Since the only part of $h(\ell, t)$ that changes at time t is the small region around $\ell = \ell^*(t) \sim t^{3/2}$, we expect that \mathcal{S}_{out} 's newly added stabilizer \tilde{Z}_i is of a size $\sim t^{3/2}$. Thus Z_i is transferred to a $\sim t^{3/2}$ sized operator \tilde{Z}_i by $C(t)$. We will confirm this conjecture numerically in Sec. 3.3.5.

Here, we would like to note one caveat in the aforementioned argument concerning the size of \tilde{Z}_j . Recall that the size distribution in Eq. (3.14) is defined for stabilizer generators in a clipped gauge. Adding \tilde{Z}_j to stabilizer generators in a clipped gauge does not necessarily create stabilizers in a clipped gauge. As such, the evolution of Eq. (3.14) may be sourced by the addition of \tilde{Z}_j as well as some rearrangement of stabilizer generators to fit in a clipped gauge. Despite this subtlety, we expect that such rearrangement will not significantly alter our argument. For one thing, in the time regime of our interest, $\mathcal{S}_{\text{in}}(t)$ is not full rank, so there is an $O(1)$ chance that we do not need any rearrangement to a clipped gauge at all. Furthermore, even when \tilde{Z}_j breaks a clipped gauge, recombinations with other stabilizer generators do not change the size of \tilde{Z}_j much. Hence, we expect that our estimate remains qualitatively valid.

3.3.4 Loss of local information

In this subsection and the next, we study information spreading through numerical simulations of $I_{A_R:B_P}(t)$. We perform simulation of $I_{A_R:B_P}(t)$ for both unitary ($p = 0$) and monitored ($p = 0.08$) cases. We set $A = [-a, a]$ and $B = [-d, d]$, with the origin taken to be the midpoint of the corresponding system (P or R). An illustration of the setting is shown in Fig. 3.7. For the brevity of the presentation, we use the symbol \mathcal{I}_A as a short-hand notation for the input information within A . As we have discussed, $I_{A_R:B_P}(t)$ measures the amount of \mathcal{I}_A detectable within region $B \subseteq P$ at time t .

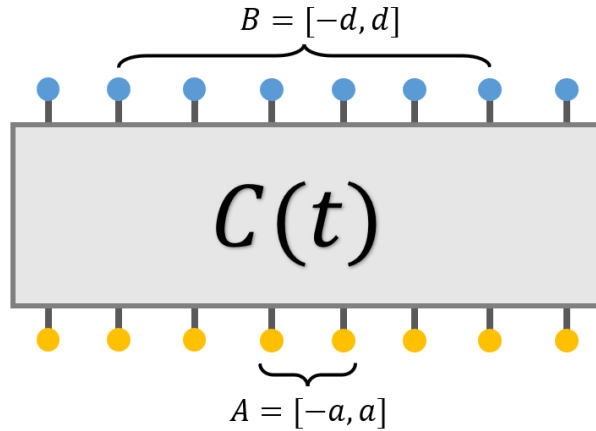


Figure 3.7: Arrangement of $A_R = [-a, a]_R$ and $B_P = [-d, d]_R$ in the numerical simulation. The figure shows the special case of $a = 1$ and $d = 3$.

We start by considering $I_{A_R:P}(t) = I_{A_R:(-\infty,\infty)_P}(t)$, *i.e.* the amount of remaining \mathcal{I}_A in the whole system at time t . In the unitary ($p = 0$) case, we know:

$$I_{A_R:P}(t) \equiv 2|A|, \quad (3.57)$$

because unitary dynamics acts on P only and R is always maximally entangled with P . This implies that \mathcal{I}_A is always preserved somewhere within the total system P , as is expected to be the case for a unitary dynamics.

When measurements are turned on ($p \neq 0$), they may destroy \mathcal{I}_A , as reflected in a gradual decay of $I_{A_R:P}(t)$, see Fig. 3.8(a). It is natural to expect that $I_{A_R:P}(t)$ will eventually become zero and \mathcal{I}_A will be completely lost, at some time scale that depends on $|A| = 2a$.

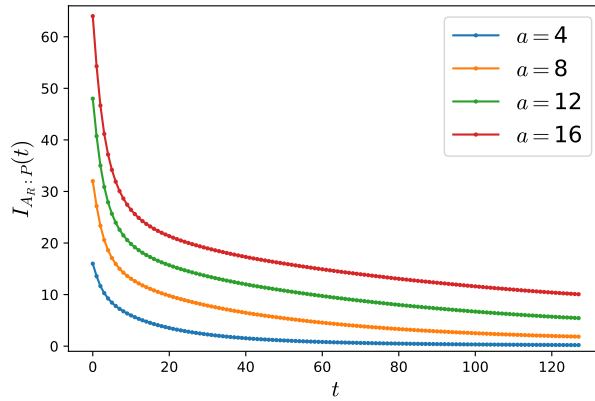


Figure 3.8: Decay of the remaining \mathcal{I}_A within the system for various different A 's sizes.

It turns out this problem, concerning the loss of local information, is equivalent to the code distance growth which we have studied in Sec. 3.2.4. Monitored circuits respect time reversal symmetry on average: $C^\dagger(t)$, which is the reversed circuit of $C(t)$, has the same distribution as $C(t)$. This implies that

$$I_{A_R:P}(t) = I_{A_P:R}(t). \quad (3.58)$$

Note that this equality is defined for averaged quantities, and may not hold for each instance. In Sec. 3.2.4, we derived that the *r.h.s.* vanishes when $|A| < O(\sqrt{t})$. This suggests that the time scale for \mathcal{I}_A to be completely lost is given by

$$t_{\text{loss}}^* \sim |A|^2. \quad (3.59)$$

3.3.5 Information spreading

Next, we study how the remaining \mathcal{I}_A spreads with time. Since we are interested in the portion of \mathcal{I}_A which was not lost by measurements, we analyze the following normalized mutual information:

$$\mu(d, t) = \frac{I_{A_R:[-d,d]_P}(t)}{I_{A_R:P}(t)}. \quad (3.60)$$

Here, $\mu(d, t)$ measures the *fraction* of survived \mathcal{I}_A detectable within the region $[-d, d]$, at a given time t . Note that the spreading of \mathcal{I}_A is only well defined before it is completely lost, *i.e.* before the time scale Eq. (3.59).

Fig. 3.9 (a) and (b) show the heatmaps of normalized mutual information as a function of radius d and time t , for unitary and monitored dynamics respectively. We find that there are three regimes: a dark blue region where $\mu(d, t) \approx 0$ for small d , a bright yellow region where $\mu(d, t) \approx 1$, and an intermediary transitioning region.

- $\mu(t, d) \approx 1$ implies that $[-d, d]$ contains all the remaining \mathcal{I}_A at time t , and thus the smallest such d marks the boundary of the region where the remaining \mathcal{I}_A is supported on. Formally we can define this boundary as

$$D_\epsilon(t) = \operatorname{argmin}_d (\mu(d, t) \geq 1 - \epsilon) \quad (3.61)$$

for some $\epsilon \ll 1$, and $[-D_\epsilon(t), D_\epsilon(t)]$ is where the remaining \mathcal{I}_A is supported. We plotted $D_{0.1}(t)$ with orange dashed lines in Fig. 3.9(a) and (b).

- $\mu(t, d) \approx 0$ implies that one cannot probe any \mathcal{I}_A within $[-d, d]$. We observe that, in both unitary and monitored cases, there exists a region with $\mu(t, d) \approx 0$. $[-d_\epsilon(t), d_\epsilon(t)]$ defines the largest region that no information \mathcal{I}_A can be detected. The radius of the information-less region can be quantified by ($\epsilon \ll 1$):

$$d_\epsilon(t) = \operatorname{argmax}_d (\mu(d, t) \leq \epsilon). \quad (3.62)$$

In Fig. 3.9(b), $d_{0.1}(t)$ are plotted using blue dashed lines.

The physical meaning of $D_\epsilon(t)$ and $d_\epsilon(t)$ becomes clear by recalling the discussion in Sec. 3.3.2. Let us assume that O_A is transferred to \tilde{O}_B by the dynamics C_m , in the sense of Eq. (3.50). Recalling that $I_{A_R:B_P}$ measures the amount of logical operators transferred from A to B , we conclude \tilde{O}_B can be supported within $[-D_\epsilon(t), D_\epsilon(t)]$ but beyond $[-d_\epsilon(t), d_\epsilon(t)]$.

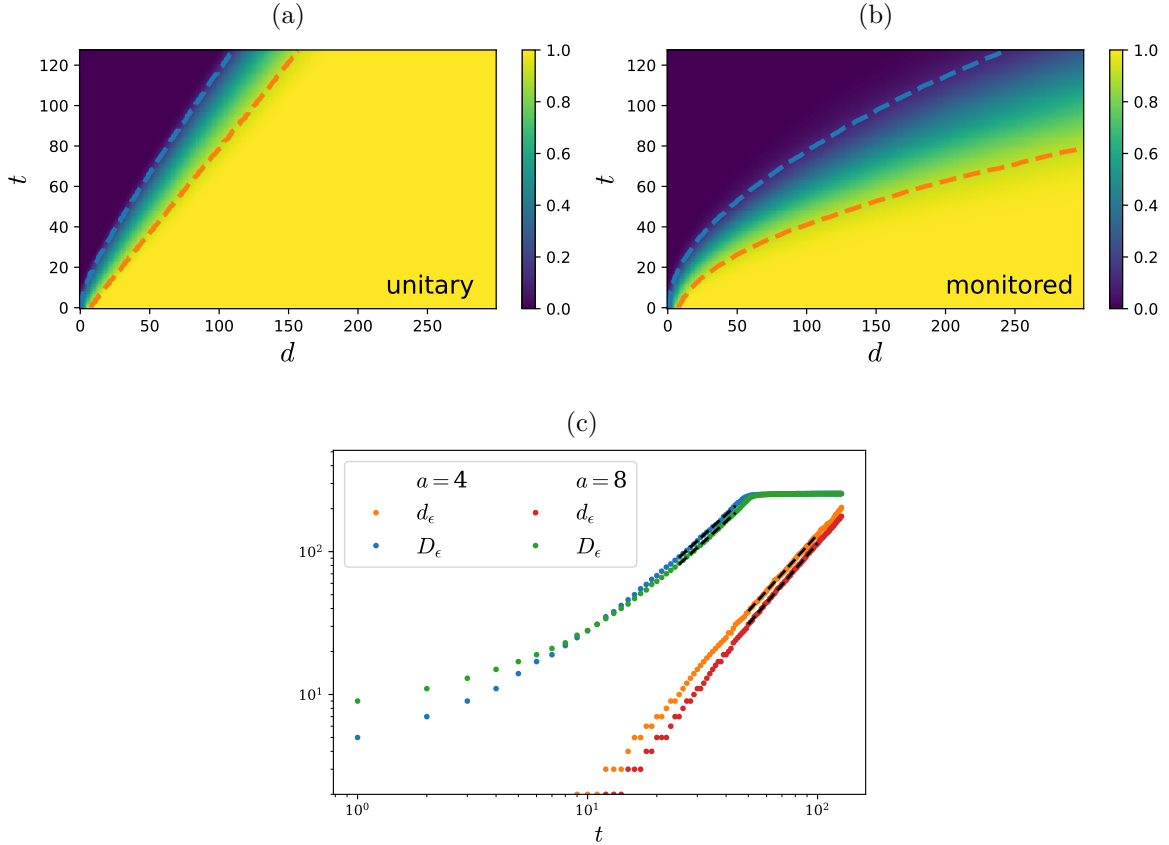


Figure 3.9: Simulation results for $I_{A_R:B_P}(t)$ in a system with $L = 768$ qubits. (a)(b) Heatmaps of the normalized mutual information μ_{A_R,B_P} , as a function of t and $|B|=2d$, for unitary and monitored dynamics respectively. (c) The growth of $d_\epsilon(t)$ and $D_\epsilon(t)$ with $\epsilon = 0.01$. Both quantities develop power-law growing behaviors at late time. The D_ϵ curve has a plateau at late time as they reach the boundary of the simulated system.

This is consistent with and further generalizes our conclusion in Sec. 3.3.3, stating that a $O(1)$ sized operator will be transferred to a $O(t^{3/2})$ sized one after t steps of dynamics.

The evolutions of the three regions define information lightcones, whose behaviors sharply differ between unitary and monitored dynamics. Here, $d_\epsilon(t)$ and $D_\epsilon(t)$ correspond to the inner and the outer front of the lightcone respectively. In the unitary case in Fig. 3.9(a), both lightcones grow linearly with time, consistent with emergent causality. In contrast, in the monitored case in Fig. 3.9(b), both lightcones are outward bent, corresponding to the super-linear spreading of \mathcal{I}_A . In Fig. 3.9(c), we plot the growth of $d_\epsilon(t)$ and $D_\epsilon(t)$ with $\epsilon = 0.01$. Both $d_\epsilon(t)$ and $D_\epsilon(t)$ display power-law growth in late time, with the fitted exponents (fitted lines are displayed as black dashed lines in the figure):

$$\begin{aligned} a = 4 : \quad d_\epsilon(t) &\propto t^{1.78}, & D_\epsilon(t) &\propto t^{1.47}, \\ a = 8 : \quad d_\epsilon(t) &\propto t^{1.89}, & D_\epsilon(t) &\propto t^{1.46}. \end{aligned} \tag{3.63}$$

We notice that the inner and the outer front have different exponents. Namely, the latter one is close to $3/2$ as predicted in Sec. 3.3.3.

Furthermore, the inner exponent is larger than the outer one, suggesting that two fronts are likely to collide at some point. This is consistent with the interpretation that the inner front and the outer front respectively mark the shortest and the longest survived logical operator initially supported on A . Recall that all the logical operators will be eventually destroyed (*i.e.* $I_{AR:P} \approx 0$) at a time scale $t \propto |A|^2$, and shortly before this time scale, there will be only one logical operator surviving. This logical operator is both the longest logical operator and the shortest logical operator, which means that two fronts of the lightcone collide. Numerically accessing this time scale, however, is challenging due to the requirement of running a large system for a long time.

We currently do not have a physical explanation of the exponent for $d_\epsilon(t)$. We leave this as a future question.

3.3.6 Partially fixing the input state

Until now, we have treated $C_{\mathbf{m}}$ as a dynamical process whose input is the entire physical system P . In this subsection we discuss the consequence of using only a small subregion $A \subseteq P$ as the input while fixing the initial state for other qubits in $A^c = P \setminus A$. In the error-correcting code perspective, fixing part of the initial state effectively selects a subspace of the original code space. Here, we restrict our discussion to the case that ρ_{A^c} is a homogeneous product state: $\rho_{A^c} = \otimes_{i \in A^c} (\rho_0)_i$, where ρ_0 is some single qubit density

matrix, see Fig. 3.5(a) for illustration. A similar setting was considered in [58] for studying information spreading in measurement-only circuits.

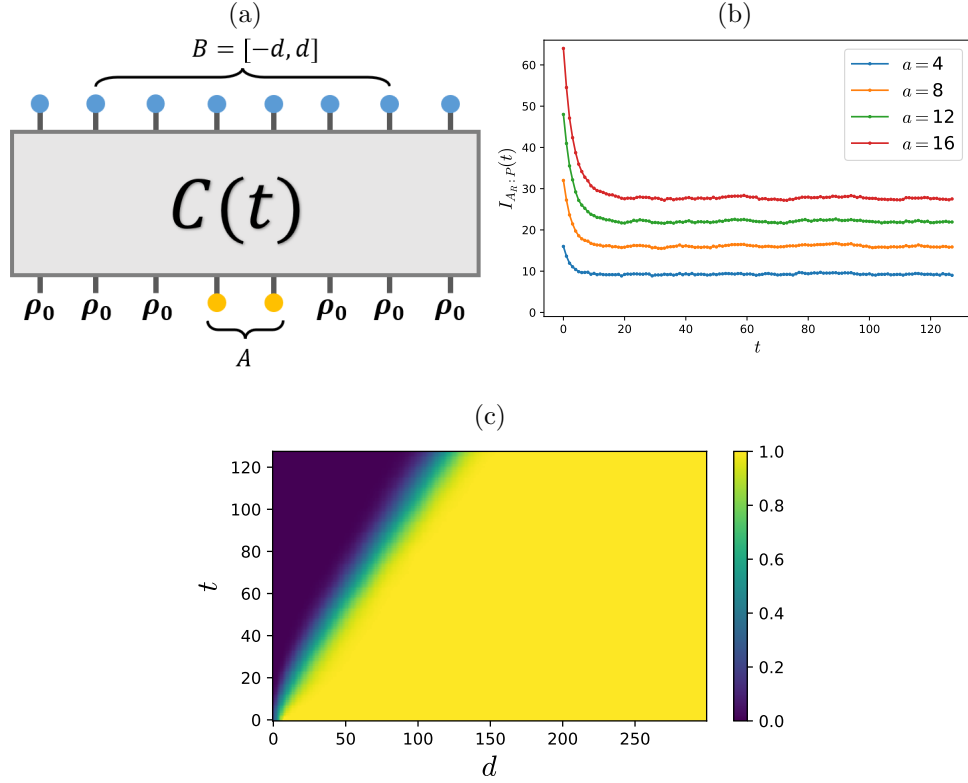


Figure 3.10: (a) The circuit configuration for the alternative setting to characterize information spreading discussed in Sec. 3.3.6, where $A = \{3, 4\}$ (b) Decay of $A = [-a, a]$'s initial information with time t . (c) Heatmap of the normalized mutual information $\mu(d, t)$ in the alternative setting

Let us begin by introducing a reference system R which is maximally entangled with A initially. Note that, in this case, $R = A_R = [-a, a]_R$ has the same size as A .

We first discuss the case that $\rho_0 = \frac{1}{2}\mathbb{I}$, *i.e.* the input state on A_P^c is initially maximally mixed. This enforces no constraint on the codespace, so it is equivalent to the previously studied case in Sec. 3.3.5.

Next, we consider the case $\rho_0 = |0\rangle\langle 0|$, *i.e.* qubits in A_P^c are initially prepared in a pure product state. We present the numerically simulated $I_{A_R: B_P}(t)$ in Fig. 3.10(b-c).

In panel (b), we observe that A 's input information equilibrates to some constant value instead of decaying to zero with time (at exponentially long time, we expect it to decay to zero). In addition, in panel (c) which displays the heatmap for the normalized mutual information $\mu(d, t)$, we find that the remaining information spreads only linearly, instead of super-linearly with time. This behavior of information spreading is similar to the one observed in measurement-only dynamics within its volume-law, as reported in [58].

3.4 domain-wall Picture

It has been proposed that several universal features of entanglement dynamics in weakly monitored circuits can be described effectively by modeling entanglement domain-walls using directed polymers in a random environment (DPRE) [26]. In this section, we revisit our results from the domain-wall picture and the DPRE effective theory.

3.4.1 Review of domain-wall picture

We begin by providing a brief review of the domain-wall picture and the DPRE effective theory. We refer interested readers to [59, 31, 30, 60, 61] for detailed discussions on how to map monitored circuits to statistical mechanics models as well as how the former's entanglement properties are related to domain-walls in the latter.

Consider a t -layer circuit defined on an infinite qubit chain with the initial state being maximally entangled with the reference R as in Fig. 3.6. By stacking Q copies of the $(1+1)$ -dimensional circuit and performing disorder average over random unitary gates, one can map the whole system to a $(2+0)$ -dimensional classical statistical mechanics model on the same space-time manifold. Through this mapping, each unitary gate is mapped to a spin in the bulk, while each qubit in P and R is mapped to a spin located at the boundaries. Here, spins $\{s\}$ take values in the permutation group S_Q . The weakly-monitored phase of the circuit corresponds to the ordered phase of the spin model.

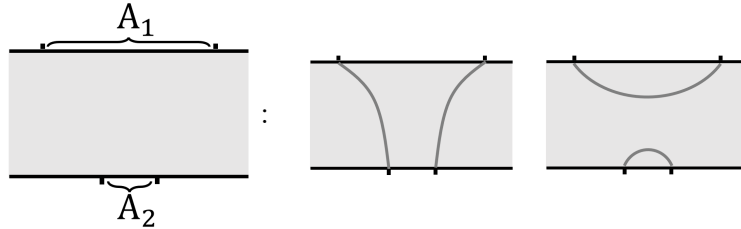
Entanglement properties of the original quantum circuit can be found by looking for the domain-walls in the statistical mechanics model. In particular, the entanglement entropy $S_A(t)$ of a boundary region $A \in P \cup R$ is given by the free energy cost of a domain-wall

that separates A from the rest of the boundary $\bar{A} = P \cup R - A$:

$$S_A(t) \approx f \left(\begin{array}{c} \overline{A} \quad A \quad \overline{A} \\ \text{P} \overbrace{\hspace{10em}} \\ \text{R} \underbrace{\hspace{10em}} \\ \overline{A} \end{array} \right) \quad (3.64)$$

where $f(\cdot)$ denotes the energy cost of the domain-wall(s) configuration (the dark grey curve).

While the above figure considers the case where A is a single contiguous region, the region A can be any subset of $P \cup R$. Generally, there may be domain-wall configurations with different topologies that separate A and \bar{A} . For example, if $A = A_1 \cup A_2$ with $A_1 \subseteq P$ and $A_2 \subseteq R$, the domain-wall can have two different topologies:



In this case the free energy, in the leading order, is given by the configuration that gives the smaller free energy:

$$S_A(t) = \min \left\{ f \left(\begin{array}{c} \text{---} \\ \text{---} \end{array} \right), f \left(\begin{array}{c} \text{---} \\ \text{---} \end{array} \right) \right\} \quad (3.65)$$

Furthermore, if the domain-wall has several disconnected pieces (for instance in the case shown above), its total free energy is the sum of each individual piece's contribution.

Solving domain-wall's properties from the statistical mechanics model is in general not feasible. In [26], the authors find numerical and analytical evidence suggesting that large-scale properties of the domain-wall are captured by DPRE. In particular, a single piece of domain-wall's energy cost is approximately proportional to the length of the shortest path connecting two endpoints in a random media:

$$f \left(\begin{array}{c} \mathbf{x} \\ \text{---} \\ \mathbf{y} \end{array} \right) \simeq \min_{\substack{\mathbf{z}(\tau): \mathbf{z}(0)=\mathbf{x}, \\ \mathbf{z}(1)=\mathbf{y}}} \left(\int_0^1 V(\mathbf{z}(\tau)) |\mathbf{z}'(\tau)| d\tau \right) \quad (3.66)$$

$$\equiv D(\mathbf{x}, \mathbf{y}),$$

where $V(\mathbf{x})$ is a quenched random potential without spatial-temporal correlation $\text{cov}(V(\mathbf{x}), V(\mathbf{y})) = \sigma^2 \delta_{\mathbf{x}, \mathbf{y}}$ and with a positive mean $\mathbb{E}[V(\mathbf{x})] = \mu > 0$. The $\mathbf{z}(\cdot)$ runs over all paths connecting \mathbf{x} to \mathbf{y} . It should be noted that, while the leading term in $D(\mathbf{x}_1, \mathbf{x}_2)$ is proportional to $|\mathbf{x}_1 - \mathbf{x}_2|$, it contains a subleading contribution which gives rise to non-trivial multipartite entanglement as we shall see later.

Before finishing the review, we discuss an issue about the directedness of the shortest paths $\mathbf{z}(\tau)$ appearing in Eq. (3.66). In the original proposal of the effective theory [26], it is further required that $\mathbf{z}(\cdot)$ is only chosen from paths that are *directed* (*i.e.* not going backward) along the \mathbf{x} - \mathbf{y} direction, as is suggested by the word ‘directed’ in the name DPRE. In fact, this extra constraint does not have to be added by hand. This is because for a typical realization of V , the not-necessarily-directed shortest path connecting \mathbf{x} and \mathbf{y} has only a $O(1)$ length overhang along the \mathbf{x} - \mathbf{y} direction [62], which is negligible after coarse-graining. In other words, directed shortest paths and un-directed shortest paths connecting \mathbf{x} and \mathbf{y} belong to the same universality class, and are indistinguishable in the thermodynamic limit. Thus, depending on our purpose, we can impose or lift the directedness at our convenience at the lattice level without worrying about getting different conclusions in the thermodynamic limit.

3.4.2 Domain-wall interpretation of S_A

Henceforth, for each quantity O defined in the context of monitored circuits, we use $[O]$ to denote its counterpart in the DPRE effective theory.

We start from the simplest case: entanglement entropy of a single contiguous interval A . Using the domain-wall description Eq. (3.64), S_A can be written as follows:

$$\begin{array}{c} \text{A} \\ \text{---} \\ \mathbf{x}_1 \quad \mathbf{x}_2 \\ \text{---} \\ \text{---} \end{array} : S_A(t) = f \left(\begin{array}{c} \text{---} \\ \text{---} \\ \text{---} \end{array} \right), \quad (3.67)$$

where

$$\mathbf{x}_1 = (0, t), \quad \mathbf{x}_2 = (|A|, t) \quad (3.68)$$

and

$$[S_A(t)] \simeq D(\mathbf{x}_1, \mathbf{x}_2). \quad (3.69)$$

Numerical and theoretical studies in [26] found that the mean of D takes the following scaling form:

$$\overline{D(\mathbf{x}_1, \mathbf{x}_2)} = s_0(t)|A| + |A|^{\frac{1}{3}}\Phi(t|A|^{-\frac{2}{3}}), \quad (3.70)$$

where $\Phi(\cdot)$ in the subleading term is a universal scaling function with the following limiting behavior:

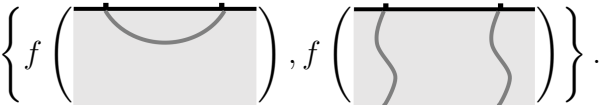
$$\Phi(\eta) = \begin{cases} \eta^{1/2} & \eta \rightarrow 0 \\ \eta^0 & \eta \rightarrow \infty \end{cases} \quad (3.71)$$

This implies that the subleading part of $S_A(t)$ behaves as:

$$S_A^{\text{sub}}(t) \simeq \begin{cases} t^{\frac{1}{2}} & t \ll |A|^{\frac{2}{3}} \\ |A|^{\frac{1}{3}} & t \gg |A|^{\frac{2}{3}} \end{cases} \quad (3.72)$$

This agrees with our results derived from the stabilizer length distribution in Sec. 3.2.2. Furthermore, since the conditional mutual information Eq. (3.32) and the growth of contiguous code distance Eq. (3.5) rely only on the dynamics of $S_A(t)$ in single intervals, we conclude these are also consistent with the DPRE effective theory.

The domain-wall picture also provides a useful insight into the S_A 's different behaviors for pure and for completely mixed initial states. In the pure initial state case, the underlying statistical mechanics model assumes free boundary condition on the $t = 0$ boundary [59, 27, 31], and domain-walls can freely start or end on the $t = 0$ boundary. We thus have

$$S_A(t) \approx \min \left\{ f \left(\text{Diagram 1} \right), f \left(\text{Diagram 2} \right) \right\}. \quad (3.73)$$


Using properties of the $D(\cdot)$ function, we notice that in the leading order the first term is $O(|A|)$, while the second term is $O(t)$. This suggests that, when t is sublinear in $|A|$, the second term is preferred over the first one. This changes at a time scale $t^* \simeq |A|$, after which the first term becomes smaller. Furthermore, we notice that the time scale t^* is far later than the other time scale $\simeq |A|^{2/3}$ at which the first term would reach the equilibrium. We thus conclude that $S_A(t)$ hardly changes after t^* . In summary, we have the following behavior of $S_A(t)$:

$$S_A(t) \simeq \begin{cases} t & t < t^* = O(|A|) \\ |A| & t > t^* \end{cases} \quad (3.74)$$

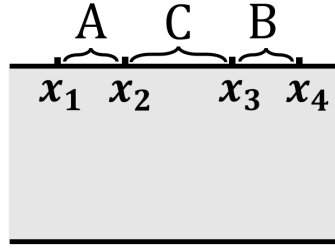
which agrees with the results we obtained in Sec. 3.2.6.

3.4.3 Domain-wall interpretation of $I_{A:B}$

Next, we turn our attention to the mutual information $I_{A:B}$ and present a derivation of Eq. (3.29) using the domain-wall picture, which is reprinted below

$$I_{A:B} \approx \max\{S_A + S_B - S_{ABC} - S_C, 0\}. \quad (3.75)$$

Here, A , B and C are arranged as follows:



Using the relation Eq. (3.64), the domain-wall representations for the three terms in $I_{A,B}$ are:

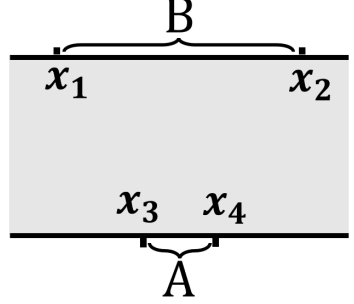
$$\begin{aligned}
 S_A &= f \left(\begin{array}{c} \text{---} \\ \text{---} \\ \text{---} \end{array} \right), \\
 S_B &= f \left(\begin{array}{c} \text{---} \\ \text{---} \\ \text{---} \end{array} \right), \\
 S_{AB} &= \min \left\{ f \left(\begin{array}{c} \text{---} \\ \text{---} \\ \text{---} \end{array} \right), f \left(\begin{array}{c} \text{---} \\ \text{---} \\ \text{---} \end{array} \right) \right\} \\
 &= \min\{S_{ABC} + S_C, S_A + S_B\}.
 \end{aligned} \quad (3.76)$$

Combining them together, we again obtain Eq. (3.29).

Here we would like to point out a certain subtlety, due to the subleading contributions, in evaluating the minimum of domain-wall's free energies. Recalling that the leading order contribution of a domain-wall's free energy is proportional to the distance between two endpoints, one might think that the second domain-wall configuration for S_{AB} in Eq. (3.76) would be always smaller. Notice, however, that the difference in the leading order contributions is $O(|C|)$, and if $|C|$ is comparable to the subleading terms in S_A or S_B , the subleading contributions could make the first domain-wall configuration smaller. This is indeed what we observed in the calculations of the code distance in Sec. 3.2.4.

3.4.4 Domain-wall interpretation of $I_{A_R:B_P}$

Finally, we evaluate $I_{A_R:B_P}$, defined in Eq. (3.44), which was used as a measure of information spreading in Sec. 3.3. Recall that the intervals A and B have the following configuration:



Using the domain-wall picture, we can obtain the following relations:

$$\begin{aligned}
 S_{A_R} &= f \left(\text{Diagram 1} \right) \\
 S_{B_P} &= f \left(\text{Diagram 2} \right) \\
 S_{A_R \cup B_P} &= \min \left\{ f \left(\text{Diagram 3} \right), f \left(\text{Diagram 4} \right) \right\} \\
 \Rightarrow I_{A_R:B_P} &\approx \max \left\{ 0, f \left(\text{Diagram 3} \right) - f \left(\text{Diagram 4} \right) \right\}.
 \end{aligned} \tag{3.77}$$

In the last line we make use of the additive property of the domain-walls' energies:

$$f \left(\text{Diagram 1} \right) + f \left(\text{Diagram 2} \right) \approx f \left(\text{Diagram 3} \right). \tag{3.78}$$

The four points involved are chosen as

$$\begin{aligned}
 \mathbf{x}_1 &= (-d/2, t), & \mathbf{x}_2 &= (d/2, t), \\
 \mathbf{x}_3 &= (-a/2, 0), & \mathbf{x}_4 &= (a/2, 0).
 \end{aligned} \tag{3.79}$$

and we have

$$[I_{A_R:B_P}(t)] = \max\{0, D(\mathbf{x}_1, \mathbf{x}_2) + D(\mathbf{x}_3, \mathbf{x}_4) - D(\mathbf{x}_1, \mathbf{x}_3) - D(\mathbf{x}_2, \mathbf{x}_4)\}. \quad (3.80)$$

Since the analytical expressions for $D(\mathbf{x}_1, \mathbf{x}_3)$ and $D(\mathbf{x}_2, \mathbf{x}_4)$ are not known, we resort to a direct simulation of Eq. (3.80). Details about the shortest paths simulation can be found in Sec. C.2.

As shown in Fig. 3.11(a), the behavior of the simulated $[\mu_{A_R:B_P}(t)] = [I_{A_R:B_P}(t)]/[I_{A_R:P}(t)]$ is qualitatively similar to that of $\mu_{A_R:B_P}$ shown in Fig. 3.9(b). Furthermore, we calculate $[d_\epsilon(t)]$ and $[D_\epsilon(t)]$ and find that they also develop power-law growth in late times (Fig. 3.11(b), black dashed lines are power-law fittings). The exponents are fitted to be:

$$d_\epsilon(t) \propto t^{1.92}, \quad D_\epsilon(t) \propto t^{1.53}. \quad (3.81)$$

The exponents numerically agree with those obtained in Eq. (3.63), reflecting the consistency between our results and the DPRE effective theory.

3.5 Discussions and outlook

In this work, we studied the quantum information dynamics in weakly monitored Clifford quantum circuits and found that entanglement and information can spread superlinearly with time ($\simeq t^{\frac{3}{2}}$). Namely, we observed that such superballistic propagation of information is mediated by superlinear growth of the size of stabilizer generators due to projective measurements. Furthermore, this led to a new sublinear time scale of $\simeq L^{\frac{2}{3}}$ which can be interpreted as the encoding time of a dynamical quantum error-correcting code. It is important to emphasize again that these nonlocal effects emerge in the non-relativistic limit where each local observer instantly learns the measurement outcomes.

While we focused on a particular setup of a $(1+1)$ -dimensional random weakly-monitored Clifford circuit with $p = 0.08$, we expect that our results reveal universal aspects of monitored quantum many-body dynamics. Indeed, some of our technical results suggest further generalization. For example, the stabilizer length distributions can be replaced with the conditional mutual information Eq. (3.13) when studying monitored circuits beyond Clifford gates.

One important future question is to reveal the microscopic origin of the superlinear entanglement growth. In this work, we have taken a few first steps toward this goal. Namely, we identified the scaling form of the time evolution of the stabilizer length distributions

$h(\ell, t)$ for both pure and mixed initial states. A key next step will be to understand the underlying microscopic mechanism for the superlinear growth of stabilizer generators and the effect of projective measurements. Also, we have presented a derivation of the mutual information for two disjoint intervals by utilizing a probabilistic argument on the operator contents of stabilizer generators. Our analysis matched with the macroscopic prediction from DPRES, including the subleading contributions. This hints that probabilistic arguments on operator contents may provide further insights into the microscopic origin of the effective theory of monitored quantum circuits.

The notion of information spreading has played a key role in investigating the bulk and boundary dynamics in the AdS/CFT correspondence. This naturally prompts us to ponder over a possible gravitational dual of monitored quantum circuits and the geometric manifestation of the superlinear entanglement growth. In the bulk quantum gravity, it has been conjectured that some class of projection operations can be modeled as insertions of End-of-World (EoW) branes [63, 64]. In the boundary quantum many-body physics, recent studies suggest that projective measurements of a few qubits can induce significant changes of the entanglement structure due to the underlying scrambling dynamics [65]. The effect of measurements on a conformal field theory has been considered in [66, 67, 68, 69], and the holographic bulk interpretation analyzed in [70, 71]. It will be interesting to further look into the geometric interpretation of continuous monitoring in quantum gravity and the resulting entanglement dynamics.

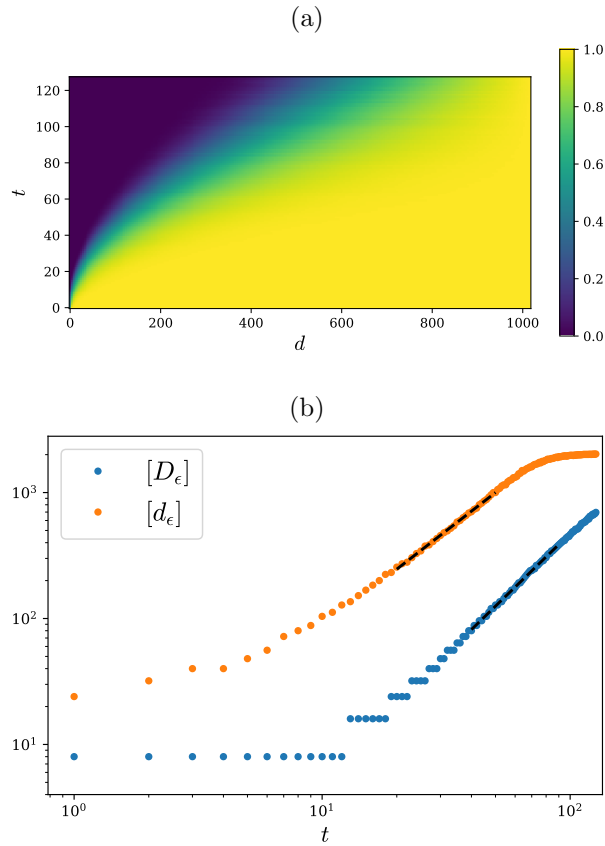


Figure 3.11: Numerical result for the shortest path simulation. (a) Heatmap of the simulated $[\mu_{A_R, B_P}(t)]$. The figure should be compared with its counterpart in the Clifford simulation Fig. 3.9(b). (b) $[d_\epsilon(t)]$ and $[D_\epsilon(t)]$ extracted from the simulation data, with $\epsilon = 0.01$. The black dashed lines are power-law fittings, with fitted exponents shown in Eq. (3.81)

Chapter 4

Real-space renormalization group for quantum mixed states

Starting from this chapter, we shift our attention to quantum mixed states' phases of matter.

Real-space renormalization group (RG) played a major role in both statistical mechanics and quantum many-body physics. The idea dates back to Wilson [72] and Kadanoff [73] who proposed that under block spin transformations, statistical mechanical systems flow to fixed points whose properties are easier to characterize. In the context of quantum many-body systems, real-space RG has led to the development of powerful numerical algorithms, including density matrix renormalization group (DMRG) [74], multiscale entanglement renormalization ansatz (MERA) [75], as well as theoretical tools, including matrix product states (MPS) [76], projected entangled pair states (PEPS) [77], etc.

In this chapter, we define a real-space RG scheme for mixed states involving local channel (LC) transformations to establish the existence of mixed-state phases. We define an “ideal” RG to consist of local channels acting on blocks which preserve correlations between different blocks, and we prove that the actions of such correlation-preserving channels can be reversed by another channel, thus establishing the phase equivalence of the fine-grained and coarse-grained states. As an example, we construct an ideal RG for the two-dimensional toric code at finite temperature and show that the temperature monotonically increases under coarse graining and thus the state does not possess topological order.

4.1 Real-space RG of quantum mixed-states

According to the definition 2, to answer whether two given states ρ_1 and ρ_2 are in the same phase we need to either construct a pair of local channel transformations or prove their nonexistence.

Recall that when studying pure-state phases of ground states, adiabatic paths between Hamiltonians provide a convenient way of obtaining phase equivalence. Let $|\psi_1\rangle$ and $|\psi_2\rangle$ be ground-states of local Hamiltonians H_1 and H_2 . If there is a path from H_1 to H_2 in the space of local Hamiltonians such that the energy gap remains $O(1)$ throughout the path, there is a standard way to construct a LU transformation connecting $|\psi_1\rangle$ to $|\psi_2\rangle$ which establishes the phase equivalence [78]. For mixed states, there is generally no counterpart to adiabatic paths.

In this section, we introduce the mixed-state real-space renormalization group (RG) as an alternative way to find LC connections and identify mixed-state phases.

4.1.1 From pure-state RG to mixed-state RG

Conceptually, RG transformation in classical and quantum statistical mechanics is an iterative coarse-graining process that discards short-range degrees of freedom while preserving long-range ones. The idea of using real-space renormalization to study zero-temperature physics of lattice quantum systems (‘numerical RG’) was pioneered by Wilson when considering impurity problems [72], and was later generalized and developed into a series of powerful RG-based numerical methods including DMRG [74], entanglement RG [75], etc. We refer to all of them as pure-state RGs, in contrast to the mixed-state RG we introduce in this work. ¹

For the sake of presentation, we restrict our attention to one-dimensional systems and only focus on tree-like RG circuits (see Fig. 4.1). All the main ideas can be easily generalized to more sophisticated RG circuit structures, *e.g.* entanglement RG circuits [75], as well as higher dimensional systems.

Pure-state RG, in its simplest form, involves partitioning the lattice into consecutive blocks each with size b and applying a coarse-graining map w_B^\dagger to each block B of a pure state $|\psi\rangle$. More specifically, coarse-graining involves truncating the Hilbert space, and w_B is an isometry satisfying $w_B^\dagger w_B = \mathbb{I}$. As proposed [74] for the density matrix renormalization

¹Another aspect of pure-state RG is that it preserves the low-energy physics of the system. But here we emphasize this less because for mixed-states, there may not be a notion of energy or Hamiltonian.

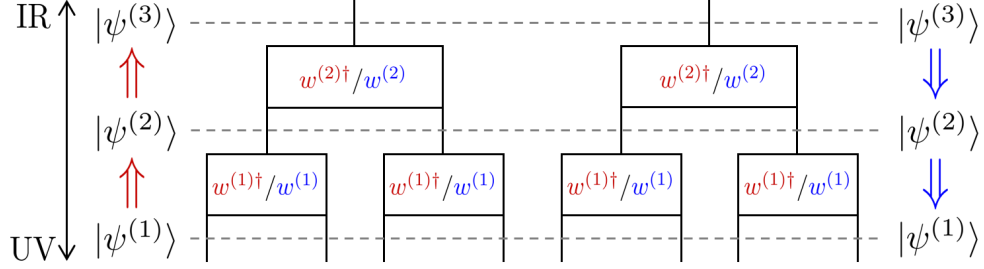


Figure 4.1: **Real-space RG transformation of pure states**– Circuit representation of two iterations of pure state RG transformation. At the ℓ -th iteration, the coarse-graining isometry $w^{(\ell)}$ is determined by the level’s input state $|\psi^{(\ell)}\rangle$ using Eq.(4.1). By applying the circuit from bottom to top (red arrows), all the short-range features of the initial UV state are gradually discarded, and only long-range ones are kept in the IR state $\rho^{(\ell \rightarrow \infty)}$. By applying the circuit from top to bottom (blue arrows), the circuit generates the UV state $|\psi^{(1)}\rangle$.

group (DMRG) algorithm, the optimal choice of w_B that preserves all correlations between B and its complement is given by

$$\text{supp } w_B w_B^\dagger = \text{supp } \rho_B \quad (4.1)$$

where $\rho_B := \text{tr}_{\bar{B}}(|\psi\rangle\langle\psi|)$ is the reduced density matrix of the block B . $\text{supp } K$ of a positive semi-definite matrix K means the subspace spanned by K ’s eigenstates with positive eigenvalues. If the original state $|\psi\rangle$ has area law entanglement $S_B \equiv -\text{tr}[\rho_B \log \rho_B] = O(1)$, then each block is efficiently coarse-grained into a constant dimensional Hilbert space independent of the original block size².

Now we turn to 1D mixed-states. In contrast to the pure state case, physical mixed states (*e.g.* ones mentioned below Def.2) typically have volume-law scaling of S_B , leading to inefficient compression using the w_B selected according to Eq.(4.1). This is because S_B results from not only correlations between B and the complementary system \bar{B} but also between B and a purifying environment E of the mixed state. The latter is the non-universal information that should be discarded. We thus need a new criterion for finding the coarse-graining map.

²Rigorously speaking, it is only proven that the ground state of a gapped local Hamiltonian satisfying the area law can be represented as an MPS with a bond dimension that grows sublinearly with the system size [79]. However, in practice, it is usually true that a finite bond dimension suffices to reproduce an accurate wavefunction for arbitrary large (even infinite) system sizes.

To motivate the criterion we introduce, we observe that Eq.(4.1) can be interpreted as the solution to the optimization problem:

$$\begin{aligned} & \operatorname{argmin}_{w_B} \dim_{\text{out}}(w_B^\dagger) \\ \text{s.t. } & I_{B:\bar{B}}(w_B^\dagger |\psi\rangle) = I_{B:\bar{B}}(|\psi\rangle), \end{aligned} \tag{4.2}$$

where $\dim_{\text{out}}(w_B^\dagger)$ is the output dimension of w_B^\dagger and $I_{X:Y} := S_X + S_Y - S_{XY}$ is the quantum mutual information, a measure of correlations between two parties X and Y . The constraint has clear physical meaning in the context of RG: by preserving $I_{B:\bar{B}}$, it preserves all the long-distance correlation within $|\psi\rangle$. We thus use ‘ $I_{B:\bar{B}}$ preserving’ condition as a guideline to generalize Eq.(4.1) to mixed-states.

4.1.2 Correlation-preserving map

We make the argument above more precise:

Definition 3 (correlation-preserving maps). For a given bipartite quantum state $\rho = \rho_{AB}$, a quantum channel $\mathcal{E}_{A \rightarrow A'}$ acting on A is *correlation-preserving* with respect to ρ_{AB} if it satisfies

$$I_{A':B}(\mathcal{E}_{A \rightarrow A'}(\rho)) = I_{A:B}(\rho)$$

It is worth noting that a channel being correlation-preserving or not depends on both the input state and the bipartition: the same map \mathcal{E} that is correlation-preserving with respect to one (ρ, B) pair may not be so with respect to another pair.

Recalling that the motivation for defining an RG scheme is to establish equivalence between two mixed states by finding a local channel transformation and its inverse, ideally we would like \mathcal{E} 's action on ρ to be reversible. Conveniently, the two desired properties (correlation-preserving and reversibility) are equivalent, as we prove in the following theorem.

Theorem 2. For a given bipartite quantum state $\rho = \rho_{AB}$, the map $\mathcal{E}_{A \rightarrow A'}$ is correlation-preserving if and only if there exists another quantum channel $\mathcal{D}_{A' \rightarrow A}$, such that:

$$\rho = \mathcal{D}_{A' \rightarrow A} \circ \mathcal{E}_{A \rightarrow A'}(\rho)$$

Proof. (reversibility \Rightarrow correlation-preserving) According to the quantum data processing inequality, a channel acting only on A cannot increase correlations between A and B :

$$I_{A:B}(\rho) \geq I_{A':B}(\mathcal{E}(\rho)) \geq I_{A:B}(\mathcal{D} \circ \mathcal{E}(\rho)) = I_{A:B}(\rho) \tag{4.3}$$

Thus $I_{A:B}(\rho) = I_{A':B}(\mathcal{E}(\rho))$.

(correlation-preserving \Rightarrow reversibility) Let W be an isometry from A to $A' \cup E$ that dilates the channel $\mathcal{E}_{A \rightarrow A'}$:

$$\mathcal{E}_{A \rightarrow A'}(\cdot) := \text{tr}_E [W(\cdot)W^\dagger], \quad (4.4)$$

where E is an ancillary system, and let $\sigma_{A'EB} = W\rho W^\dagger$. Then we have the following relation:

$$I_{A:B}(\rho) = I_{A'E:B}(\sigma_{A'EB}) = I_{A':B}(\sigma_{A'EB}). \quad (4.5)$$

The second equality, due to the correlation-preserving property, implies that $I_{B:E|A'}(\sigma_{A'EB}) = 0$ and $B - A' - E$ forms a quantum Markov chain. Thus there is a channel $\mathcal{T}_{A' \rightarrow A'E}$ that reconstructs $\sigma_{A'EB}$ from $\mathcal{E}_{A \rightarrow A'}(\rho) = \sigma_{A'B} = \text{tr}_E \sigma_{A'EB}$ alone:

$$\mathcal{T}_{A' \rightarrow A'E}(\sigma_{A'B}) = \sigma_{A'EB}. \quad (4.6)$$

The map $\mathcal{T}_{A' \rightarrow A'E}$ is the Petz recovery map [80]:

$$\mathcal{T}_{A' \rightarrow A'E}(\cdot) := \sigma_{A'E}^{1/2} \left(\sigma_{A'}^{-1/2}(\cdot) \sigma_{A'}^{-1/2} \otimes \mathbb{I}_E \right) \sigma_{A'E}^{1/2} \quad (4.7)$$

We can then choose the inverse channel \mathcal{D} to be

$$\mathcal{D}_{A' \rightarrow A}(\cdot) = \text{tr}_R \left(U_W^\dagger \mathcal{T}_{A' \rightarrow A'E}(\cdot) U_W \right), \quad (4.8)$$

where $U_W : A \cup R \rightarrow A' \cup E$ is a unitary operator that ‘completes’ the isometry $W : A \rightarrow A' \cup E$, namely:

$$W(\cdot)W^\dagger = U_W ((\cdot) \otimes |0\rangle_R \langle 0|) U_W^\dagger. \quad (4.9)$$

□

We remark that the relation between correlation-preserving and reversibility is robust in one direction. More precisely, if the channel $\mathcal{E}_{A \rightarrow A'}$ almost preserves correlation

$$I_{A:B}(\rho) - I_{A':B}(\mathcal{E}_{A \rightarrow A'}(\rho)) = \epsilon, \quad (4.10)$$

then there exists an almost perfect recovery channel $\mathcal{D}_{A' \rightarrow A}$ such that

$$F(\rho, \mathcal{D} \circ \mathcal{E}(\rho)) \geq 2^{-\epsilon/2}. \quad (4.11)$$

A proof, based on approximate quantum Markov chains [81], can be found in App.D.1.1. The robustness property is desirable especially when we would like to numerically search for the correlation-preserving channel \mathcal{E} .

When using \mathcal{E} for the purpose of coarse-graining, the target space of the channel should be as small as possible. This corresponds to solving the following optimization problem:

$$\begin{aligned} & \operatorname{argmin}_{\mathcal{E}_{A \rightarrow A'}} \dim \mathcal{H}_{A'} \\ & \text{s.t. } I_{A:\bar{A}}(\rho) - I_{A':\bar{A}}(\mathcal{E}(\rho)) \leq \epsilon \end{aligned} \quad (4.12)$$

with ϵ taken to be a small number or zero. The problem is analogous to Eq.(4.2) for pure states, which has Eq.(4.1) as an explicit solution. The current problem, in contrast, has no known explicit solution. In fact, the problem is closely related to the mixed-state quantum data compression problem, which is under active exploration in quantum information theory. We refer interested readers to Refs. [82, 83, 84, 85] for recent discussions on the problem.

To search for a good coarse-graining map for a given state, one can either numerically solve the optimization problem Eq.(4.12) (in this case the robustness property is crucial for the purpose of estimating error), or try to construct the channel analytically by exploiting the special structure of the given state, as we do later when studying examples in Sec.4.2.

We point out that two familiar coarse-graining schemes in 1D, one for quantum ground states and one for classical statistical mechanics models, are in fact correlation-preserving maps. The first one is the Hilbert space truncation reviewed in Sec.4.1.1 using the rule Eq.(4.1). Since this scheme preserves the entropy of a block, it satisfies the correlation-preserving condition (for a pure state $|\psi_{AB}\rangle$, $S_A = \frac{1}{2}I_{A:B}$). The other example is Kadanoff's block spin decimation of classical spin chains. Consider the Gibbs state of a classical spin chain with nearest-neighbor interaction, but written as a quantum mixed-state:

$$\rho_\beta \propto \sum_{\mathbf{s}=s_0\dots s_L} \exp\left(-\beta \sum_i h_i(s_i, s_{i+1})\right) |\mathbf{s}\rangle \langle \mathbf{s}| \quad (4.13)$$

The state is classical because it is diagonal in the computational basis $|\mathbf{s}\rangle = |s_1\dots s_L\rangle$. For each block $B = \{i_1, \dots, i_b\}$, the block spin decimation corresponds to a quantum channel that traces out all spins in B other than i_1 . This operation is correlation-preserving with respect to $B' := B \cup \{i_{b+1}\}$, because:

$$I_{B':\bar{B}'}(\rho) = I_{\{i_1, i_{b+1}\}:\bar{B}'}(\rho) \quad (4.14)$$

which is a consequence of the Markov property of the Gibbs distribution.

4.1.3 Ideal mixed-state RG

In this section, we formulate an ideal real-space RG scheme built from local correlation-preserving channels.

Assume ρ is a many-body mixed-state on a lattice with linear size L . We further assume that we have constructed, either numerically or analytically, a series of coarse-graining transformations $\{\mathcal{C}^{(0)}, \mathcal{C}^{(1)}, \dots, \mathcal{C}^{(\ell)}, \dots\}$ acting on ρ sequentially. In 1D, each $\mathcal{C}^{(\ell)}$ may have one of the structures shown in Fig. 4.1, or any other structure as long as it is composed of at most $O(1)$ -layer of local channels. This leads to an ‘RG flow’ of mixed-states:

$$\rho = \rho^{(0)} \xrightarrow{\mathcal{C}^{(0)}} \rho^{(1)} \xrightarrow{\mathcal{C}^{(1)}} \dots \xrightarrow{\mathcal{C}^{(\ell-1)}} \rho^{(\ell)} \xrightarrow{\mathcal{C}^{(\ell)}} \dots \quad (4.15)$$

along which the level of coarse-graining increases gradually.

Each state $\rho^{(\ell)}$ is supported on a coarse-grained lattice $\mathcal{L}^{(\ell)}$ with an $L^{(\ell)} := L/b^\ell$ linear size. The chain has a length at most $\sim \log_b L$, after which the state is supported on $O(1)$ number of sites.

We call this RG process *ideal* if every channel gate \mathcal{E} within each $\mathcal{C}^{(\ell)}$ is correlation-preserving with respect to its input and the prescribed bipartition.

As a direct consequence of Thm.2, ideal RG is reversible. More specifically, there exists a series of local ‘fine-graining’ transformations $\{\mathcal{F}^{(0)}, \mathcal{F}^{(1)}, \dots, \mathcal{F}^{(\ell)}, \dots\}$ that recovers the original mixed-state from its coarse-grained version by gradually adding local details:

$$\rho^{(0)} \xleftarrow{\mathcal{F}^{(0)}} \rho^{(1)} \xleftarrow{\mathcal{F}^{(1)}} \dots \xleftarrow{\mathcal{F}^{(\ell-1)}} \rho^{(\ell)} \xleftarrow{\mathcal{F}^{(\ell)}} \dots \quad (4.16)$$

where each $\mathcal{F}^{(\ell)}$ is the ‘reversed’ channel of $\mathcal{C}^{(\ell)}$, obtained by replacing each channel \mathcal{E} within $\mathcal{F}^{(\ell)}$ by its corresponding recovery map \mathcal{D} (see Thm.2). In graphical notation, if

$$\mathcal{C}^{(\ell)} = \left(\dots \begin{array}{c} \parallel \\ \boxed{\mathcal{E}_1} \\ \parallel \end{array} \begin{array}{c} \parallel \\ \boxed{\mathcal{E}_2} \\ \parallel \end{array} \begin{array}{c} \parallel \\ \boxed{\mathcal{E}_3} \\ \parallel \end{array} \begin{array}{c} \parallel \\ \boxed{\mathcal{E}_4} \\ \parallel \end{array} \dots \right) \quad (4.17)$$

then

$$\mathcal{F}^{(\ell)} := \left(\dots \begin{array}{c} \parallel \\ \boxed{\mathcal{D}_1} \\ \parallel \end{array} \begin{array}{c} \parallel \\ \boxed{\mathcal{D}_2} \\ \parallel \end{array} \begin{array}{c} \parallel \\ \boxed{\mathcal{D}_3} \\ \parallel \end{array} \begin{array}{c} \parallel \\ \boxed{\mathcal{D}_4} \\ \parallel \end{array} \dots \right) \quad (4.18)$$

In both plots, the state ($\rho^{(\ell)}$ for $\mathcal{C}^{(\ell)}$ and $\rho^{(\ell+1)}$ for $\mathcal{F}^{(\ell)}$), is inserted from the bottom.

Coarse-graining and fine-graining maps also establish relations between operators at different coarse-graining levels. Let $O^{(\ell)}$ be any operator (not necessarily local) defined on the lattice $\mathcal{L}^{(\ell)}$. Then the following relation holds:

$$\begin{aligned} \text{tr} (\rho^{(\ell)} O^{(\ell)}) &= \text{tr} (\mathcal{F}^{(\ell)} \circ \mathcal{C}^{(\ell)}(\rho^{(\ell)}) O^{(\ell)}) \\ &= \text{tr} (\rho^{(\ell+1)} \mathcal{F}^{(\ell)}(O^{(\ell)})), \end{aligned} \quad (4.19)$$

where \mathcal{F}^\dagger is \mathcal{F} 's dual map, defined through the relation $\text{tr}(A \cdot \mathcal{F}(B)) \equiv \text{tr}(\mathcal{F}^\dagger(A) \cdot B)$. Thus we can define the coarse-grained operator of $O^{(\ell)}$ through:

$$O^{(\ell+1)} := \mathcal{F}^\dagger(O^{(\ell)}) \quad (4.20)$$

so that:

$$\langle O^{(\ell)} \rangle^{(\ell)} = \langle O^{(\ell+1)} \rangle^{(\ell+1)} \quad (4.21)$$

where $\langle \cdot \rangle^{(\ell)} := \text{tr}(\rho^{(\ell)}(\cdot))$.

It is worth noting that $\mathcal{F}^\dagger = \mathcal{F}^{(\ell)\dagger}$ does not preserve operator multiplication: if $O^{(\ell)} = o_1^{(\ell)} o_2^{(\ell)}$ then it is possible that $\mathcal{F}^\dagger(O^{(\ell)}) = O^{(\ell+1)} \neq o_1^{(\ell+1)} o_2^{(\ell+1)} = \mathcal{F}^\dagger(o_1^{(\ell)}) \mathcal{F}^\dagger(o_2^{(\ell)})$. However, if two operators o_1 and o_2 are spatially well-separated, then the multiplication is preserved:

$$\mathcal{F}^\dagger(o_1^{(\ell)} o_2^{(\ell)}) = \mathcal{F}^\dagger(o_1^{(\ell)}) \mathcal{F}^\dagger(o_2^{(\ell)}) \quad (4.22)$$

Here ‘well-separated’ means that the lightcones for o_1 and o_2 , as determined by the circuit structure of $\mathcal{C}^{(\ell)}$ (or equivalently that of $\mathcal{F}^{(\ell)\dagger}$), are non-overlapping. We illustrate the definition of the lightcone and a proof of the above equation in App.D.1.2. This guarantees that long-distance behavior of all the k -point functions are preserved along an ideal RG:

$$\langle o_1^{(\ell)} o_2^{(\ell)} \dots o_k^{(\ell)} \rangle^{(\ell)} = \langle o_1^{(\ell+1)} o_2^{(\ell+1)} \dots o_k^{(\ell+1)} \rangle^{(\ell+1)} \quad (4.23)$$

where $\{o_i\}$ are mutually well-separated local operators.

4.1.4 From mixed-state RG to mixed-state quantum phases

In this section we discuss how to use RGs, both ideal and non-ideal ones, to furnish the two-way LC transformations required to establish the phase equivalence of two mixed states (Def.2).

Assume that for the state of interest ρ , we have found a (not necessarily ideal) real-space RG process $\{\mathcal{C}^{(1)}, \mathcal{C}^{(2)}, \dots, \mathcal{C}^{(\ell)}, \dots\}$. We further assume that the RG has a well-defined fixed-point state $\rho^{(\infty)}$, whose mixed-state phase of matter is presumably easy to identify.

Intuitively, this RG can be treated as an LC transformation connecting ρ to $\rho^{(\infty)}$ ³. To rigorously show this according to Defs.1 and 2, one needs to show that the sequence $\{\rho^{(\ell)}\}$ converges toward $\rho^{(\infty)}$ fast enough. More concretely, we need to show that there exists ℓ^* such that:

³When discussing LC transformations in this section, we fix the reference lattice as the one that $\rho = \rho^{(0)}$ is defined upon. The renormalized state $\rho^{(\ell)}$ can be considered as supported on a sub-lattice with L/b^ℓ sites.

1. The channel $\mathcal{C}^{(\ell^*)} \circ \dots \circ \mathcal{C}^{(2)} \circ \mathcal{C}^{(1)}$ is an LC transformation. Noticing that $\mathcal{C}^{(\ell)}$ entails b^ℓ range of non-locality while an LC transformation can have at most $o(L)$ range, the condition is equivalent to requiring $\ell^* \lesssim \log L^\alpha$, for some $\alpha < 1$.
2. The state after ℓ^* iterations is close enough to $\rho^{(\infty)}$, namely $F(\rho^{(\ell^*)}, \rho^{(\infty)}) > 1 - \epsilon$ for a small ϵ .

We find that such an ℓ^* does exist in many cases when the fixed-point state $\rho^{(\infty)}$ has a finite correlation length. More specifically, in such cases, the fidelity function satisfies the form:

$$F(\rho^{(\ell)}, \rho^{(\infty)}) \simeq \exp(-\alpha \theta^{(\ell)} L^{(\ell)}) \quad (4.24)$$

for some $\alpha = O(1)$ and a positive coefficient $\theta^{(\ell)}$. Further, $\theta^{(\ell)}$ displays a power-law iteration relation under each coarse-graining step:

$$\theta^{(\ell+1)} \lesssim (\theta^{(\ell)})^\gamma \quad \text{when} \quad \theta^{(\ell)} \rightarrow 0_+ \quad (4.25)$$

for some coefficient $\gamma > 1$.

As detailed in the App.D.2, Eqs.(4.24),(4.25) guarantee that choosing

$$\ell^* \sim \log \log(L/\epsilon) \quad (4.26)$$

is sufficient to have $F(\rho^{(\ell^*)}, \rho^{(\infty)}) > 1 - \epsilon$. We remark that one can let ϵ be as small as $(\text{poly}L)^{-1}$ but still guarantee that ℓ^* steps of RG is a $(\text{polylog}L)$ -range LC transformation.

In the App.D.2 we show that conditions Eq.(4.24) and Eq.(4.25) hold for:

- 1D pure-state RG of a matrix product state
- Gibbs state of a classical statistical mechanics model flowing toward a non-critical fixed point
- All examples we study in Sec.4.2

So far in this section, we have shown that RG can be viewed as an LC transformation connecting ρ to $\rho^{(\infty)}$. Recalling that the phase equivalence is defined through two-way LC connections, we have to find another LC channel connecting $\rho^{(\infty)}$ to ρ to conclude that the two states are in the same phase.

If the RG is an ideal one, it is composed of correlation-preserving channels and thus reversible. In this case, the other direction comes from the ‘reversed’ RG process $\text{RG}^{-1} =$

$\{\mathcal{F}^{(1)}, \mathcal{F}^{(2)}, \dots, \mathcal{F}^{(\ell)}, \dots\}$ which we discussed in Sec.4.1.3. Similar to the forward RG, there is the issue of convergence concerning whether RG^{-1} can be treated as an LC transformation. But the discussion is completely parallel to the one for the forward RG. Thus in this case, the LC bi-connection is established as

$$\rho \xrightarrow{\text{RG}} \rho^{(\infty)} \xrightarrow{\text{RG}^{-1}} \rho \quad (4.27)$$

and we can conclude ρ and $\rho^{(\infty)}$ are in the same phase.

Next we discuss what we can learn from a non-ideal RG. One class of mixed states of significant interest is a long-range entangled pure-state $|\psi\rangle$ subject to local decoherence represented by an LC transformation, and an important question is whether or not the decohered state is in the same phase as $|\psi\rangle$. In this setting, one direction of the connection is already given by the decoherence. Therefore, if the RG (ideal or not) has $|\psi\rangle$ as the fixed point:

$$|\psi\rangle \xrightarrow{\text{decohere}} \rho \xrightarrow{\text{RG}} \rho^{(\infty)} = |\psi\rangle \langle \psi|, \quad (4.28)$$

then an LC bi-connection is established and ρ and $|\psi\rangle$ are in the same phase. But on the other hand, if the fixed-point is not in the same phase as $|\psi\rangle$, then we cannot determine ρ 's phase because no bi-connection is identified.

4.2 Overview of examples

In the remaining sections we use our formalism to understand the quantum phases of several many-body mixed-states of recent interest.

In all the examples, the mixed-state is obtained by ‘perturbing’ a long-range entangled pure state, either through incoherent noise or finite temperature. The question we address is whether the states before and after the perturbation are in the same phase.

The long-range entangled pure state is chosen to be either the Greenberger–Horne–Zeilinger (GHZ) state or Kitaev’s toric code state. In most examples, the LC circuits for identifying phases take the form of RG. The coarse-graining maps therein are either constructed according to the correlation-preserving criterion (Def.3), or inspired by decoders of quantum error correcting codes.

In the App.D.3 we include an example of a mixed symmetry-protected topological (SPT) state and its associated mixed-state RG.

4.3 Noisy GHZ states

The many-body GHZ state, defined as

$$|\text{GHZ}_L\rangle := \frac{1}{\sqrt{2}} (|0^{\otimes L}\rangle + |1^{\otimes L}\rangle), \quad (4.29)$$

has long-range entanglement, *i.e.* it can not be generated from a product state using any one-dimensional LU (or LC) transformation from a product state. In this section, we study the effect of dephasing noise on this state.

For convenience of analysis, we let $L = b^{\ell_{\max}}$ for some integer ℓ_{\max} and an odd integer b . The state can be rewritten as:

$$|\text{GHZ}_L\rangle = w_b^{\otimes b^{\ell_{\max}-1}} \cdot w_b^{\otimes b^{\ell_{\max}-2}} \dots w_b^{\otimes b^1} |+\rangle \quad (4.30)$$

where $w_b = |0^{\otimes b}\rangle\langle 0| + |1^{\otimes b}\rangle\langle 1|$ is an isometry and $|+\rangle = \frac{1}{\sqrt{2}}(|0\rangle + |1\rangle)$. This provides a tree tensor network representation of the state (see Fig.4.2), as well as a way of blocking sites when performing RG.

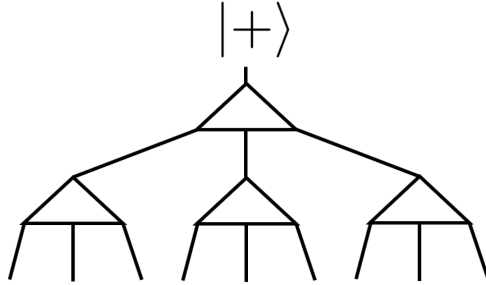


Figure 4.2: Tree tensor network of a GHZ state with $L = b^\ell = 9$, $b = 3$, $\ell = 2$. Each triangle represents an isometry w (Eq.(4.30)). By replacing the state at the top with a generic single qubit state $|\psi\rangle$, the same tensor network encodes $|\psi\rangle$ into a codeword state of the quantum repetition code.

We consider a setting in which each qubit experiences the same noise, as modeled by a single qubit channel \mathcal{N} , resulting in the mixed state

$$\rho_L := \mathcal{N}^{\otimes L}(|\text{GHZ}_L\rangle\langle \text{GHZ}_L|) \quad (4.31)$$

We remark that the GHZ state is closely related to the quantum repetition code, whose codespace is spanned by $|0^{\otimes L}\rangle$ and $|1^{\otimes L}\rangle$. It is known that quantum information stored

in a quantum repetition code is robust against bit-flip noise (X dephasing noise), but not phase-flip noise (Z dephasing noise). As we will see in this section, the robustness of the GHZ state's long-range entanglement has a parallel behavior when it is subjected to these two types of noise. We postpone a detailed discussion of the relation between mixed-state phases and quantum coding properties to Chap.5.

4.3.1 Bit-flip noise

We first consider dephasing each qubit in the X direction:

$$\mathcal{N}(\cdot) = \mathcal{N}_p^X(\cdot) := (1 - p)(\cdot) + pX(\cdot)X, \quad (4.32)$$

in which each qubit is flipped with probability p .

The resulting state is

$$\rho_{p,L}^X = \frac{1}{2} \sum_{\mathbf{s}} p^{|\mathbf{s}|} (1 - p)^{L-|\mathbf{s}|} (|\mathbf{s}\rangle \langle \mathbf{s}| + |\mathbf{s}\rangle \langle \bar{\mathbf{s}}| + |\bar{\mathbf{s}}\rangle \langle \mathbf{s}| + |\bar{\mathbf{s}}\rangle \langle \bar{\mathbf{s}}|) \quad (4.33)$$

where $|\mathbf{s}| := \sum_i s_i$ is the number of 1 in the bitstring \mathbf{s} , and $\bar{\mathbf{s}}$ is the bitwise complement of \mathbf{s} . Since $\rho_p^X = \rho_{1-p}^X$, we only consider $p \in (0, 0.5]$.

Inspired by decoders for the quantum repetition code, we use the b -qubit *majority-vote* channel as the coarse-graining map. To define it, we first introduce the unitary operator that re-parametrizes the bitstring:

$$U |\mathbf{s}\rangle := |\text{maj}(\mathbf{s})\rangle \otimes |\text{diff}(\mathbf{s})\rangle \quad (4.34)$$

where $\text{maj}(\mathbf{s})$ takes the majority vote of the bits within \mathbf{s} :

$$\text{maj}(\mathbf{s}) := \begin{cases} 0 & \text{if } |\mathbf{s}| < b/2 \\ 1 & \text{if } |\mathbf{s}| \geq b/2 \end{cases} \quad (4.35)$$

and $\text{diff}(\mathbf{s})$ is a length $(b - 1)$ bitstring that records pairwise difference of \mathbf{s} :

$$\text{diff}(\mathbf{s})_i := (s_{i+1} - s_i) \bmod 2 \quad i = 1, 2, \dots, b - 1 \quad (4.36)$$

Then the majority vote channel can be written as:

$$\mathcal{E}_b(\cdot) := \text{tr}_2(U(\cdot)U^\dagger) \quad (4.37)$$

where tr_2 denotes tracing out the pairwise difference information, regarded as unimportant short-distance degrees of freedom in the current example.

We inspect the state's RG flow under \mathcal{E}_b , the coarse-graining map:

$$\begin{aligned} & \mathcal{E}_b^{\otimes L/b}(\rho_{p,L}^X) \\ &= \mathcal{E}_b^{\otimes L/b} \circ (\mathcal{N}_p^X)^{\otimes L} (|\text{GHZ}_L\rangle \langle \text{GHZ}_L|) \\ &= (\mathcal{E}_b \circ (\mathcal{N}_p^X)^{\otimes b} \circ \mathcal{U}_{w_b})^{\otimes L/b} (|\text{GHZ}_{L/b}\rangle \langle \text{GHZ}_{L/b}|) \end{aligned} \quad (4.38)$$

where $\mathcal{U}_{w_b}(\cdot) := w_b(\cdot)w_b^\dagger$ and we applied the relation $|\text{GHZ}_L\rangle = w_b^{\otimes L/b} |\text{GHZ}_{L/b}\rangle$. Thus after one iteration of coarse-graining, the resulting state is a GHZ state with $1/b$ of the original size subject to a 'renormalized' noise channel, which is still X -dephasing (see App.D.1.3 for a derivation):

$$\mathcal{E}_b \circ (\mathcal{N}_p^X)^{\otimes b} \circ \mathcal{U}_{w_b} = \mathcal{N}_{p'}^X, \quad (4.39)$$

but with a renormalized noise strength $p' = \sum_{k=(b+1)/2}^b \binom{b}{k} p^k (1-p)^{b-k}$.

Thus we obtain an exact description of the state's RG flow:

$$\rho^{(\ell)} = (\mathcal{N}_{p^{(\ell)}}^X)^{\otimes L^{(\ell)}} (|\text{GHZ}_{L^{(\ell)}}\rangle \langle \text{GHZ}_{L^{(\ell)}}|) \quad (4.40)$$

where $L^{(\ell)} = Lb^{-\ell}$ is the renormalized system size at the ℓ -th iteration, and $p^{(\ell+1)} = \sum_{k=(b+1)/2}^b \binom{b}{k} (p^{(\ell)})^k (1-p^{(\ell)})^{b-k}$. It is straightforward to check that $p = 0$ and $p = 1/2$ are the two fixed points of the RG transformation.

Around $p = 1/2$, the iteration relation has the asymptotic behavior:

$$(p' - 1/2) \simeq g(b)(p - 1/2) \quad (4.41)$$

where $g(b) := \sum_{k=(b+1)/2}^b 4k \binom{b}{k} > 1$. Thus this is an unstable fixed point. Exactly at $p = 1/2$, the fixed-point state is:

$$\rho_{1/2, L}^X = \frac{1}{2^L} \sum_{\mathbf{s} \in \{0,1\}^L} (|\mathbf{s}\rangle \langle \mathbf{s}| + |\mathbf{s}\rangle \langle \bar{\mathbf{s}}|). \quad (4.42)$$

The state is better understood in the eigenbasis of Pauli X operators, *i.e.* $\{|0^X\rangle = \frac{1}{\sqrt{2}}(|0\rangle + |1\rangle), |1^X\rangle = \frac{1}{\sqrt{2}}(|0\rangle - |1\rangle)\}$:

$$\rho_{1/2, L}^X = \frac{1}{2^{L-1}} \sum_{\mathbf{s} \in \{0,1\}^L} |\mathbf{s}^X\rangle \langle \mathbf{s}^X| \delta(|\mathbf{s}| \equiv 0 \pmod{2}) \quad (4.43)$$

In this basis, the state is a uniform distribution of bitstrings with even parity. Since it is diagonal in this basis, the state is a classical state (recall the definition in Chap.1) and is not in the same phase as the GHZ state ⁴.

On the other hand, $p = 0$ is a stable fixed-point attracting $p \in [0, 0.5)$. Starting from any state in the interval, the RG process gradually removes entropy within the state and brings it back to the noiseless state at $p = 0$, *i.e.* $|\text{GHZ}\rangle$. We thus obtain the following LC transformation bi-connection:

$$|\text{GHZ}\rangle \xrightarrow{\mathcal{N}_X} \rho_p^X \xrightarrow{\text{RG}} |\text{GHZ}\rangle \quad p \in [0, 0.5) \quad (4.44)$$

Thus we can conclude ρ_p^X and $|\text{GHZ}\rangle$ are in the same phase. The analysis shows that the X -dephasing noise acts as an irrelevant perturbation with respect to the $|\text{GHZ}\rangle$ state and its long-range entanglement.

Besides establishing the phase equivalence, the bi-connection in Eq.(4.44) also yields information on the entanglement structure of the dephased state ρ_p^X . Consider two sufficiently large subregions of the system, referred to as A and B , for which one can always choose the RG blocking scheme such that coarse-graining channels never act jointly on A and B . Let $E_{A:B}(\cdot)$ be *any* quantum or classical correlation measure between A and B that satisfies the data processing inequality. Then due to the bi-connection we have:

$$\begin{aligned} E_{A:B}(|\text{GHZ}\rangle) &\geq E_{A:B}(\rho_p^X) \geq E_{A:B}(|\text{GHZ}\rangle) \\ \Rightarrow E_{A:B}(\rho_p^X) &= E_{A:B}(|\text{GHZ}\rangle). \end{aligned} \quad (4.45)$$

Some examples of correlation measures are quantum mutual information, entanglement negativity, and entanglement of formation & distillation. All quantities are easy to compute analytically for the GHZ state but are difficult to obtain for the mixed-state ρ_p^X by other means.

We point out that all conclusions in this section hold also for the dephasing noise along other directions in the X - Y plane. This can be most easily seen by noticing that the expression Eq.(4.39) holds for any dephasing direction in the X - Y plane. As we will see in the next subsection, the Z -dephasing acts very differently.

⁴In fact, the state $\rho_{1/2,L}^X$ is in the same phase as the product state. One may prepare the state using LC by first preparing a one dimensional cluster state of $2L$ spins and then tracing out qubits on all odd sites.

4.3.2 Phase-flip noise

Next we consider the GHZ state under another type of noise, namely the phase-flip or Z-dephasing:

$$\mathcal{N}_p^Z(\cdot) := (1-p)(\cdot) + pZ(\cdot)Z \quad (4.46)$$

which leads to the density matrix

$$\begin{aligned} \rho_{p,L}^Z = & \frac{1}{2} [|0^{\otimes L}\rangle \langle 0^{\otimes L}| + |1^{\otimes L}\rangle \langle 1^{\otimes L}| + \\ & (1-2p)^L (|0^{\otimes L}\rangle \langle 1^{\otimes L}| + |1^{\otimes L}\rangle \langle 0^{\otimes L}|)] \end{aligned} \quad (4.47)$$

In the thermodynamic limit, the off-diagonal term vanishes for any $p \notin \{0, 1\}$ and the state converges to a classical state $\frac{1}{2}(|0^{\otimes L}\rangle \langle 0^{\otimes L}| + |1^{\otimes L}\rangle \langle 1^{\otimes L}|)$. This already indicates that the state is in a different phase from the GHZ state.

To construct the RG for this mixed state, we still use the majority-vote channel \mathcal{E}_b (Eq.(4.37)) as the coarse-graining map. An important difference of this case compared to the bit-flip case is that the majority vote channel is now correlation-preserving with respect to $\rho_{p,L}^Z$. To see this, we first verify the following relations:

$$\begin{aligned} \mathcal{E}_b \circ \mathcal{U}_{w_b} &= \mathcal{I} \\ (\mathcal{N}_p^Z)^{\otimes b} \circ \mathcal{U}_{w_b} &= \mathcal{U}_{w_b} \circ \mathcal{N}_{p'}^Z \end{aligned} \quad (4.48)$$

where \mathcal{I} is the identity channel and p' is given later in Eq.(4.51). These equations imply that:

$$\mathcal{U}_{w_b} \circ \mathcal{E}_b(\rho_{p,L}^Z) = \rho_{p',L}^Z \quad (4.49)$$

where $\mathcal{U}_{w_b} \circ \mathcal{E}_b$ is applied to any block of b sites. Thus \mathcal{E}_b is reversible and correlation-preserving with respect to $\rho_{p,L}^Z$.

Following a similar calculation as in the bit-flip noise case, we obtain that the state after one step of RG maintains the same form:

$$\mathcal{E}_b^{\otimes L/b}(\rho_{p,L}^Z) = \rho_{p',L/b}^Z \quad (4.50)$$

but with a renormalized noise strength

$$p' = \frac{1}{2}(1 - (1 - 2p)^b), \quad (4.51)$$

The iteration relation has $p = 0$ as an unstable fixed point, around which $p' \simeq bp$, and also $p = 1/2$ as a stable fixed point, around which $(p' - 1/2) = (p - 1/2)^b$.

Since the RG is ideal, it leads to the following LC bi-connection:

$$\rho_{1/2}^Z \xrightarrow{\text{RG}^{-1}} \rho_p^Z \xrightarrow{\text{RG}} \rho_{1/2}^Z \quad p \in [0, 0.5) \quad (4.52)$$

and the analysis shows the noisy state is of the same phase as the classical state $\frac{1}{2}(|0^{\otimes L}\rangle\langle 0^{\otimes L}| + |1^{\otimes L}\rangle\langle 1^{\otimes L}|)$. Therefore, for the GHZ state the phase flip noise is relevant and destroys the long-range entanglement therein with an arbitrarily small strength.

4.4 Thermal toric code state

In this section and the next, we discuss two mixed-states related to \mathbb{Z}_2 topological order. In Sec.4.4.1 we review key properties of the toric code model and define the notations. In Sec.4.4.2 we construct an ideal RG to explicitly show that any finite temperature Gibbs state of the toric code is in the trivial phase.

4.4.1 Review of the toric code model

We consider a square lattice with periodic boundary conditions and qubits on the links. Kitaev's toric code model has the Hamiltonian

$$H = - \sum_{\square \in P} A_{\square} - \sum_{+ \in V} B_{+} \quad (4.53)$$

where $A_{\square} = \prod_{i \in \square} X_i$ and $B_{+} = \prod_{i \in +} Z_i$. P, V represent plaquettes and vertices, respectively.

Since all terms in the Hamiltonian commute with each other, their common eigenstates can be used to label the Hilbert space. But in order to construct a complete basis, we need two more operators $\tilde{X}_{1,2} = \prod_{i \in S_{1,2}} X_i$, where S_1, S_2 are the two homotopically inequivalent non-contractable loops on the torus. Each \tilde{X}_i commutes with A_{\square} s and B_{+} s, thus all of them together define a basis for the Hilbert space:

$$|\mathbf{m} = m_1 \dots m_{|P|}; \mathbf{e} = e_1 \dots e_{|V|}; \mathbf{l} = l_1 l_2\rangle, \quad m_i, e_i, l_i \in \{0, 1\} \quad (4.54)$$

satisfying

$$\begin{aligned} A_{\square_i} |\mathbf{m}; \mathbf{e}; \mathbf{l}\rangle &= (-1)^{m_i} |\mathbf{m}; \mathbf{e}; \mathbf{l}\rangle \\ B_{+_i} |\mathbf{m}; \mathbf{e}; \mathbf{l}\rangle &= (-1)^{e_i} |\mathbf{m}; \mathbf{e}; \mathbf{l}\rangle \\ \tilde{X}_i |\mathbf{m}; \mathbf{e}; \mathbf{l}\rangle &= (-1)^{l_i} |\mathbf{m}; \mathbf{e}; \mathbf{l}\rangle \end{aligned} \quad (4.55)$$

We call this the anyon number basis in contrast to the computational basis. If $m_i = 1$, there is a plaquette anyon (or m anyon) at the corresponding plaquette; while if $e_i = 1$, there is a vertex anyon (or e anyon) at the corresponding vertex. The operator identities $\prod_{\square} A_{\square} = 1$ and $\prod_{+} B_{+} = 1$ enforce that the total number of either type of anyon must be even:

$$\pi(\mathbf{m}) = 0 \quad \pi(\mathbf{e}) = 0, \quad (4.56)$$

where the function $\pi(\cdot)$ evaluates the total parity of a bit string, *i.e.* $\pi(\mathbf{s}) := (\sum_i s_i \bmod 2)$.

The Hamiltonian's 4-dimensional ground state subspace V is spanned by anyon-free states:

$$V := \text{span}\{ |\mathbf{m} = \mathbf{0}; \mathbf{e} = \mathbf{0}; \mathbf{l}\rangle : \mathbf{l} \in \{00, 01, 10, 11\} \} \quad (4.57)$$

States within this subspace are locally indistinguishable, *i.e.* $\rho_A = \text{tr}_{\bar{A}}(|\psi\rangle\langle\psi|)$ is independent of $|\psi\rangle \in V$ whenever A is a topologically trivial region.

We define a mixed-state ρ to be in the toric code phase if it is LC bi-connected to states within V , namely:

$$\rho_a \xrightarrow{\mathcal{C}_1} \rho \xrightarrow{\mathcal{C}_2} \rho_b \quad (4.58)$$

for some states ρ_a, ρ_b within V , and some LC transformations $\mathcal{C}_1, \mathcal{C}_2$.

4.4.2 RG of the thermal toric code state

We consider the Gibbs state of the toric code model Eq.(4.53) $\rho_{\beta} \propto \exp(-\beta H)$ at inverse temperature β . Ref. [34] showed that this state for finite β is not long-range entangled, and here we reproduce the conclusion by constructing an ideal mixed-state RG under which the state flows to a trivial one.

We notice that the density matrix ρ_{β} is diagonal in the anyon number basis (Eq. (4.54)):

$$\rho_{\beta} |\mathbf{m}; \mathbf{e}; \mathbf{l}\rangle \propto |\mathbf{m}; \mathbf{e}; \mathbf{l}\rangle, \quad (4.59)$$

and is thus a classical mixture of different anyon configurations, with probabilities

$$\begin{aligned} \text{Pr}(\mathbf{m}, \mathbf{e}, \mathbf{l}) &:= \langle \mathbf{m}; \mathbf{e}; \mathbf{l} | \rho_{\beta} | \mathbf{m}; \mathbf{e}; \mathbf{l} \rangle \\ &= \text{Pr}_m(\mathbf{m}) \text{Pr}_e(\mathbf{e}) \text{Pr}_l(\mathbf{l}) \end{aligned} \quad (4.60)$$

in which the three types of degrees of freedom are independent:

$$\begin{aligned}
\Pr_m(\mathbf{m}) &= C_\beta \delta(\pi(\mathbf{m}) = 0) \prod_i p_\beta^{m_i} (1 - p_\beta)^{1 - m_i} \\
\Pr_e(\mathbf{e}) &= C_\beta \delta(\pi(\mathbf{e}) = 0) \prod_i p_\beta^{e_i} (1 - p_\beta)^{1 - e_i} \\
\Pr_l(\mathbf{l}) &= 1/4
\end{aligned} \tag{4.61}$$

with $p_\beta = \frac{e^{-\beta}}{e^\beta + e^{-\beta}}$ and C_β a normalization constant.

The key property is that m anyons on each plaquette (and e anyons on vertices) are independently excited with probability p_β , up to a global constraint that the total number of each anyon type is even. This allows us to find an ideal RG, as we need only preserve the local anyon parity $\pi(\mathbf{m}_B), \pi(\mathbf{e}_B)$ of a block B to maintain correlations between the block and its complement.

We now describe how to coarse-grain to preserve this parity information. Consider the following quantum channel acting on 12 qubits in a 2×2 block of plaquettes:

$$\mathcal{E}^X(\cdot) := \sum_{\mathbf{m} \in \{0,1\}^{\otimes 4}} U_{\mathbf{m}} P_{\mathbf{m}}(\cdot) P_{\mathbf{m}} U_{\mathbf{m}}^\dagger \tag{4.62}$$

where $P_{\mathbf{m}}$ is the projector to the subspace with anyon configuration \mathbf{m} , and the unitary operator $U_{\mathbf{m}}$ is a product of Pauli Z matrices that brings $|\mathbf{m} = m_1 m_2 m_3 m_4\rangle$ to $|\pi(\mathbf{m})000\rangle$. For instance, if we assume plaquettes are labeled as $\frac{1}{3} \frac{2}{4}$ and $\mathbf{m} = 0110$, then $U_{\mathbf{m}}$ can be $Z_{12} Z_{13}$, where $Z_{12(13)}$ is the Pauli- Z matrix acting on the qubit separating 1 and 2 (1 and 3). We remark that $U_{\mathbf{m}}$ only acts on the inner four qubits.

In other words, \mathcal{E}^X first measures the anyon configuration within the block and then applies a unitary gate depending on the measurement outcome that pushes all anyons to the top-left plaquette. Since m -anyon is its own anti-particle, the top-left plaquette ends up with $\pi(\mathbf{m})$ anyons while the other three end up with 0. Importantly, neither step disturbs the distribution of e -anyons.

\mathcal{E}^X is a correlation-preserving map with respect to the state ρ_β , and one can explicitly check that its action on ρ_β can be reversed by the following channel:

$$\mathcal{D}^X(\cdot) := \sum_{\mathbf{m}} \Pr(\mathbf{m} | \pi(\mathbf{m})) U_{\mathbf{m}}^\dagger P_{\pi(\mathbf{m})}^1(\cdot) P_{\pi(\mathbf{m})}^1 U_{\mathbf{m}} \tag{4.63}$$

where P_x^1 is the projector to the subspace with $m_1 = x$. The action of \mathcal{D}^X can be intuitively understood as follows: It first measures the anyon occupancy of the site 1, which we

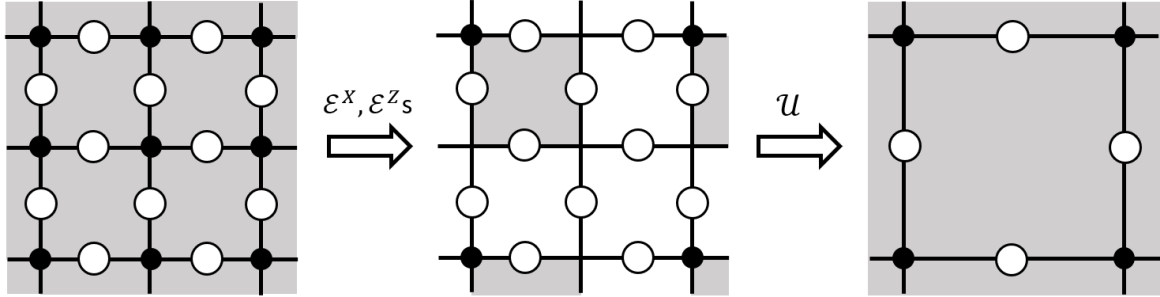


Figure 4.3: **RG scheme for the thermal toric code state**— In all panels, a plaquette (vertex) is shaded (dotted) if has a non-zero probability of holding an m - (e -) anyon, and physical qubits are associated with edges of the lattice and drawn as circles. (left→mid) \mathcal{E}^X and \mathcal{E}^Z (see Eq.(4.62) and Eq.(4.64)) acts on each 2×2 block of plaquettes and vertices, respectively. The resulting state has anyons on one of its sublattices' plaquettes and vertices. (mid→right) After disentangling with the unitary \mathcal{U} depicted in Eq.(4.65) and discarding the decoupled qubits, the new state is still a toric code Gibbs state, but with renormalized temperature p' (Eq.(4.67)) supported on a coarse-grained lattice.

recall is the only site that may host an anyon after the action of \mathcal{E}^X . Then based on the measurement outcome (referred to as x), it randomly generates an anyon configuration on the block according to the distribution $\Pr(\mathbf{m}|\pi(\mathbf{m}) = x)$.

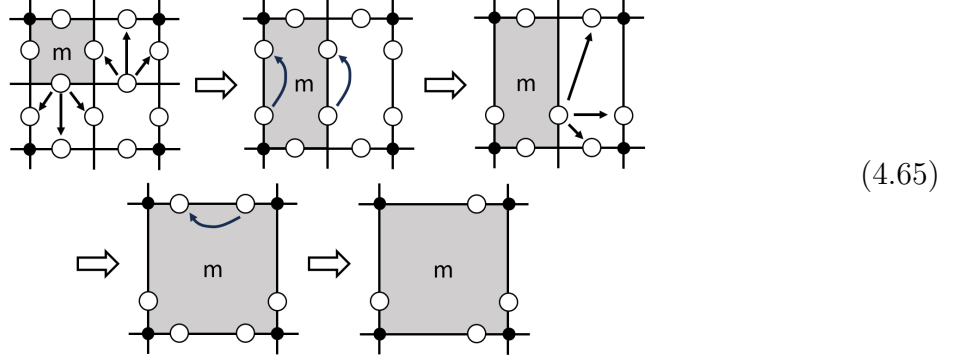
Analogously, there is a channel for each 2×2 block of vertices (*i.e.* a block of plaquettes of the dual lattice) that coarse-grains e -anyons:

$$\mathcal{E}^Z(\cdot) := \sum_{\mathbf{e} \in \{0,1\}^{\otimes 4}} U_{\mathbf{e}} P_{\mathbf{e}}(\cdot) P_{\mathbf{e}} U_{\mathbf{e}}^{\dagger} \quad (4.64)$$

where $P_{\mathbf{e}}$ are projector for e -anyon configurations and $U_{\mathbf{e}}$ a product of X operators that brings $|\mathbf{e} = e_1 e_2 e_3 e_4\rangle$ to $|\pi(\mathbf{e})000\rangle$. \mathcal{E}^Z only moves e -anyons and commutes with \mathcal{E}^X .

After applying $\mathcal{E}^{X(Z)}$ to each block of plaquettes (vertices), the resulting state only has anyons on plaquettes and vertices corresponding to a sublattice (see Fig.4.3, middle panel). To complete one iteration of the RG, we need to discard some degrees of freedom and put the state on a coarse-grained lattice. This step can be achieved by a series of local unitary operators called elementary moves introduced in [86, 87].

This step is most easily described graphically:



At each step, multiple controlled-not gates are applied, represented with arrows from the control qubit to target qubit. These gates decouple qubits into a product state which can then be removed, and the remaining qubits form a toric code state with anyons on a coarser lattice. Operations shown in each panel are applied in parallel to all the 2×2 blocks on the lattice.

In summary, one iteration of the RG consists of:

$$\mathcal{C} = \mathcal{U} \circ \left(\bigotimes_{B \in \mathcal{B}'} \mathcal{E}_B^Z \right) \circ \left(\bigotimes_{B \in \mathcal{B}} \mathcal{E}_B^X \right) \quad (4.66)$$

where \mathcal{B} contains 2×2 blocks of plaquettes and \mathcal{B}' contains 2×2 blocks of vertices. \mathcal{U} stands for the disentangling operations in Eq.(4.65).

After one step of RG, a plaquette (vertex) contains an anyon if and only the four plaquettes (vertices) it was coarse-grained from contain an odd number of anyons. The renormalized state is still a thermal toric code state, but with a renormalized probability (or renormalized temperature):

$$\begin{aligned} p'_{\beta'} &= 4p_{\beta}(1 - p_{\beta})^3 + 4p_{\beta}^3(1 - p_{\beta}) \\ \Leftrightarrow \tanh \beta' &= \tanh^4 \beta \end{aligned} \quad (4.67)$$

We thus conclude that any finite temperature state $\rho_{\beta < \infty}$ flows to the infinite temperature one $\rho_{\beta=0}$ under the RG.

Furthermore, since all channels in the RG are correlation-preserving with respect to their inputs, the RG is ideal and can be reversed. Thus there is the following bi-connection:

$$\rho_{\beta=0} \xrightarrow{\text{RG}^{-1}} \rho_{\beta} \xrightarrow{\text{RG}} \rho_{\beta=0} \quad \beta < \infty \quad (4.68)$$

Since the infinite temperature state $\rho_{\beta=0} \propto \mathbb{I}$ is in the trivial phase, we conclude that ρ_{β} is also in the trivial phase.

Chapter 5

Mixed-state phases and quantum error correction

The notion of quantum topologically ordered phases has close connection to quantum error correction. In this chapter, we consider two closely related questions in this context: 1. When subjecting a topological quantum code to noise, how is its decodability property related to its mixed-state phases? 2. How to use known decoders for topological codes to inspire LC connections required for proving phase equivalence?

Our primary example is the dephased toric code state. All notations in the chapter follow those introduced in Sec.4.4.1. The toric code model can be viewed as a quantum memory that stores quantum information in its ground state subspace V . In Sec.5.1, we discuss the relation between the preservation of logical information and the preservation of the phase of matter. We prove that if an LC transformation \mathcal{C} does not bring a pure toric code state out of its phase, then \mathcal{C} must preserve any quantum information stored in V . In Sec.5.2 and 5.3, we describe two ways to show that the dephased toric code state is in the toric code phase when dephasing strength is small. Both methods are inspired by well-studied decoders (the Harrington decoder and the minimal weight perfect matching decoder) for the toric code.

5.1 Logical information and long-range entanglement

The toric code model, as its name suggests, is naturally a quantum error correcting code whose codespace is the ground state subspace V (Eq.(4.57)). In this context, an important

question is whether a noise channel \mathcal{N} destroys logical information stored in a quantum memory. Mathematically, this is equivalent to asking whether there exists a recovery channel \mathcal{R} such that:

$$\mathcal{R} \circ \mathcal{N}(|\psi\rangle\langle\psi|) = |\psi\rangle\langle\psi| \quad \forall |\psi\rangle \in V. \quad (5.1)$$

In quantum error correction, \mathcal{R} is often realized by a *decoder*, which maps any input state into an output supported within V ¹. If such \mathcal{R} exists, we say the logical information is preserved by \mathcal{N} . Otherwise, we say the logical information is destroyed.

To relate the phase of the mixed state, as defined by two-way LC connection, to preservation of logical information, we will need to first prove the following theorem.

Theorem 3. Let V be the code subspace of a toric code defined on a torus. Suppose \mathcal{C} is a local channel transformation satisfying $\text{supp } \mathcal{C}(|\psi\rangle\langle\psi|) \subseteq V \quad \forall |\psi\rangle \in V$, then \mathcal{C} 's action when restricted to V is a unitary channel.

To gain some intuition for why locality of the channel is essential in the theorem, consider the following channel:

$$\mathcal{N}(\rho) := \frac{1}{2}\rho + \frac{1}{2}\tilde{X}_1\rho\tilde{X}_1 \quad (5.2)$$

where $\tilde{X}_1 = \prod_{i \in S_1} X_i$ is the logical X operator of the first encoded qubit (see Sec.4.4.1). \mathcal{N} is not an LC transformation: $\mathcal{N}(|0\rangle^{\otimes L}\langle 0|^{\otimes L}) = \frac{1}{2}(|0\rangle^{\otimes L}\langle 0|^{\otimes L} + |1\rangle^{\otimes L}\langle 1|^{\otimes L})$, a non-trivial mixed-state with long-range correlations. Furthermore, \mathcal{N} preserves V , but its action within V is dephasing the first logical qubit, which is not a unitary action.

We now prove the Thm.3.

Proof. \mathcal{C} can be dilated into an LU circuit U that acts jointly on the physical qubits (referred to as P) and the ancilla qubits (referred to as A). Consider U 's action on a codeword state:

$$|\psi; \mathbf{0}\rangle := |\psi\rangle_P |\mathbf{0}\rangle_A \xrightarrow{U} |\phi\rangle_{PA} \quad (5.3)$$

where $|\psi\rangle$ is any code word state in V . For later convenience we define the expanded codespace V_0 , which is the subspace of \mathcal{H}_{PA} spanned by $\{|\psi\rangle_P |\mathbf{0}\rangle_A\}_{|\psi\rangle \in V}$. We use V_0 to refer to both the subspace and the code defined by it. V_0 is still a stabilizer code, whose stabilizers are those of V combined with $\{Z_i : i \in A\}$.

¹Since we are only concerned about in-principle recoverability of logical information, we assume all operations within \mathcal{R} are noiseless.

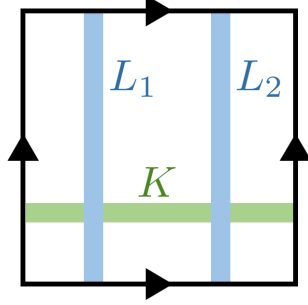


Figure 5.1: Geometry of operators L_1 , L_2 , and K .

Let L_1 and L_2 be two Pauli logical operators of the toric code that act in the same way in the code subspace V (see Fig. 5.1). Thus $L_1 L_2$ is a stabilizer of the toric code. Since \mathcal{C} preserves the code subspace, we have:

$$\langle \phi | L_1 L_2 | \phi \rangle = \text{tr}(C(|\psi\rangle \langle \psi|) L_1 L_2) = 1 \quad (5.4)$$

This leads to:

$$\langle \psi; \mathbf{0} | L_1^U L_2^U | \psi; \mathbf{0} \rangle = 1 \quad (5.5)$$

where $L_i^U := U^\dagger L_i U$ has support on both P and A , and is not necessarily a Pauli operator. Recalling that $L_1^U L_2^U$ is a unitary operator and the above expression holds for any $|\psi; \mathbf{0}\rangle$, we conclude that $L_1^U L_2^U$ acts as logical identity in the extended codespace V_0 .

To proceed, we assume the spatial separation between L_1 and L_2 to be much larger than the range of U , so that L_1^U and L_2^U are also well-separated.

We claim that both L_1^U and L_2^U are logical operators of V_0 . Otherwise, there needs to be a codeword state $|a\rangle \in V_0$ such that $L_1^U |a\rangle \notin V_0$. This implies at least one stabilizer S of V_0 is violated by the state: $\langle a | (L_1^U)^\dagger S L_1^U |a\rangle \neq 1$, and S must have spatial overlap with L_1^U . Further, since L_2^U is far from both L_1^U and S ,

$$\langle a | (L_1^U L_2^U)^\dagger S L_1^U L_2^U |a\rangle \neq 1 \quad (5.6)$$

But this cannot be true because $L_1^U L_2^U |a\rangle = |a\rangle$ and S is a stabilizer.

The same reasoning applies to any Pauli logical operator, referred to as K , whose spatial support is perpendicular to $L = L_1$ (see Fig. 5.1). By varying K and L , their product $R = K \cdot L$ can represent all of the 15 inequivalent Pauli logical operators of the toric code. We fix such a set: $\mathcal{P} = \{R_1, R_2, \dots, R_{15}\}$. The image of \mathcal{P} under $R \rightarrow R^U$ is a set of 15 logical operators of V_0 , as we just proved. Furthermore, since the map $R \rightarrow R^U$

preserves all the multiplication and commutation relations, we know \mathcal{P}^U must act as a set of 15 inequivalent Pauli logical operators on V_0 , up to a basis rotation.

We consider the part of R_i^U (or R_i) when restricted to the codespace V_0 (or V):

$$\begin{aligned}\Pi_{V_0} R_i^U &= \widetilde{R}_i^U \otimes |\mathbf{0}\rangle \langle \mathbf{0}| \\ \Pi_V R_i &= \widetilde{R}_i\end{aligned}\tag{5.7}$$

where \widetilde{R}_i^U and \widetilde{R}_i are operators acting within V only. Π_V is the projector to the subspace V and $\Pi_{V_0} = \Pi_V \otimes |\mathbf{0}\rangle \langle \mathbf{0}|$. As explained, both $\{\widetilde{R}_i\}$ and $\{\widetilde{R}_i^U\}$ realize the algebra of Pauli operators in the logical space.

We have:

$$\begin{aligned}\mathcal{C}(\widetilde{R}_i^U) &= \text{tr}_A(U(\widetilde{R}_i^U \otimes |\mathbf{0}\rangle \langle \mathbf{0}|)U^\dagger) \\ &= \text{tr}_A(U(R_i^U \Pi_{V_0})U^\dagger) \\ &= \text{tr}_A(R_i U \Pi_{V_0} U^\dagger) \\ &= R_i \mathcal{C}(\Pi_V) \\ &= \widetilde{R}_i \mathcal{C}(\Pi_V)\end{aligned}\tag{5.8}$$

The second to last equality holds because R_i is supported on P only, while the last one holds because $\text{supp } \mathcal{C}(\Pi_V) \subseteq V$ by assumption.

On the *r.h.s.* of the second equality above R_i^U and Π_{V_0} commute. Thus if we change their order then the same derivation gives:

$$\mathcal{C}(\widetilde{R}_i^U) = \mathcal{C}(\Pi_V) \widetilde{R}_i\tag{5.9}$$

Since the relation holds for any $i \in \{1, \dots, 15\}$ and $\text{supp } \mathcal{C}(\Pi_V) \subseteq V$, we know $\mathcal{C}(\Pi_V) \propto \Pi_V$. Further, since \mathcal{C} is trace-preserving, we have $\mathcal{C}(\Pi_V) = \Pi_V$. Thus:

$$\mathcal{C}(\widetilde{R}_i^U) = \widetilde{R}_i\tag{5.10}$$

This implies that when restricted to V , $\mathcal{C}(\cdot)$ is a *-isomorphism and must be a unitary channel. \square

We use the theorem to explore the relation between the phase of the noisy toric code state and the preservation of quantum information stored.

Consider a toric code's codeword state $|\psi\rangle \in V$. Suppose \mathcal{N}_ψ is an LC transformation that preserves the toric code phase. By definition, there exists another LC transformation \mathcal{D}_ψ such that $\text{supp } \mathcal{D}_\psi \circ \mathcal{N}_\psi(|\psi\rangle) \subseteq V$ ². We first point out that the pair $(\mathcal{N}_\psi, \mathcal{D}_\psi)$ satisfies

$$\mathcal{D}_\psi \circ \mathcal{N}_\psi(|\psi'\rangle \langle\psi'|) \subseteq V \quad \forall |\psi'\rangle \in V, \quad (5.11)$$

which we prove in App.???. Since the choice of $(\mathcal{N}_\psi, \mathcal{D}_\psi)$ does not depend on the codeword state $|\psi\rangle$, we drop the ψ subscript henceforth.

The channel $\mathcal{D} \circ \mathcal{N}$ thus satisfies the condition in Thm.3, according to which we have

$$\mathcal{D} \circ \mathcal{N}(|\psi\rangle \langle\psi|) = U |\psi\rangle \langle\psi| U^\dagger \quad \forall |\psi\rangle \in V \quad (5.12)$$

for some logical unitary operator U .

We thus conclude that if the noise \mathcal{N} preserves the toric code phase, then it also preserves the logical information stored. In particular, the recovery map can be chosen as $R(\cdot) = U^\dagger \mathcal{D}(\cdot) U$.

We consider a more detailed scenario where the channel $\mathcal{N} = \mathcal{N}_p$ has a strength parameter p . When the noise is very strong, both the toric code phase and the logical information stored should be destroyed. Thus one can define two critical noise strengths: $p_{\text{t.c.}}$, beyond which the noisy state is no longer in the toric code phase; and p_{coding} , beyond which the stored logical information is no longer recoverable. The previous analysis shows that

$$p_{\text{t.c.}} \leq p_{\text{coding}} \quad (5.13)$$

Namely, the loss of logical information must occur after transitioning out of the toric code phase.

If there is a gap between $p_{\text{t.c.}}$ and p_{coding} , then the noisy state $\mathcal{N}_p(|\psi\rangle \langle\psi|)$ for $p \in (p_{\text{t.c.}}, p_{\text{coding}})$ is not in the toric code phase but still contains logical information. In this case, the corresponding recovery map \mathcal{R} that recovers logical information must be non-LC.

5.2 LC transformation from the Harrington decoder

We illustrate these general results in a specific example, for which we construct explicit LC transformation inspired by the Harrington decoder [88]. We consider a toric code ground state $|\text{t.c.}\rangle \in V$ subject to phase-flip noise with strength p (Eq.(4.32)):

$$\rho_p := (\mathcal{N}_p^Z)^{\otimes L} (|\text{t.c.}\rangle \langle\text{t.c.}|) \quad (5.14)$$

²We emphasize that the condition should not be $\mathcal{D}_\psi \circ \mathcal{N}_\psi(|\psi\rangle) = |\psi\rangle$, according to our definition of the toric code phase in Sec.4.4.1

We ask whether the state is in the same phase as $|t.c.\rangle$, when p is small.

It is convenient to work in the anyon number basis Eq.(4.54), and since all states in this example are in the e -anyon-free subspace, we omit the \mathbf{e} labeling henceforth. An Z operator acting on a qubit on an edge will create a pair of anyons in the two plaquettes adjacent to the edge. But if two anyons meet in the same plaquette, they annihilate. Thus if we fix the set of edges acted on by Z , then anyons appear on faces adjacent to an odd number of Z s (see Fig.5.3).

The noisy state is a classical mixture of anyon configurations which differ significantly from those of the Gibbs state. When p is sufficiently small, the typical size of an error cluster is much smaller than the typical distance between clusters. The errors create anyons at the boundary of each cluster.

This picture suggests that by locally identifying clusters and pairing up anyons therein, one can remove all errors if p is sufficiently small. This intuition underlies the design of several decoding algorithms for the toric code [89, 90, 91, 88], which aim to pair up anyons such that the quantum information stored in the code remains intact. As we show now, these decoders can be modified into RG schemes to reveal mixed-state phases of the noisy toric-code states.

We construct a simplified version of the Harrington decoder for the toric code [88, 91] to demonstrate that ρ_p and $|t.c.\rangle$ are in the same phase when p is small. We first partition the lattice into even blocks $\mathcal{B}_{\text{even}}$ and odd blocks \mathcal{B}_{odd} (see Fig.5.2). Odd blocks are obtained by translating even blocks by one lattice spacing in both spatial directions. The two types of blocks will play different roles: coarse-graining will occur on even blocks and anyons will be paired up within odd blocks, regarded as boundary regions of even blocks.

Each step of the RG is composed of three layers of local channels:

$$\mathcal{C} = \mathcal{U} \circ \left(\bigotimes_{B \in \mathcal{B}_{\text{even}}} \mathcal{E}_B^X \right) \circ \left(\bigotimes_{B \in \mathcal{B}_{\text{odd}}} \mathcal{G}_B \right) \quad (5.15)$$

where the final step \mathcal{U} is the disentangling operation depicted in Eq.(4.65), and \mathcal{E}^X is the coarse-graining channel defined in Eq.(4.62).

The main difference between this RG scheme and the one for the thermal toric code state (see Sec.4.4.2) is the introduction of \mathcal{G}_B . \mathcal{G}_B annihilates all anyons within B only if there are an even number of them; otherwise it leaves anyons within B unmodified:

$$\mathcal{G}_B := \sum_{\mathbf{m} \in \{0,1\}^{\otimes 4}} \tilde{U}_{\mathbf{m}} P_{\mathbf{m}}(\cdot) P_{\mathbf{m}} \tilde{U}_{\mathbf{m}}^\dagger \quad (5.16)$$

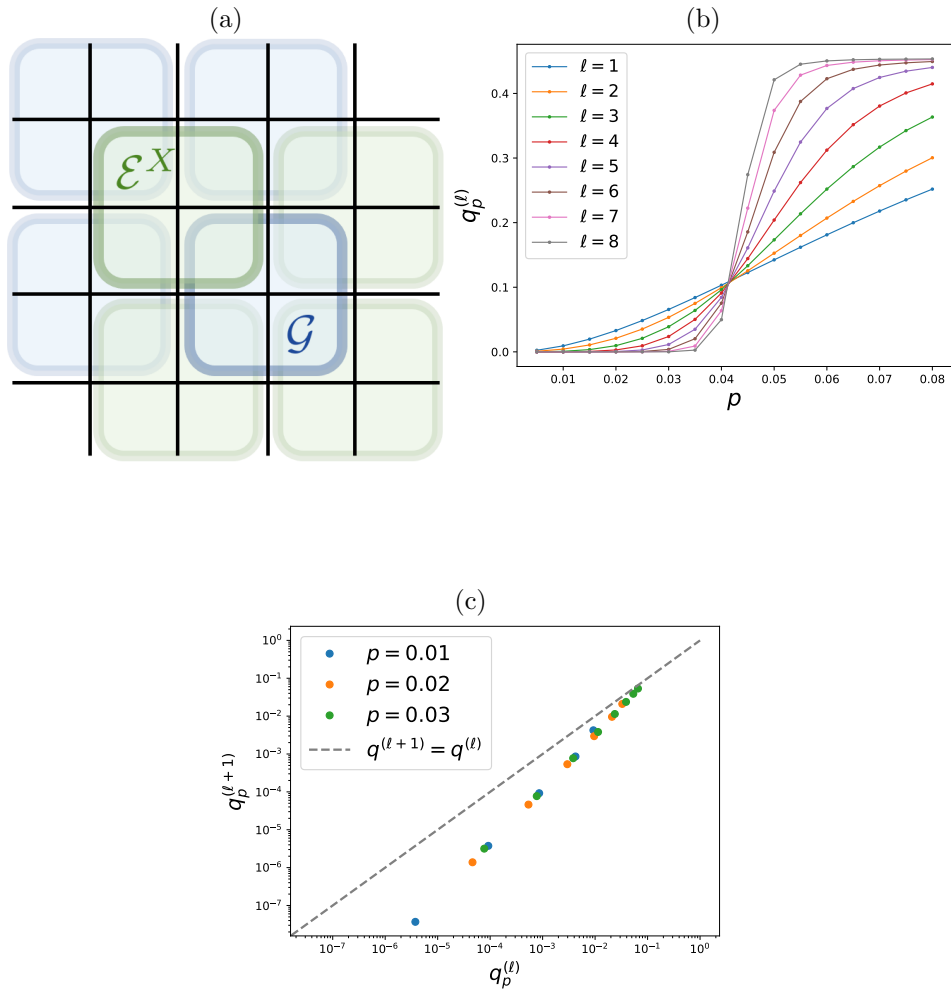


Figure 5.2: **RG of the dephased toric code state**– (a) In each RG iteration, \mathcal{G} is applied in parallel to all the odd blocks (blue), then \mathcal{E}^X is applied to all the even blocks (green). Finally disentangling unitaries (see Eq.(4.65), not drawn in the figure) are applied to reduce the lattice size by half. (b) RG flow of the anyon density $q_p^{(\ell)}$. (c) Iteration relation of $q_p^{(\ell)}$ when approaching 0, for various choices of p .

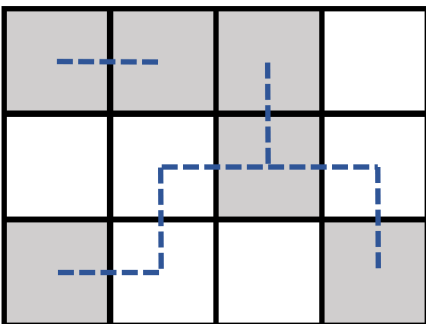


Figure 5.3: **A sample anyon configuration for noisy toric code**– A dashed line on an edge denotes the corresponding qubit’s phase is flipped by a Z operator. Anyons are created in plaquettes (shaded) where an odd number of dashed lines meet.

where $\tilde{U}_{\mathbf{m}}$ equals $U_{\mathbf{m}}$ (Eq.(4.62)) if $\pi(\mathbf{m}) = 0$, and is \mathbb{I} when $\pi(\mathbf{m}) = 1$. The heuristic reason for introducing \mathcal{G}_B is to pair up anyon clusters across the boundaries of the even blocks before the coarse-graining step. If such anyons were not paired, the coarse-graining on even blocks potentially prolongs them into clusters with a larger size, thus hindering effective anyon removal.

After each RG step \mathcal{C} , the new state is still an ensemble of different anyon configurations, albeit one that is not analytically tractable. Thus, we numerically compute how the RG steps affect the anyon density:

$$q_p^{(\ell)} = \frac{1}{|P^{(\ell)}|} \sum_{\square \in P^{(\ell)}} \text{tr} \left(\rho_p^{(\ell)} \frac{1 - A_{\square}}{2} \right) \quad (5.17)$$

where $P^{(\ell)}$ is the set of plaquettes on the renormalized lattice and $\rho_p^{(\ell)}$ is the renormalized state after ℓ iterations. $q = 0$ implies the state is in the ground state subspace V of the toric code Hamiltonian Eq.(4.53).

We use Monte Carlo method to study the flow of $q_p^{(\ell)}$ under RG. The simulation (Fig.5.2 (b)) shows that there is a sharp transition of $q_p^{(\ell)}$ at $p_c \approx 0.041$:

$$\lim_{\ell \rightarrow \infty} q_p^{(\ell)} = \begin{cases} 0 & p < p_c \\ O(1) & p > p_c \end{cases} \quad (5.18)$$

When $p < p_c$ the RG successfully annihilates all anyons and the fixed-point state is in the ground state subspace of V ; while when $p > p_c$, the fixed-point state has finite anyon density.

Furthermore, when the anyon density $q^{(\ell)}$ approaches 0, it transforms under each RG step as (see Fig.5.2 (c)):

$$q^{(\ell+1)} \simeq (q^{(\ell)})^\gamma \quad (5.19)$$

for $\gamma > 1$. This behavior guarantees that a small number of iterations is sufficient for the convergence to the toric code ground state subspace.

We thus obtain the LC bi-connection:

$$|\text{t.c.}\rangle \xrightarrow{\text{noise}} \rho_p \xrightarrow{\text{RG}} |\text{t.c.'}\rangle \quad p < p_c \quad (5.20)$$

where $|\text{t.c.'}\rangle$ is another toric code state. This shows that ρ_p is in the same phase as the pure toric code state, when $p < p_c$ and therefore X -dephasing noise is an irrelevant perturbation to the topologically ordered phase.

We emphasize that this analysis does not show that ρ_p with $p > p_c$ is in a different phase, because no bi-connection has been identified with this decoder. In fact, in the next section, we will construct another local channel that establishes that the phase boundary of the toric code phase extends to a much higher p_c .

5.3 Truncated minimal weight perfect matching channel

The seminal work [86] showed that the dephased toric code state (Eq.(5.14)) retains its logical information up to a critical point $p_{\text{coding}} \approx 0.108$, by relating the coding phase transition to the ferromagnetic-paramagnetic transition in the random bond Ising model. A recovery channel called the maximal likelihood decoder [86, 92] decodes the logical information for any $p < p_{\text{coding}}$, but the channel is not an LC transformation.

The minimal weight perfect matching (MWPM) decoder is another decoder introduced in [86]. It has a decoding threshold $p_{\text{MWPM}} \approx 0.103$ very close to p_{coding} [93]. The MWPM decoder, as a quantum channel, is also not an LC transformation. In the rest of this section, we show that it is possible to approximate the MPWM decoder's action arbitrarily well with an LC transformation whenever $p < p_{\text{MWPM}}$. Consequently, we show that any dephased toric code state with $p < p_{\text{MWPM}}$ is in the toric code phase.

The core component of the MWPM decoder (henceforth referred to as $\mathcal{C}^{\text{MWPM}}$) is a classical algorithm that solves the MWPM problem, namely looking for an anyons pairing scheme that minimizes the total length of the strings connecting pairs. Afterward, the

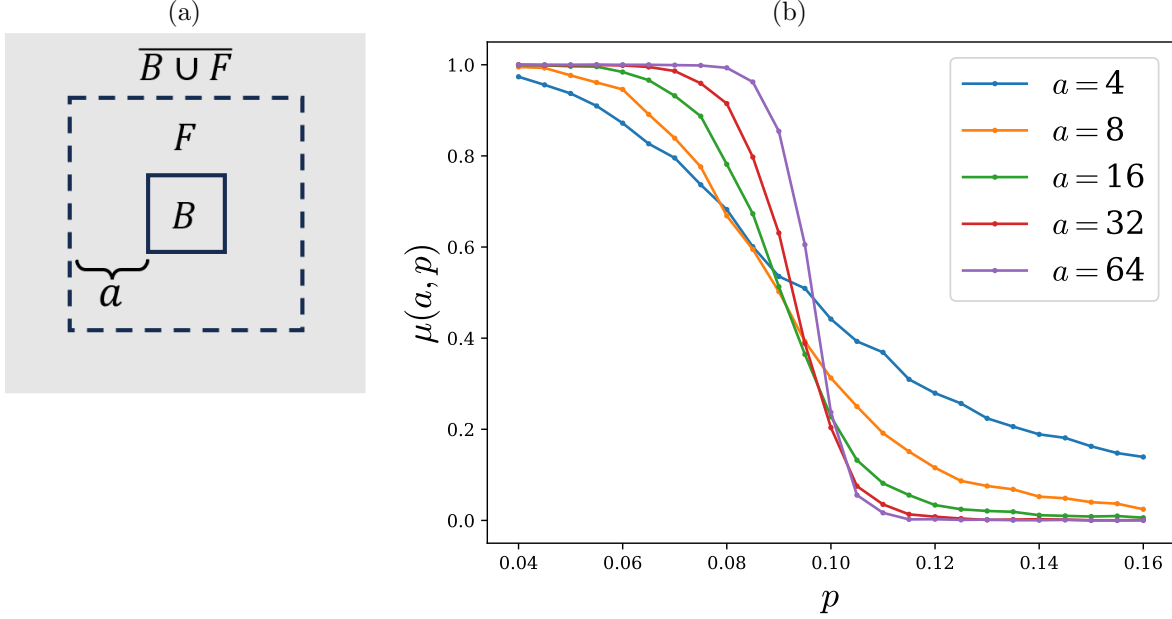


Figure 5.4: **Truncated minimum weight perfect matching channel**– (a) For a given block B , the corresponding channel $\mathcal{E}_{B,a}$ acts on both B and a buffer region F of a width a . (b) $\mu(a, p)$ is the probability that the truncated and global MWPM algorithms produce the same anyon pairings. It is plotted against p for various choices of a .

decoder annihilates each anyon pair by acting with the string of X operators connecting the pair.

We now devise a way to truncate the $\mathcal{C}^{\text{MWPM}}$ into an LC transformation. We first partition plaquettes into disjoint blocks, each with a size $b \times b$. For each block B , we apply a local channel $\mathcal{E}_{B,a}$ which acts jointly on B and a buffer region F of width a surrounding B (see Fig.5.4). The local channel first solves the MWPM of anyons within the truncated region $B \cup F$, with the additional requirement that each anyon can either pair with another anyon or with the outer boundary of F (the dashed line in Fig.5.4). Then given the pairing scheme suggested by the MWPM solution, the channel only accepts a subset of it, namely pairs with at least one anyon within B . The truncated MWPM (tMWPM) channel applies the above channel to every block:

$$\mathcal{C}_a^{\text{tMWPM}} := \prod_{B \in \mathcal{B}} \mathcal{E}_{B,a} \quad (5.21)$$

Note that different $\mathcal{E}_{B,a}$ can have overlapping domains. But since each $\mathcal{E}_{B,a}$ acts only on

a patch of $(b + 2a)^2$ qubits, we can always rearrange $\{\mathcal{E}_{B,a}\}$ into an $O((b + 2a)^2)$ -layer circuit so that each layer is composed of channels with non-overlapping domains. After the rearrangement, it is apparent that $\mathcal{E}_a^{\text{tMWPM}}$ is a range- $O((b + 2a)^4)$ LC transformation (because both the depth and the range of gate is $O((b + 2a)^2)$).

The assumption behind the design of the tMWPM channel is the existence of a correlation length $\xi(p)$, such that when $a \gg \xi(p)$, solving MWPM on $B \cup F$ only and solving MWPM on the whole system produce the same pairing for anyons in B . If the assumption holds for every block B , then the $\mathcal{C}_a^{\text{tMWPM}}$ pairs all anyons in the same way as $\mathcal{C}^{\text{MWPM}}$:

$$\mathcal{C}_a^{\text{tMWPM}}(\rho_p) \approx \mathcal{C}^{\text{MWPM}}(\rho_p) = |\text{t.c.}\rangle \quad a \gg \xi(p) \quad (5.22)$$

We provide a rough estimate of how large a needs to be for the ‘ \approx ’ above to hold (agreement between local and global MWPM with probability $1 - \epsilon$). Given the correlation length assumption, the probability that for a single block B the global and the truncated MWPM agrees should be $(1 - e^{-a/\xi(p)})$. Assuming these probabilities for different blocks are independent (which should hold for far apart blocks), then we need

$$(1 - e^{-a/\xi(p)})^{L^2/b^2} > 1 - \epsilon \quad (5.23)$$

which occurs when

$$a = \xi(p) O\left(\log \frac{L^2}{\epsilon}\right). \quad (5.24)$$

a diverges whenever $\xi(p)$ does, and this is expected to happen when $p \rightarrow p_{\text{MWPM}}$.

To numerically support the assumption that there exists a correlation length for MWPM, we sample anyon configurations in the X -dephased toric code state and solve the MWPM first for all the anyons, and then only for anyons within $B \cup F$ (Fig.5.4(a)). Then we compute the probability $\mu(a, p)$ that the two solutions are identical on B . We let both the system size L and the diameter of B be proportional to a , the width of the buffer F , so that the system has only one length scale a .

The simulation result is shown in Fig.5.4(b) and suggests there is a critical point p_{tMWPM} in the interval $(0.10, 0.11)$, presumably consistent with p_{MWPM} in the thermodynamic limit. Below p_{tMWPM} , we observe that $\lim_{a \rightarrow \infty} \mu(a, p) = 1$. This indicates that the MWPM solution within B is independent of anyons that are more than $O(\xi)$ away from B , for some correlation length ξ which diverges at p_{tMWPM} . tMWPM thus serves as a local channel which, along with the noise channel, establishes the two-way connection demonstrating the toric code phase up to $p_{\text{tMWPM}} \approx 0.1$. Above p_{tMWPM} , $\lim_{a \rightarrow \infty} \mu(a, p) = 0$, implying non-locality in the MPWM solution.

We point out that the simulation method above provides a way to detect the toric code phase using the anyon distribution data. One can fix a region B , implement MWPM on $B \cup F$, and gradually increase the buffer width a . If the MWPM solution when restricted to B becomes stationary after a is larger than some $a^* = O(1)$ with high probability, then the original mixed state is in the toric code phase because the tMWPM channel with $a \gtrsim a^* \log L$ can transform it into a pure toric code state. The method can potentially be used to detect mixed-state topological order in experiments.

5.4 Discussion and outlook

In this and the previous chapters, we provide two routes (real-space RG and truncated decoders) for constructing local channels connecting two mixed states to prove they are in the same phase. We formulated a real-space RG scheme for mixed states and proposed the correlation-preserving property as a guiding criterion for finding coarse-graining maps; this property is necessary and sufficient for the map's action to be reversible (Thm.2). We applied this formalism to identify the phases of several classes of mixed states obtained by perturbing a long-range entangled pure state with noise or finite temperature, and in particular we constructed an exact RG flow of the finite temperature 2D toric code state to infinite temperature.

For toric code subject to decoherence, we also established a relation between the mixed state phase of the toric code and the integrity of logical information. In Thm.3, we proved that if local noise preserves the long-range entanglement of the toric code (and the resulting mixed state remains within the same phase as toric code), it must also preserve logical information encoded in the initial pure state. We conjecture that the converse statement is also true, namely, if local noise destroys the long-range entanglement of toric code, it must also destroy any encoded logical information. Even though the theorem and subsequent discussion focused on the toric code state, the main proof idea generalizes to many other topological codes and their corresponding phases.

- After formalizing the definition of mixed-state phase, one natural question to ask is whether there is a nontrivial phase that has no pure state nor classical state in this phase. A promising candidate is the ZX-dephased toric code state recently studied in [94]. Since the state (when noise is strong) loses logical information [94], it is provably not in the toric code phase according to our Thm.3. Thus if the state is not in the trivial phase, it is an example of intrinsic mixed-state topological order. Another class of potential examples are decohered critical ground states [95, 96],

because such states naturally sit between a long-range entangled pure state and a long-range correlated classical state.

- One related question is whether one can find a computable quantity to detect non-trivial mixed-state phases. Topological entanglement negativity has been successfully used as a probe of mixed-state topological order [97, 98], but its robustness under LC transformations needs to be studied further.
- The decoherence-induced toric code transition can also be understood as a separability transition of the mixed-state [99], and it would be valuable to relate this perspective with the mixed state phase and local channel perspective.
- Pure state RG methods like DMRG serve as powerful computational methods for analyzing many-body systems. It is thus important to develop a numerical implementation of our mixed-state RG scheme. To facilitate simulations, one needs to first find an efficient representation of the mixed state (*e.g.* using tensor networks), then update it iteratively using exact or approximately correlation-preserving maps, obtained by solving the optimization problem Eq.(4.12). We leave this problem for future exploration.
- As presented in Sec.5.3, tMWPM also serves as a practical probe of the mixed state toric code phase using anyon measurements. However, in experiments imperfect measurements lead to a finite density of ‘fake’ anyons as well as unprobed anyons. To address this, one needs to consider a specific model of measurement errors and perform more than one round of measurements. Another potential direction is generalizing tMWPM to other topologically ordered mixed-state phases in two or higher dimensions.

Chapter 6

Markov length and mixed-state quantum phases

For quantum phases of Hamiltonian ground states, the energy gap plays a central role in ensuring the stability of the phase as long as the gap remains finite. In this chapter, we introduce Markov length, the length scale at which the quantum conditional mutual information (CMI) decays exponentially, as an equally essential quantity characterizing mixed-state phases and transitions.

6.1 Quantum conditional mutual information and Markov length

Quantum conditional mutual information is defined as:

$$I(A : C|B) \equiv S(AB) + S(BC) - S(A) - S(ABC) \quad (6.1)$$

where each $S(X) \equiv -\text{tr}(\rho_X \log \rho_X)$ is von Neumann entropy of the region X . For a annulus shaped tripartition (Fig.1), CMI is closely tied to the reversibility of Lindbladian evolution. CMI (for different partitions) has provided insight into ground state topological phases [100, 101, 102], quantum dynamics involving measurement and noise [2, 103, 104], and the efficiency of preparing and learning quantum states [105, 106, 107]. Here we use it to understand mixed state phases of matter. To gain some intuition, CMI can be written as a difference of mutual informations

$$I(A : C|B) = I(A : BC) - I(A : B), \quad (6.2)$$

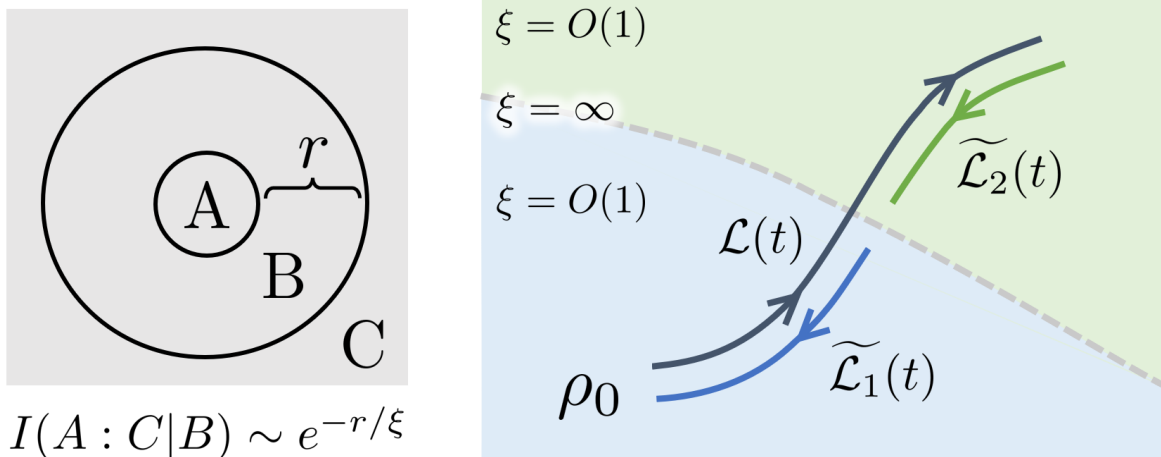


Figure 6.1: **(left)** Quantum conditional mutual information $I(A : C|B)$ quantifies how non-local is the correlation between A and its complement. When $I(A : C|B)$ decays exponentially with B 's width r , we call the corresponding length scale the Markov length ξ . **(right)** The dark grey line is a path of mixed-states generated from local Lindbladian evolution, *i.e.* $\rho_t = \mathcal{T} \exp(\int_0^t \mathcal{L}(\tau) d\tau) [\rho_0]$. For each segment in which ξ remains finite, *e.g.* below (above) the dashed line, we argue there exists a quasi-local Lindbladian $\tilde{\mathcal{L}}_{1(2)}$ that reverses \mathcal{L} 's action. Thus states within each segment are in the same mixed-state phase.

and thus small CMI implies that A 's correlation with its complement is mostly captured by a buffer region B surrounding it.

We give a formal definition of Markov length, the key quantity in this chapter. Let ρ be a state defined on a D -dimensional lattice. We say ρ has Markov length ξ if its conditional mutual information (CMI) satisfies

$$I_\rho(A : C|B) \leq \text{poly}(|A|, |C|) e^{-\text{dist}(A,C)/\xi} \quad (6.3)$$

for any three regions A, B, C with topology displayed in Fig.6.1(a), namely A is simply connected, B is an annulus-shaped region surrounding A , and $C = \overline{A \cup B}$ is the rest of the system. When ρ can be consistently defined on lattices of arbitrarily large size L (*e.g.* ρ is Gibbs state of some local Hamiltonian), and if ξ is independent of L , we say the state has ξ -finite-Markov-length (ξ -FML).

6.2 Reversing a local quantum operation

Assume a quantum channel \mathcal{E} acts on a local region A of state ρ , and let B be a width- r annulus region surrounding A . Can the effect of \mathcal{E} be approximately reversed by another quantum channel $\tilde{\mathcal{E}}$ acting on the enlarged region $A \cup B$?

Using the approximate data processing inequality [108], we prove there exists a map $\tilde{\mathcal{E}}$ acting on $A \cup B$ whose recovery quality satisfies (see SM for a derivation)¹:

$$\begin{aligned} \frac{1}{2 \ln 2} |\tilde{\mathcal{E}} \circ \mathcal{E}[\rho] - \rho|_1^2 &\leq I_\rho(A : C|B) - I_{\mathcal{E}[\rho]}(A : C|B) \\ &\leq I_\rho(A : C|B) \end{aligned} \quad (6.4)$$

where the second inequality follows from strong subadditivity and $|\sigma|_1 \equiv \text{tr}(\sqrt{\sigma^\dagger \sigma})$ is the trace norm. The explicit form of $\tilde{\mathcal{E}}$ is given by the twirled Petz recovery map $\tilde{\mathcal{E}} = \mathcal{P}(\mathcal{E}, \rho_{AB})$, defined as:

$$\mathcal{P}_{\mathcal{E}, \rho}[\cdot] = \int_{-\infty}^{\infty} f(\tau) \rho^{\frac{1-i\tau}{2}} \mathcal{E}^\dagger \left[\mathcal{E}[\rho]^{\frac{-1+i\tau}{2}} (\cdot) \mathcal{E}[\rho]^{\frac{-1-i\tau}{2}} \right] \rho^{\frac{1+i\tau}{2}} d\tau \quad (6.5)$$

which depends on the forward channel \mathcal{E} and the local reduced density matrix ρ_{AB} . The above bound shows that if ρ has ξ -FML, local recovery is possible because the recovery error $|\tilde{\mathcal{E}} \circ \mathcal{E}[\rho] - \rho|_1$ decays exponentially with r , the width of B .

Now we turn to the local reversibility of a continuous time evolution acting everywhere on an FML state. Generically, such dynamics can be represented as a time-dependent local Lindbladian evolution: $\mathcal{G} \equiv \mathcal{T} e^{\int_0^1 \mathcal{L}_\tau d\tau}$ where $\mathcal{L}_t \equiv \sum_x \mathcal{L}_{t,x}$ is a local Lindbladian at all time. But for technical simplicity, we consider a discretized (or ‘Trotterized’) Lindbladian dynamics:

$$\begin{aligned} \mathcal{G} &\equiv \mathcal{C}_{\ell=\delta t^{-1}} \circ \dots \circ \mathcal{C}_{\ell=2} \circ \mathcal{C}_{\ell=1} \\ \mathcal{C}_\ell &\equiv \prod_x \mathcal{E}_{\ell,x} = \prod_x e^{\delta t \mathcal{L}_{\ell,x}} \end{aligned} \quad (6.6)$$

Here each $\mathcal{L}_{\ell,x}$ is a Lindbladian superoperator acting on a region referred to as $A_{\ell,x}$, and x indexes gates within a layer and ℓ indexes time steps. For a given ℓ , different $A_{\ell,x}$ s are non-overlapping. Thus the total map \mathcal{G} takes the form of a circuit, whose gates are Lindbladian evolutions with a small time δt .

We show that \mathcal{G} ’s effect on ρ can be reversed by another (quasi-)local evolution $\tilde{\mathcal{G}}$ if ρ ’s Markov length remains finite throughout the dynamics \mathcal{G} . More precisely, we assume that for any $\ell \in \{1, \dots, \ell_{\max} = \delta t^{-1}\}$:

¹All the logarithms in this work, including those show up in the definition of entropic quantities, use 2 as the base.

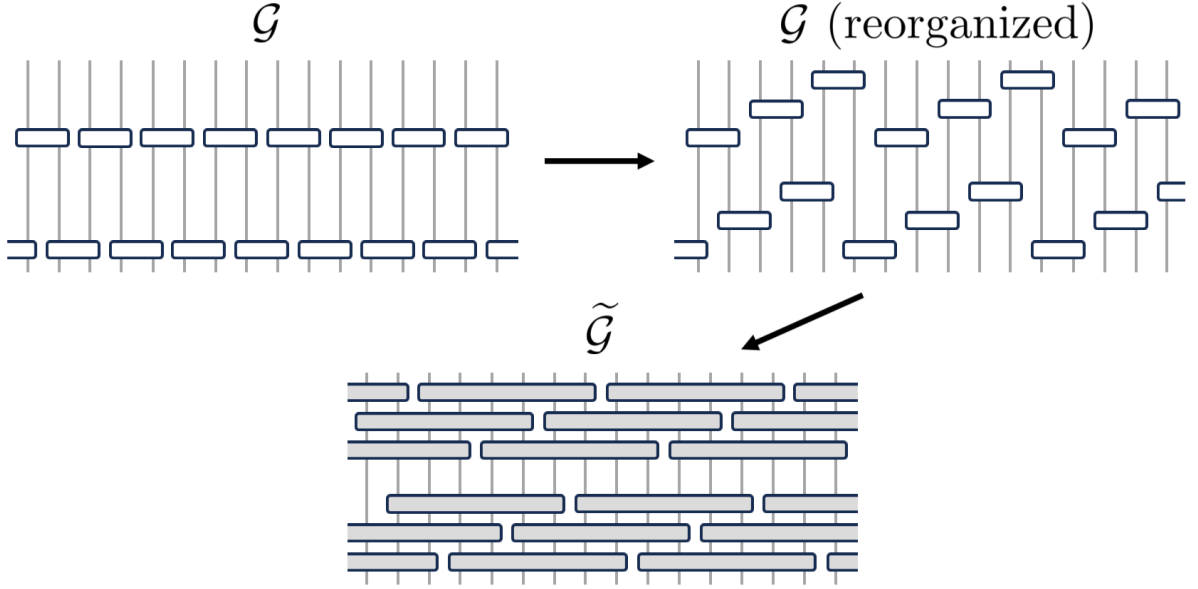


Figure 6.2: **Reversal circuit for continuous evolution**— (top left) Two layers of the forward circuit \mathcal{G} acting from bottom to top. Each box is a quantum channel $\mathcal{E}_{x,t} = \exp(\delta t \mathcal{L}_{x,t})$. (top right) Gates in each layer are reorganized into multiple layers so that any two gates in a layer are at least distance $2r$ separated (in the figure $r = 2$). (bottom) The reversal circuit $\tilde{\mathcal{G}}$ constructed from the reorganized \mathcal{G} by replacing each $\mathcal{E}_{x,t}$ with its reversal $\tilde{\mathcal{E}}_{x,t}$ (grey box) defined in Eq.(6.7). The reversal circuit acts from top to bottom.

1. $\rho_\ell \equiv \mathcal{C}_\ell[\rho_{\ell-1}]$ is ξ -FML (let $\rho_0 \equiv \rho$), and further
2. $\mathcal{C}'_\ell[\rho_{\ell-1}]$ is ξ -FML, for \mathcal{C}'_ℓ formed from any subset of gates within \mathcal{C}_ℓ

The (technical) second condition is expected to follow from the first condition and small enough δt ; it corresponds to the intuition that ξ does not suddenly change from being finite to infinite under a small perturbation. In the absence of a proof, we leave it as an assumption for the sake of rigor.

Now we describe the reversal circuit $\tilde{\mathcal{G}}$. The big picture is to reverse the circuit gate by gate using the recovery map described in the previous section in a carefully chosen order. To this end, we first reorganize the circuit structure of \mathcal{G} : for each layer \mathcal{C}_ℓ , we reorganize gates within it into multiple layers such that gates within each newly formed layer are at least distance $2r$ separated from each other (r is a distance parameter we will specify later). After the reorganization, the circuit depth may increase by a factor of $O(r^D)$, but the number of gates is unchanged. Importantly, the new circuit still satisfies aforementioned

conditions 1, 2 with respect to the state ρ for the same ξ (thanks to condition 2). With a slight abuse of notation, we still use $\{\mathcal{C}_\ell\}$ to denote layers in the reorganized circuit.

The reversal dynamics can be explicitly written as:

$$\begin{aligned}\tilde{\mathcal{G}} &\equiv \tilde{\mathcal{C}}_{\ell=1} \circ \tilde{\mathcal{C}}_{\ell=2} \circ \dots \circ \tilde{\mathcal{C}}_{\ell=\delta t-1} \\ \tilde{\mathcal{C}}_\ell &\equiv \prod_x \tilde{\mathcal{E}}_{\ell,x} \quad \tilde{\mathcal{E}}_{\ell,x} \equiv \mathcal{P}(\mathcal{E}_{\ell,x}, (\rho_{\ell-1})_{A_{\ell,x} \cup B_{\ell,x}})\end{aligned}\tag{6.7}$$

where each $\mathcal{E}_{\ell,x}$ acts on both $A_{\ell,x}$ and a width- r annulus $B_{\ell,x}$ surrounding $A_{\ell,x}$. We emphasize that each $\mathcal{E}_{\ell,x}$'s reversed channel $\tilde{\mathcal{E}}_{\ell,x}$ is calculated using $\rho_{\ell-1}$ as the reference state. Each $\tilde{\mathcal{E}}_{\ell,x}$ also admits a (time-dependent) Lindbladian representation, i.e. $\tilde{\mathcal{E}}_{\ell,x} = \mathcal{T} \exp(\int_0^{\delta t} d\tau \tilde{\mathcal{L}}_{\ell,x}(\tau))$, as shown in [109]. Thanks to the reorganization step, different $\tilde{\mathcal{E}}$ s are non-overlapping and thus commute with each other. This guarantees, as we show rigorously in the SM, that the cumulative recovery error is bounded by the sum of single-step errors, namely:

$$\epsilon \equiv |\tilde{\mathcal{G}} \circ \mathcal{G}[\rho] - \rho|_1 \leq \sum_{\ell,x} \left| \tilde{\mathcal{E}}_{\ell,x} \circ \mathcal{E}_{\ell,x} [\rho_{\ell-1}] - \rho_{\ell-1} \right|_1 .\tag{6.8}$$

Since each ρ_ℓ is ξ -FML, according to Eq.(6.4) each of the terms in the *r.h.s.* is bounded by $\text{poly}(L)e^{-r/2\xi}$ with L being the system size. In order to achieve the global recovery error ϵ , it suffices to require

$$r \geq \xi \cdot \log \left(\frac{\text{poly}(L)}{\epsilon \cdot \delta t} \right)\tag{6.9}$$

Thus a quasi-local ² reversal circuit is sufficient to achieve a high recovery fidelity. Using the definition of phase equivalence, we conclude that $\mathcal{G}[\rho]$ and ρ are in the same phase. We observe that the conclusion does not change even if we let ϵ and δt scale with the system size as $1/\text{poly}(L)$.

6.3 Example: dephased toric code

Given that finite ξ implies continuity of a phase, it is natural to expect that a phase transition occurs when ξ diverges. We demonstrate this with a concrete example: toric code topological order subject to dephasing noise.

²Naively the evolution time of the reversed dynamics $\tilde{\mathcal{G}}$ is $O(r^D)$ because the circuit depth is multiplied by the same factor due to the reorganization. However it can be turned into a time 1 evolution by absorbing the factor into $\mathcal{L}(\tau)$.

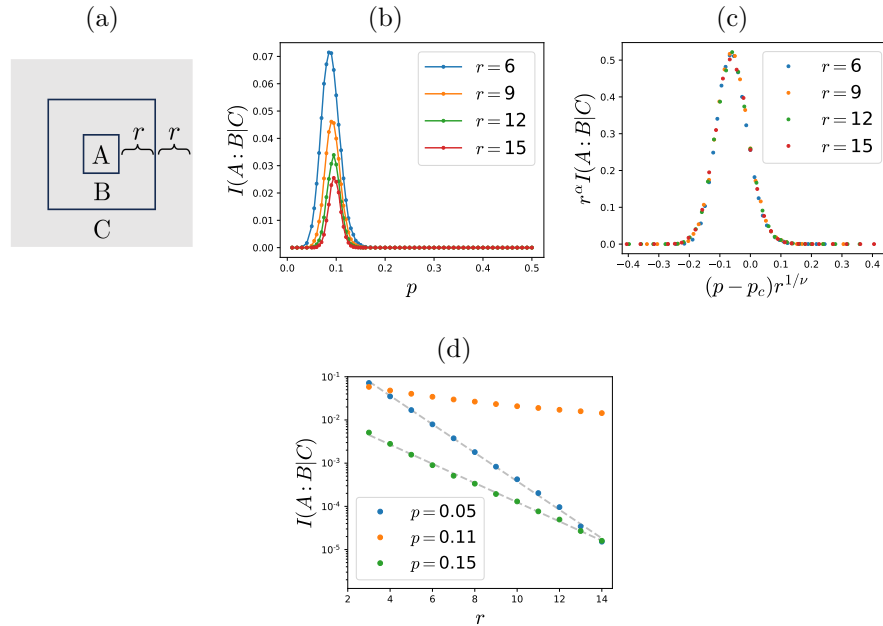


Figure 6.3: **CMI of dephased toric code state** — (a) Partition with A fixed and varying r (width of B, C). (b) $I(A : C|B)$ peaks around $p_c \approx 0.11$ and peak size decays with r . (c) Finite-size collapse with the scaling ansatz Eq.(6.14), with $(p_c, \nu, \alpha) = (0.11, 1.8, 1.1)$. (d) Above ($p = 0.15$) or below ($p = 0.05$) the critical point, CMI decays exponentially with r , in contrast to power-law decay at the critical point $p_c \approx 0.11$.

Let $|\text{t.c.}\rangle$ be a ground state of the toric code Hamiltonian:

$$H_{\text{t.c.}} = -\sum_{\square} A_{\square} - \sum_{+} B_{+}, \quad (6.10)$$

where qubits reside on edges of an $L \times L$ square lattice, and \square ($+$) are plaquettes (vertices). The two terms are $A_{\square} = \prod_{i \in \square} X_i$ and $B_{+} \equiv \prod_{i \in +} Z_i$ and all mutually commute. Thus the ground state satisfies all terms, *i.e.* $A_{\square} |\text{t.c.}\rangle = B_{+} |\text{t.c.}\rangle = |\text{t.c.}\rangle$.

After applying dephasing noise $\mathcal{E}_p[\cdot] \equiv (1-p)(\cdot) + pZ(\cdot)Z$ on each qubit, we obtain a mixed-state $\rho_p \equiv \mathcal{E}_p^{\otimes L^2} [|\text{t.c.}\rangle \langle \text{t.c.}|]$. Physically this corresponds to applying a Pauli- Z gate independently on each qubit with probability p . The channel can be realized by evolving the Lindbladian $\mathcal{L}[\rho] = \sum_i \frac{1}{2}(Z_i \rho Z_i - \rho)$ for time $t_p = -\ln(1-2p)$, with $t = \infty$ corresponding to $p = 0.5$.

The mixed state is concisely described by an anyon distribution. We say a plaquette \square is occupied by an anyon if $A_{\square} = -1$ (before decoherence, the ground state has no anyons). Once a Z operator acts on an edge, it flips the anyon occupancy on the two adjacent plaquettes. Thus for a fixed set of flipped qubits, the resulting state has anyons on plaquettes that contain an odd number of flipped links. The state ρ_p is a mixture of all compatible anyon configurations weighted by their probabilities. For a simply connected sub-region Q , its reduced density matrix is:

$$\begin{aligned} \rho_{p,Q} &= \sum_{\mathbf{m}_Q} \text{Pr}(\mathbf{m}_Q) \Pi_{\mathbf{m}_Q} \\ \text{Pr}(\mathbf{m}_Q) &\equiv \sum_{\mathbf{e}} p^{|\mathbf{e}|} (1-p)^{|Q|-|\mathbf{e}|} \delta(\mathbf{m}_Q = \partial \mathbf{e}) \end{aligned} \quad (6.11)$$

where the binary vector \mathbf{m}_Q indicates the anyon configuration of plaquettes within Q . $\Pi_{\mathbf{m}_Q}$ is the maximally mixed state that has anyon configuration \mathbf{m}_Q and satisfies $B_{+} = 1$ for all vertices.

After some algebra, one can show that region Q 's von Neumann entropy is

$$S(\rho_{Q,p}) = S(\rho_{Q,0}) + H(\mathbf{m}_Q), \quad (6.12)$$

$H(\mathbf{m}) \equiv -\sum_{\mathbf{m}} \text{Pr}(\mathbf{m}) \log \text{Pr}(\mathbf{m})$ being the Shannon entropy of the anyon distribution $\text{Pr}(\mathbf{m})$. If Q is not simply connected and contains a hole denoted Γ , the *r.h.s.* of Eq.(6.12) is replaced by $H(\mathbf{m}_Q, \pi(\mathbf{m}_{\Gamma}))$, with $\pi(\mathbf{m}_{\Gamma})$ being the parity of anyon number within Γ (see SM for details). Thus for an annulus-shaped A, B, C partition (Fig. 6.3(a)),

$$\begin{aligned} I(A : C|B) &= H(\mathbf{m}_{BC}, \pi(\mathbf{m}_A)) - H(\mathbf{m}_{ABC}) \\ &\quad - H(\mathbf{m}_B, \pi(\mathbf{m}_A)) + H(\mathbf{m}_{AB}). \end{aligned} \quad (6.13)$$

We simulate $I(A : B|C)$ in this geometry for various rs (*i.e.* width of B and C) and system sizes by representing $\Pr(\mathbf{m})$ as a two-dimensional tensor network and contracting it using the boundary transfer matrix technique [110, 111] (see SM).

We first focus on the parameter regime around the presumed critical point $p_c \approx 0.11$. Our results (Fig.6.1) show that for any system size r , CMI has a peak around p_c with height decreasing with r . Furthermore, data from different system sizes can be collapsed with the scaling ansatz:

$$I(A : C|B) = r^{-\alpha} \Phi((p - p_c)r^{1/\nu}) \quad (6.14)$$

by choosing $p_c = 0.11$, $\alpha = 1.1$ and $\nu = 1.8$. In particular, when $p = p_c$, CMI decays as a power-law with r , in contrast to mutual information and conventional correlation functions. To verify that the state is FML away from the critical point p_c , we pick two representative points below and above the threshold: $p = 0.05 < p_c$ and $p = 0.15 > p_c$. As shown in Fig.6.1(d), at both points CMI decays exponentially. These observations imply that in the large r limit:

$$I(A : C|B) \simeq \begin{cases} e^{-r/\xi_-(p)} & p < p_c \\ r^{-\alpha} & p = p_c \\ e^{-r/\xi_+(p)} & p > p_c \end{cases} \quad (6.15)$$

where $\xi_{\pm}(p)$ diverges near the critical point as $\xi_{\pm} \propto (p - p_c)^{-\nu}$.

Because the Markov length remains finite in $p \in [0, p_c)$ and $p \in (p_c, 0.5]$ ³, these intervals constitute two mixed-state phases. The former is a topologically ordered phase containing |t.c.>, and the latter is a trivial phase containing $\rho_{0.5} \propto \sum_{\mathbf{s} \in \text{loops}} |\mathbf{s}\rangle \langle \mathbf{s}|$, *i.e.* a classical uniform distribution of all closed-loop spin configurations. This state can be obtained by applying $\mathcal{G}_{\square}[\cdot] \equiv \frac{1}{2}(\cdot) + \frac{1}{2}A_{\square}(\cdot)A_{\square}$ on each plaquette \square of a product state $|\mathbf{0}\rangle \langle \mathbf{0}|$; thus it belongs to a trivial phase.

Similar to other aspects of decohered toric code studied in [86, 99, 98, 112], the behavior of CMI can also be understood in terms of the random bond Ising model (RBIM) along the Nishimori line [113]. Each term in Eq.(6.13) can be mapped to a free energy in RBIM (see SM for detailed mapping and RBIM definition). For instance, $H(\mathbf{m}_{AB}) = \overline{F_{\text{RBIM},p}(AB)} + c_1|AB| + c_2$, where $\overline{F_{\text{RBIM},p}(AB)}$ is the disorder-averaged free energy of the RBIM defined on region AB 's dual lattice, and $c_{1,2}$ are constants. For non-simply-connected regions B and BC , the central hole A is treated as a single dual lattice site in the corresponding RBIM. Since A is $O(1)$ -sized, from a coarse-grained point of view the CMI is:

$$I(A : C|B) = \overline{F_{\text{def}}(4r)} - \overline{F_{\text{def}}(2r)}, \quad (6.16)$$

³We remark that the $p = 0.5$ state requires infinite time dephasing Lindbladian evolution. But as we show in SM, a $O(\log L)$ time evolution is enough to obtain a sufficiently close-by state

where $\overline{F_{\text{def}}(x)}$ is the free energy cost of introducing a point defect at the center of RBIM on an $x \times x$ lattice. The two terms come from $H(\pi(\mathbf{m}_A), \mathbf{m}_{BC}) - H(\mathbf{m}_{ABC})$ and $H(\pi(\mathbf{m}_A), \mathbf{m}_B) - H(\mathbf{m}_{AB})$, respectively. The RBIM has ferromagnetic and paramagnetic phases, separated by a critical point presumably described by a conformal field theory, where $\overline{F_{\text{def}}(r)}$ has a subleading piece decaying as a power law with r . Thus we expect the scaling form Eq.(6.14) to originate from the RBIM critical point. As the correlation length is the only length scale near a critical point, we expect that the Markov length ξ can be identified with the RBIM's correlation length. We note however that our fitted exponent $\nu \approx 1.8$ deviates from $\nu_{\text{RBIM}} \approx 1.5$ reported in [114], and we leave this discrepancy, likely due to finite-size effects, for future work.

6.4 $\tilde{\mathcal{G}}$ as a quasi-local decoder

Using the mapping to RBIM as a bridge, we associate the dephased toric code's mixed-state phase transition to its decodability transition studied in [86], since both occur at the RBIM transition. In fact, our reversal channel allows us to make a stronger statement justified below: when the dephased toric code state is decodable (*i.e.* $p < p_c$), it can be decoded with a quasi-local process derived from $\tilde{\mathcal{G}}$.

When defined on a torus, the Hamiltonian Eq.(4.53) has a degenerate ground state subspace V which can store quantum information. We care about whether the information stored is decodable despite the noise $\mathcal{E}_p^{\otimes L^2}$, namely whether there exists a decoding channel \mathcal{D} satisfying $\mathcal{D} \circ \mathcal{E}_p^{\otimes L^2}[\rho] = \rho$, $\forall \rho \in \mathcal{B}_V$, the set of density operators on V . The reversal circuit $\tilde{\mathcal{G}}$ constructed earlier naturally induces a decoding channel. We invoke a theorem in [3], which states that if a quasi-local channel \mathcal{F} satisfies $\mathcal{F}[\mathcal{B}_V] \subseteq \mathcal{B}_V$, then $\mathcal{F}|_{\mathcal{B}_V}[\cdot] = U[\cdot]U^\dagger$ for some quasi-local unitary evolution U that leaves V invariant. Now we let $\mathcal{F} = \tilde{\mathcal{G}} \circ \mathcal{E}_p^{\otimes L^2}$, with $\tilde{\mathcal{G}}$ being the reversal circuit constructed from the forward dynamics $\mathcal{G} = \mathcal{E}_p^{\otimes L^2}$ and any $|\text{t.c.}\rangle \in V$ as initial state, using the strategy described earlier. Applying the theorem⁴, we conclude that $U^\dagger \tilde{\mathcal{G}}[\cdot]U$ is a decoding channel, and is quasi-local because both $U^\dagger[\cdot]U$ and $\tilde{\mathcal{G}}$ are quasi-local channels.

⁴The theorem is only rigorously proved for \mathcal{F} that exactly preserves \mathcal{B}_V ; nevertheless here we are applying it on a map $\tilde{\mathcal{G}} \circ \mathcal{G}$ which approximately preserves \mathcal{B}_V .

6.5 Discussions and outlook

We have shown that under a local Lindbladian evolution, a mixed state remains in the same phase of matter whenever its Markov length stays finite. Applying this diagnostic to the dephased toric code state and identifying the Markov length with the RBIM correlation length reveal that the mixed state phase transition and decoding transition precisely coincide and as a byproduct, furnishes a quasi-local decoding channel.

Our main result and methods can be readily generalized to mixed-state phases with symmetry, *e.g.* symmetry-protected topological (SPT) phases [115, 35, 116, 117, 118, 119, 120], since the reverse evolution is naturally symmetry respecting: $\tilde{\mathcal{G}}$ satisfies any strong (or weak) symmetry present in both the forward evolution \mathcal{G} and the initial state ρ . This derives from the same property of the Petz map $\mathcal{P}(\mathcal{E}, \rho)$, which is manifest from its definition (see SM).

Our discussion relies on paths of FML states from local Lindbladian evolution, which is only justified if FML states constitute extended regions under generic local Lindbladian evolutions, and non-FML states constitute a measure-zero set requiring fine-tuning (as depicted in Fig.6.1). Our work shows this is true in the case of dephased toric code, but understanding its generic validity is desirable.

The Markov length criteria for continuity of a phase also encompasses pure ground state phases, in which the Markov length should reduce to the correlation length that remains finite along a path of gapped parent Hamiltonians. It is worth exploring the role of Markov length in understanding phases of other types of mixed-states, *e.g.* Gibbs states and Lindbladian steady states. For the former case, FML property is rigorously established for several special cases [121, 122, 123], and is believed to be generically true at non-zero temperature. On the other hand, there are states with infinite Markov length which are unstable to certain Lindbladian perturbations, *e.g.* the Greenberger–Horne–Zeilinger (GHZ) state $|\text{GHZ}\rangle \propto |00\dots 0\rangle + |11\dots 1\rangle$ and critical ground states. It is worth understanding how infinite Markov length is related to the state’s instability.

References

- [1] Shengqi Sang and Timothy H. Hsieh. Measurement-protected quantum phases. *Phys. Rev. Res.*, 3:023200, Jun 2021.
- [2] Shengqi Sang, Zhi Li, Timothy H Hsieh, and Beni Yoshida. Ultrafast entanglement dynamics in monitored quantum circuits. *PRX Quantum*, 4(4):040332, 2023.
- [3] Shengqi Sang, Yijian Zou, and Timothy H Hsieh. Mixed-state quantum phases: Renormalization and quantum error correction. *arXiv preprint arXiv:2310.08639*, 2023.
- [4] Shengqi Sang and Timothy H Hsieh. Stability of mixed-state quantum phases via finite markov length. *arXiv preprint arXiv:2404.07251*, 2024.
- [5] Adam Nahum and Brian Skinner. Entanglement and dynamics of diffusion-annihilation processes with majorana defects, 2019.
- [6] KJ Satzinger, Y-J Liu, A Smith, C Knapp, M Newman, C Jones, Z Chen, C Quintana, X Mi, A Dunsworth, et al. Realizing topologically ordered states on a quantum processor. *Science*, 374(6572):1237–1241, 2021.
- [7] Giulia Semeghini, Harry Levine, Alexander Keesling, Sepehr Ebadi, Tout T Wang, Dolev Bluvstein, Ruben Verresen, Hannes Pichler, Marcin Kalinowski, Rhine Samajdar, et al. Probing topological spin liquids on a programmable quantum simulator. *Science*, 374(6572):1242–1247, 2021.
- [8] Non-abelian braiding of graph vertices in a superconducting processor. *Nature*, 618(7964):264–269, 2023.
- [9] Jesse C Hoke, Matteo Ippoliti, Dmitry Abanin, Rajeev Acharya, Markus Ansmann, Frank Arute, Kunal Arya, Abraham Asfaw, Juan Atalaya, Joseph C Bardin, et al.

Quantum information phases in space-time: measurement-induced entanglement and teleportation on a noisy quantum processor. *arXiv preprint arXiv:2303.04792*, 2023.

- [10] Jae-yoon Choi, Sebastian Hild, Johannes Zeiher, Peter Schauf, Antonio Rubio-Abadal, Tarik Yefsah, Vedika Khemani, David A Huse, Immanuel Bloch, and Christian Gross. Exploring the many-body localization transition in two dimensions. *Science*, 352(6293):1547–1552, 2016.
- [11] Xiao Mi, Pedram Roushan, Chris Quintana, Salvatore Mandra, Jeffrey Marshall, Charles Neill, Frank Arute, Kunal Arya, Juan Atalaya, Ryan Babbush, et al. Information scrambling in quantum circuits. *Science*, 374(6574):1479–1483, 2021.
- [12] Sepehr Ebadi, Tout T Wang, Harry Levine, Alexander Keesling, Giulia Semeghini, Ahmed Omran, Dolev Bluvstein, Rhine Samajdar, Hannes Pichler, Wen Wei Ho, et al. Quantum phases of matter on a 256-atom programmable quantum simulator. *Nature*, 595(7866):227–232, 2021.
- [13] Frank Arute, Kunal Arya, Ryan Babbush, Dave Bacon, Joseph C Bardin, Rami Barends, Rupak Biswas, Sergio Boixo, Fernando GSL Brandao, David A Buell, et al. Quantum supremacy using a programmable superconducting processor. *Nature*, 574(7779):505–510, 2019.
- [14] Han-Sen Zhong, Hui Wang, Yu-Hao Deng, Ming-Cheng Chen, Li-Chao Peng, Yi-Han Luo, Jian Qin, Dian Wu, Xing Ding, Yi Hu, et al. Quantum computational advantage using photons. *Science*, 370(6523):1460–1463, 2020.
- [15] Sepehr Ebadi, Alexander Keesling, Madelyn Cain, Tout T Wang, Harry Levine, Dolev Bluvstein, Giulia Semeghini, Ahmed Omran, J-G Liu, Rhine Samajdar, et al. Quantum optimization of maximum independent set using rydberg atom arrays. *Science*, 376(6598):1209–1215, 2022.
- [16] Barbara M Terhal. Quantum error correction for quantum memories. *Reviews of Modern Physics*, 87(2):307, 2015.
- [17] Hans J Briegel, David E Browne, Wolfgang Dür, Robert Raussendorf, and Maarten Van den Nest. Measurement-based quantum computation. *Nature Physics*, 5(1):19–26, 2009.
- [18] Dorit Aharonov. Quantum to classical phase transition in noisy quantum computers. *Physical Review A*, 62(6):062311, 2000.

- [19] Yaodong Li, Xiao Chen, and Matthew PA Fisher. Quantum zeno effect and the many-body entanglement transition. *Physical Review B*, 98(20):205136, 2018.
- [20] Brian Skinner, Jonathan Ruhman, and Adam Nahum. Measurement-induced phase transitions in the dynamics of entanglement. *Physical Review X*, 9(3):031009, 2019.
- [21] Amos Chan, Rahul M Nandkishore, Michael Pretko, and Graeme Smith. Unitary-projective entanglement dynamics. *Physical Review B*, 99(22):224307, 2019.
- [22] Daniel Gottesman. Class of quantum error-correcting codes saturating the quantum hamming bound. *Phys. Rev. A*, 54:1862–1868, Sep 1996.
- [23] Daniel Gottesman. The heisenberg representation of quantum computers, 1998.
- [24] Scott Aaronson and Daniel Gottesman. Improved simulation of stabilizer circuits. *Phys. Rev. A*, 70:052328, Nov 2004.
- [25] Yaodong Li, Xiao Chen, and Matthew PA Fisher. Measurement-driven entanglement transition in hybrid quantum circuits. *Physical Review B*, 100(13):134306, 2019.
- [26] Yaodong Li, Sagar Vijay, and Matthew Fisher. Entanglement domain walls in monitored quantum circuits and the directed polymer in a random environment. *arXiv preprint arXiv:2105.13352*, 2021.
- [27] Yaodong Li, Xiao Chen, Andreas W. W. Ludwig, and Matthew P. A. Fisher. Conformal invariance and quantum nonlocality in critical hybrid circuits. *Phys. Rev. B*, 104:104305, Sep 2021.
- [28] Aidan Zabalo, Michael J Gullans, Justin H Wilson, Romain Vasseur, Andreas WW Ludwig, Sarang Gopalakrishnan, David A Huse, and JH Pixley. Operator scaling dimensions and multifractality at measurement-induced transitions. *Physical review letters*, 128(5):050602, 2022.
- [29] Michael J Gullans and David A Huse. Dynamical purification phase transition induced by quantum measurements. *Physical Review X*, 10(4):041020, 2020.
- [30] Yaodong Li and Matthew PA Fisher. Statistical mechanics of quantum error correcting codes. *Physical Review B*, 103(10):104306, 2021.
- [31] Yimu Bao, Soonwon Choi, and Ehud Altman. Theory of the phase transition in random unitary circuits with measurements. *Physical Review B*, 101(10):104301, 2020.

- [32] Xie Chen, Zheng-Cheng Gu, and Xiao-Gang Wen. Local unitary transformation, long-range quantum entanglement, wave function renormalization, and topological order. *Physical review b*, 82(15):155138, 2010.
- [33] Andrea Coser and David Pérez-García. Classification of phases for mixed states via fast dissipative evolution. *Quantum*, 3:174, 2019.
- [34] Matthew B Hastings. Topological order at nonzero temperature. *Physical review letters*, 107(21):210501, 2011.
- [35] Ruochen Ma and Chong Wang. Average symmetry-protected topological phases. *Physical Review X*, 13(3):031016, 2023.
- [36] Elliott H. Lieb and Derek W. Robinson. The finite group velocity of quantum spin systems. *Communications in Mathematical Physics*, 28(3):251–257, 1972.
- [37] S. Bravyi, M. B. Hastings, and F. Verstraete. Lieb-robinson bounds and the generation of correlations and topological quantum order. *Phys. Rev. Lett.*, 97:050401, Jul 2006.
- [38] John Cardy. Linking numbers for self-avoiding loops and percolation: Application to the spin quantum hall transition. *Phys. Rev. Lett.*, 84:3507–3510, Apr 2000.
- [39] Brian Skinner, Jonathan Ruhman, and Adam Nahum. Measurement-induced phase transitions in the dynamics of entanglement. *Phys. Rev. X*, 9:031009, Jul 2019.
- [40] Yaodong Li, Xiao Chen, and Matthew P. A. Fisher. Measurement-driven entanglement transition in hybrid quantum circuits. *Phys. Rev. B*, 100:134306, Oct 2019.
- [41] Adam Nahum, P. Serna, A. M. Somoza, and M. Ortuño. Loop models with crossings. *Phys. Rev. B*, 87:184204, May 2013.
- [42] J. L. Jacobsen, N. Read, and H. Saleur. Dense loops, supersymmetry, and goldstone phases in two dimensions. *Phys. Rev. Lett.*, 90:090601, Mar 2003.
- [43] N. Read and H. Saleur. Exact spectra of conformal supersymmetric nonlinear sigma models in two dimensions. *Nuclear Physics B*, 613(3):409 – 444, 2001.
- [44] A. L. Owczarek and T. Prellberg. The collapse point of interacting trails in two dimensions from kinetic growth simulations. *Journal of Statistical Physics*, 79(5):951–967, 1995.

- [45] Robert M. Ziff, X. P. Kong, and E. G. D. Cohen. Lorentz lattice-gas and kinetic-walk model. *Phys. Rev. A*, 44:2410–2428, Aug 1991.
- [46] M. J. Martins, B. Nienhuis, and R. Rietman. Intersecting loop model as a solvable super spin chain. *Phys. Rev. Lett.*, 81:504–507, Jul 1998.
- [47] Wouter Kager and Bernard Nienhuis. Monte carlo study of the hull distribution for the $q=1$ brauer model. *Journal of Statistical Mechanics: Theory and Experiment*, 2006(08):P08004–P08004, aug 2006.
- [48] Yacine Ikhlef, Jesper Jacobsen, and Hubert Saleur. Non-intersection exponents of fully packed trails on the square lattice. *Journal of Statistical Mechanics: Theory and Experiment*, 2007(05):P05005–P05005, may 2007.
- [49] Romain Vasseur, Andrew C. Potter, Yi-Zhuang You, and Andreas W. W. Ludwig. Entanglement transitions from holographic random tensor networks. *Phys. Rev. B*, 100:134203, Oct 2019.
- [50] Yaodong Li, Xiao Chen, and Matthew P. A. Fisher. Quantum zeno effect and the many-body entanglement transition. *Phys. Rev. B*, 98:205136, Nov 2018.
- [51] Alexei Kitaev. Anyons in an exactly solved model and beyond. *Annals of Physics*, 321(1):2 – 111, 2006. January Special Issue.
- [52] Beni Yoshida. Decoding the entanglement structure of monitored quantum circuits. *arXiv preprint arXiv:2109.08691*, 2021.
- [53] Adam Nahum, Jonathan Ruhman, Sagar Vijay, and Jeongwan Haah. Quantum entanglement growth under random unitary dynamics. *Physical Review X*, 7(3):031016, 2017.
- [54] Patrick Hayden, Matthew Headrick, and Alexander Maloney. Holographic mutual information is monogamous. *Physical Review D*, 87(4):046003, 2013.
- [55] Alexei Kitaev and John Preskill. Topological entanglement entropy. *Physical review letters*, 96(11):110404, 2006.
- [56] Patrick Hayden and John Preskill. Black holes as mirrors: quantum information in random subsystems. *Journal of high energy physics*, 2007(09):120, 2007.
- [57] Pavan Hosur, Xiao-Liang Qi, Daniel A Roberts, and Beni Yoshida. Chaos in quantum channels. *Journal of High Energy Physics*, 2016(2):1–49, 2016.

- [58] Matteo Ippoliti, Michael J Gullans, Sarang Gopalakrishnan, David A Huse, and Vedika Khemani. Entanglement phase transitions in measurement-only dynamics. *Physical Review X*, 11(1):011030, 2021.
- [59] Chao-Ming Jian, Yi-Zhuang You, Romain Vasseur, and Andreas WW Ludwig. Measurement-induced criticality in random quantum circuits. *Physical Review B*, 101(10):104302, 2020.
- [60] Tianci Zhou and Adam Nahum. Emergent statistical mechanics of entanglement in random unitary circuits. *Physical Review B*, 99(17):174205, 2019.
- [61] Cheryne Jonay, David A Huse, and Adam Nahum. Coarse-grained dynamics of operator and state entanglement. *arXiv preprint arXiv:1803.00089*, 2018.
- [62] David A Huse and Christopher L Henley. Pinning and roughening of domain walls in ising systems due to random impurities. *Physical review letters*, 54(25):2708, 1985.
- [63] Ahmed Almheiri. Holographic quantum error correction and the projected black hole interior. *arXiv preprint arXiv:1810.02055*, 2018.
- [64] Tadashi Takayanagi. Holographic dual of a boundary conformal field theory. *Physical review letters*, 107(10):101602, 2011.
- [65] Beni Yoshida. Projective measurement of black holes. *arXiv preprint arXiv:2203.04968*, 2022.
- [66] M A Rajabpour. Entanglement entropy after a partial projective measurement in 1+1 dimensional conformal field theories: exact results. *Journal of Statistical Mechanics: Theory and Experiment*, 2016(6):063109, jun 2016.
- [67] Cheng-Ju Lin, Weicheng Ye, Yijian Zou, Shengqi Sang, and Timothy H. Hsieh. Probing sign structure using measurement-induced entanglement, 2022.
- [68] Samuel J. Garratt, Zack Weinstein, and Ehud Altman. Measurements conspire non-locally to restructure critical quantum states, 2022.
- [69] Shengqi Sang, Yaodong Li, Tianci Zhou, Xiao Chen, Timothy H Hsieh, and Matthew PA Fisher. Entanglement negativity at measurement-induced criticality. *PRX Quantum*, 2(3):030313, 2021.
- [70] Stefano Antonini, Gregory Bentsen, ChunJun Cao, Jonathan Harper, Shao-Kai Jian, and Brian Swingle. Holographic measurement and bulk teleportation, 2022.

- [71] Stefano Antonini, Brianna Grado-White, Shao-Kai Jian, and Brian Swingle. Holographic measurement and quantum teleportation in the syk thermofield double, 2022.
- [72] Kenneth G. Wilson. The renormalization group: Critical phenomena and the kondo problem. *Rev. Mod. Phys.*, 47:773–840, Oct 1975.
- [73] Leo P. Kadanoff. Scaling laws for ising models near T_c . *Physics Physique Fizika*, 2:263–272, Jun 1966.
- [74] Steven R White. Density matrix formulation for quantum renormalization groups. *Physical review letters*, 69(19):2863, 1992.
- [75] Guifre Vidal. Entanglement renormalization. *Physical review letters*, 99(22):220405, 2007.
- [76] M. Fannes, B. Nachtergaele, and R. F. Werner. Finitely correlated states on quantum spin chains. *Communications in Mathematical Physics*, 144(3):443–490, March 1992.
- [77] F. Verstraete and J. I. Cirac. Renormalization algorithms for quantum-many body systems in two and higher dimensions, 2004.
- [78] Matthew B Hastings and Xiao-Gang Wen. Quasiadiabatic continuation of quantum states: The stability of topological ground-state degeneracy and emergent gauge invariance. *Physical review b*, 72(4):045141, 2005.
- [79] Itai Arad, Alexei Kitaev, Zeph Landau, and Umesh Vazirani. An area law and sub-exponential algorithm for 1d systems. *arXiv preprint arXiv:1301.1162*, 2013.
- [80] Dénes Petz. Sufficiency of channels over von neumann algebras. *The Quarterly Journal of Mathematics*, 39(1):97–108, 1988.
- [81] Omar Fawzi and Renato Renner. Quantum conditional mutual information and approximate markov chains. *Communications in Mathematical Physics*, 340(2):575–611, 2015.
- [82] Anurag Anshu, Debbie Leung, and Dave Touchette. Incompressibility of classical distributions. *IEEE Transactions on Information Theory*, 68(3):1758–1771, 2021.
- [83] Zahra Baghali Khanian and Andreas Winter. General mixed-state quantum data compression with and without entanglement assistance. *IEEE Transactions on Information Theory*, 68(5):3130–3138, 2022.

- [84] Zahra Baghali Khanian. Strong converse bounds for compression of mixed states. *arXiv preprint arXiv:2206.09415*, 2022.
- [85] Kohtaro Kato. Exact and local compression of quantum bipartite states. *arXiv preprint arXiv:2309.07434*, 2023.
- [86] Eric Dennis, Alexei Kitaev, Andrew Landahl, and John Preskill. Topological quantum memory. *Journal of Mathematical Physics*, 43(9):4452–4505, 2002.
- [87] Miguel Aguado and Guifre Vidal. Entanglement renormalization and topological order. *Physical review letters*, 100(7):070404, 2008.
- [88] James William Harrington. *Analysis of quantum error-correcting codes: symplectic lattice codes and toric codes*. California Institute of Technology, 2004.
- [89] Guillaume Duclos-Cianci and David Poulin. Fast decoders for topological quantum codes. *Physical review letters*, 104(5):050504, 2010.
- [90] Sergey Bravyi and Jeongwan Haah. Quantum self-correction in the 3d cubic code model. *Phys. Rev. Lett.*, 111:200501, Nov 2013.
- [91] Nikolas P Breuckmann, Kasper Duivenvoorden, Dominik Michels, and Barbara M Terhal. Local decoders for the 2d and 4d toric code. *arXiv preprint arXiv:1609.00510*, 2016.
- [92] Sergey Bravyi, Martin Suchara, and Alexander Vargo. Efficient algorithms for maximum likelihood decoding in the surface code. *Physical Review A*, 90(3):032326, 2014.
- [93] Chenyang Wang, Jim Harrington, and John Preskill. Confinement-higgs transition in a disordered gauge theory and the accuracy threshold for quantum memory. *Annals of Physics*, 303(1):31–58, 2003.
- [94] Zijian Wang, Zhengzhi Wu, and Zhong Wang. Intrinsic mixed-state topological order without quantum memory. *arXiv preprint arXiv:2307.13758*, 2023.
- [95] Yijian Zou, Shengqi Sang, and Timothy H. Hsieh. Channeling quantum criticality. *Physical Review Letters*, 130(25):250403, 2023.
- [96] Jong Yeon Lee, Chao-Ming Jian, and Cenke Xu. Quantum criticality under decoherence or weak measurement. *arXiv preprint arXiv:2301.05238*, 2023.

- [97] Tsung-Cheng Lu, Timothy H. Hsieh, and Tarun Grover. Detecting topological order at finite temperature using entanglement negativity. *Phys. Rev. Lett.*, 125:116801, Sep 2020.
- [98] Ruihua Fan, Yimu Bao, Ehud Altman, and Ashvin Vishwanath. Diagnostics of mixed-state topological order and breakdown of quantum memory. *arXiv preprint arXiv:2301.05689*, 2023.
- [99] Yu-Hsueh Chen and Tarun Grover. Separability transitions in topological states induced by local decoherence, 2023.
- [100] Alexei Kitaev and John Preskill. Topological entanglement entropy. *Phys. Rev. Lett.*, 96:110404, Mar 2006.
- [101] Michael Levin and Xiao-Gang Wen. Detecting topological order in a ground state wave function. *Phys. Rev. Lett.*, 96:110405, Mar 2006.
- [102] Bowen Shi, Kohtaro Kato, and Isaac H. Kim. Fusion rules from entanglement. *Annals of Physics*, 418:168164, 2020.
- [103] Yifan Zhang and Sarang Gopalakrishnan. Nonlocal growth of quantum conditional mutual information under decoherence, 2024.
- [104] Su un Lee, Changhun Oh, Yat Wong, Senrui Chen, and Liang Jiang. Universal spreading of conditional mutual information in noisy random circuits, 2024.
- [105] Emilio Onorati, Cambyse Rouzé, Daniel Stilck França, and James D Watson. Efficient learning of ground & thermal states within phases of matter. *arXiv preprint arXiv:2301.12946*, 2023.
- [106] Fernando GSL Brandao and Michael J Kastoryano. Finite correlation length implies efficient preparation of quantum thermal states. *Communications in Mathematical Physics*, 365:1–16, 2019.
- [107] Paul Gondolf, Samuel O Scalet, Alberto Ruiz-de Alarcon, Alvaro M Alhambra, and Angela Capel. Conditional independence of 1d gibbs states with applications to efficient learning. *arXiv preprint arXiv:2402.18500*, 2024.
- [108] Marius Junge, Renato Renner, David Sutter, Mark M Wilde, and Andreas Winter. Universal recovery maps and approximate sufficiency of quantum relative entropy. In *Annales Henri Poincaré*, volume 19, pages 2955–2978. Springer, 2018.

- [109] Hyukjoon Kwon, Rick Mukherjee, and MS Kim. Reversing lindblad dynamics via continuous petz recovery map. *Physical Review Letters*, 128(2):020403, 2022.
- [110] V. Murg, F. Verstraete, and J. I. Cirac. Variational study of hard-core bosons in a two-dimensional optical lattice using projected entangled pair states. *Phys. Rev. A*, 75:033605, Mar 2007.
- [111] Sergey Bravyi, Martin Suchara, and Alexander Vargo. Efficient algorithms for maximum likelihood decoding in the surface code. *Phys. Rev. A*, 90:032326, Sep 2014.
- [112] Jong Yeon Lee. Exact calculations of coherent information for toric codes under decoherence: Identifying the fundamental error threshold, 2024.
- [113] Yukiyasu Ozeki and Hidetoshi Nishimori. Phase diagram of gauge glasses. *Journal of Physics A: Mathematical and General*, 26(14):3399, 1993.
- [114] F Merz and JT Chalker. Two-dimensional random-bond ising model, free fermions, and the network model. *Physical Review B*, 65(5):054425, 2002.
- [115] Caroline de Groot, Alex Turzillo, and Norbert Schuch. Symmetry protected topological order in open quantum systems. *Quantum*, 6:856, 2022.
- [116] Jian-Hao Zhang, Yang Qi, and Zhen Bi. Strange correlation function for average symmetry-protected topological phases, 2022.
- [117] Jong Yeon Lee, Yi-Zhuang You, and Cenke Xu. Symmetry protected topological phases under decoherence. *arXiv preprint arXiv:2210.16323*, 2022.
- [118] Hanyu Xue, Jong Yeon Lee, and Yimu Bao. Tensor network formulation of symmetry protected topological phases in mixed states. *arXiv preprint arXiv:2403.17069*, 2024.
- [119] Yuchen Guo, Jian-Hao Zhang, Shuo Yang, and Zhen Bi. Locally purified density operators for symmetry-protected topological phases in mixed states. *arXiv preprint arXiv:2403.16978*, 2024.
- [120] Ruochen Ma and Alex Turzillo. Symmetry protected topological phases of mixed states in the doubled space. *arXiv preprint arXiv:2403.13280*, 2024.
- [121] Matthew S Leifer and David Poulin. Quantum graphical models and belief propagation. *Annals of Physics*, 323(8):1899–1946, 2008.

- [122] Tomotaka Kuwahara, Kohtaro Kato, and Fernando G. S. L. Brandão. Clustering of conditional mutual information for quantum gibbs states above a threshold temperature. *Phys. Rev. Lett.*, 124:220601, Jun 2020.
- [123] Kohtaro Kato and Fernando GSL Brandao. Quantum approximate markov chains are thermal. *Communications in Mathematical Physics*, 370:117–149, 2019.
- [124] Xiangyu Cao, Antoine Tilloy, and Andrea De Luca. Entanglement in a fermion chain under continuous monitoring. *SciPost Phys.*, 7:24, 2019.
- [125] Amos Chan, Rahul M. Nandkishore, Michael Pretko, and Graeme Smith. Unitary-projective entanglement dynamics. *Phys. Rev. B*, 99:224307, Jun 2019.
- [126] Soonwon Choi, Yimu Bao, Xiao-Liang Qi, and Ehud Altman. Quantum error correction in scrambling dynamics and measurement induced phase transition, 2019.
- [127] M. Szyniszewski, A. Romito, and H. Schomerus. Entanglement transition from variable-strength weak measurements. *Phys. Rev. B*, 100:064204, Aug 2019.
- [128] Michael J. Gullans and David A. Huse. Dynamical purification phase transition induced by quantum measurements, 2019.
- [129] Yimu Bao, Soonwon Choi, and Ehud Altman. Theory of the phase transition in random unitary circuits with measurements. *Phys. Rev. B*, 101:104301, Mar 2020.
- [130] Chao-Ming Jian, Yi-Zhuang You, Romain Vasseur, and Andreas W. W. Ludwig. Measurement-induced criticality in random quantum circuits. *Phys. Rev. B*, 101:104302, Mar 2020.
- [131] Qicheng Tang and W. Zhu. Measurement-induced phase transition: A case study in the nonintegrable model by density-matrix renormalization group calculations. *Phys. Rev. Research*, 2:013022, Jan 2020.
- [132] Michael J. Gullans and David A. Huse. Scalable probes of measurement-induced criticality, 2019.
- [133] Aidan Zabalo, Michael J. Gullans, Justin H. Wilson, Sarang Gopalakrishnan, David A. Huse, and J. H. Pixley. Critical properties of the measurement-induced transition in random quantum circuits. *Phys. Rev. B*, 101:060301, Feb 2020.

- [134] Lei Zhang, Justin A. Reyes, Stefanos Kourtis, Claudio Chamon, Eduardo R. Mucciolo, and Andrei E. Ruckenstein. Nonuniversal entanglement level statistics in projection-driven quantum circuits, 2020.
- [135] Ruihua Fan, Sagar Vijay, Ashvin Vishwanath, and Yi-Zhuang You. Self-organized error correction in random unitary circuits with measurement, 2020.
- [136] Oles Shtanko, Yaroslav A. Kharkov, Luis Pedro García-Pintos, and Alexey V. Gorshkov. Classical models of entanglement in monitored random circuits, 2020.
- [137] Yaodong Li, Xiao Chen, Andreas W. W. Ludwig, and Matthew P. A. Fisher. Conformal invariance and quantum non-locality in hybrid quantum circuits, 2020.
- [138] Rahul Nandkishore and David A. Huse. Many-body localization and thermalization in quantum statistical mechanics. *Annual Review of Condensed Matter Physics*, 6(1):15–38, 2015.
- [139] Dmitry A. Abanin, Ehud Altman, Immanuel Bloch, and Maksym Serbyn. Colloquium: Many-body localization, thermalization, and entanglement. *Rev. Mod. Phys.*, 91:021001, May 2019.
- [140] David A. Huse, Rahul Nandkishore, Vadim Oganesyan, Arijeet Pal, and S. L. Sondhi. Localization-protected quantum order. *Phys. Rev. B*, 88:014206, Jul 2013.
- [141] Jonas A. Kjäll, Jens H. Bardarson, and Frank Pollmann. Many-body localization in a disordered quantum ising chain. *Phys. Rev. Lett.*, 113:107204, Sep 2014.
- [142] Yasaman Bahri, Ronen Vosk, Ehud Altman, and Ashvin Vishwanath. Localization and topology protected quantum coherence at the edge of hot matter. *Nature Communications*, 6(1):7341, 2015.
- [143] Matthew P. A. Fisher and Leo Radzihovsky. Quantum indistinguishability in chemical reactions. *Proceedings of the National Academy of Sciences*, 115(20):E4551–E4558, 2018.
- [144] Matthew P.A. Fisher. Quantum cognition: The possibility of processing with nuclear spins in the brain. *Annals of Physics*, 362:593 – 602, 2015.
- [145] Nicole [Yunger Halpern] and Elizabeth Crosson. Quantum information in the posner model of quantum cognition. *Annals of Physics*, 407:92 – 147, 2019.

- [146] Dorit Aharonov. Quantum to classical phase transition in noisy quantum computers. *Phys. Rev. A*, 62:062311, Nov 2000.
- [147] D. Stauffer and A. Aharony. *Introduction To Percolation Theory*. London: Taylor and Francis, 1992.
- [148] Ali Lavasani, Yahya Alavirad, and Maissam Barkeshli. Measurement-induced topological entanglement transitions in symmetric random quantum circuits, 2020.
- [149] Stephen H Shenker and Douglas Stanford. Black holes and the butterfly effect. *Journal of High Energy Physics*, 2014(3):1–25, 2014.
- [150] Daniel A Roberts, Douglas Stanford, and Leonard Susskind. Localized shocks. *Journal of High Energy Physics*, 2015(3):1–27, 2015.
- [151] Yasuhiro Sekino and Leonard Susskind. Fast scramblers. *Journal of High Energy Physics*, 2008(10):065, 2008.
- [152] Pasquale Calabrese and John Cardy. Evolution of entanglement entropy in one-dimensional systems. *Journal of Statistical Mechanics: Theory and Experiment*, 2005(04):P04010, 2005.
- [153] Elliott H Lieb and Derek W Robinson. The finite group velocity of quantum spin systems. In *Statistical mechanics*, pages 425–431. Springer, 1972.
- [154] CW Von Keyserlingk, Tibor Rakovszky, Frank Pollmann, and Shivaji Lal Sondhi. Operator hydrodynamics, otocs, and entanglement growth in systems without conservation laws. *Physical Review X*, 8(2):021013, 2018.
- [155] Adam Nahum, Sagar Vijay, and Jeongwan Haah. Operator spreading in random unitary circuits. *Phys. Rev. X*, 8:021014, Apr 2018.
- [156] Aaron J Friedman, Chao Yin, Yifan Hong, and Andrew Lucas. Locality and error correction in quantum dynamics with measurement. *arXiv preprint arXiv:2206.09929*, 2022.
- [157] Yimu Bao, Maxwell Block, and Ehud Altman. Finite time teleportation phase transition in random quantum circuits. *arXiv preprint arXiv:2110.06963*, 2021.
- [158] Lorenzo Piroli, Georgios Styliaris, and J. Ignacio Cirac. Quantum circuits assisted by local operations and classical communication: Transformations and phases of matter. *Phys. Rev. Lett.*, 127:220503, Nov 2021.

- [159] Nathanan Tantivasadakarn, Ashvin Vishwanath, and Ruben Verresen. A hierarchy of topological order from finite-depth unitaries, measurement and feedforward, 2022.
- [160] Sergey Bravyi, Isaac Kim, Alexander Kliesch, and Robert Koenig. Adaptive constant-depth circuits for manipulating non-abelian anyons, 2022.
- [161] Tsung-Cheng Lu, Leonardo A Lessa, Isaac H Kim, and Timothy H Hsieh. Measurement as a shortcut to long-range entangled quantum matter. *arXiv preprint arXiv:2206.13527*, 2022.
- [162] Jong Yeon Lee, Wenjie Ji, Zhen Bi, and Matthew Fisher. Measurement-prepared quantum criticality: from ising model to gauge theory, and beyond. *arXiv preprint arXiv:2208.11699*, 2022.
- [163] Nathanan Tantivasadakarn, Ashvin Vishwanath, and Ruben Verresen. A hierarchy of topological order from finite-depth unitaries, measurement and feedforward. *arXiv preprint arXiv:2209.06202*, 2022.
- [164] Guo-Yi Zhu, Nathanan Tantivasadakarn, Ashvin Vishwanath, Simon Trebst, and Ruben Verresen. Nishimori’s cat: stable long-range entanglement from finite-depth unitaries and weak measurements. *arXiv preprint arXiv:2208.11136*, 2022.
- [165] Michael J Gullans and David A Huse. Scalable probes of measurement-induced criticality. *Physical review letters*, 125(7):070606, 2020.
- [166] Aidan Zabalo, Michael J Gullans, Justin H Wilson, Sarang Gopalakrishnan, David A Huse, and JH Pixley. Critical properties of the measurement-induced transition in random quantum circuits. *Physical Review B*, 101(6):060301, 2020.
- [167] Romain Vasseur, Andrew C Potter, Yi-Zhuang You, and Andreas WW Ludwig. Entanglement transitions from holographic random tensor networks. *Physical Review B*, 100(13):134203, 2019.
- [168] Soonwon Choi, Yimu Bao, Xiao-Liang Qi, and Ehud Altman. Quantum error correction in scrambling dynamics and measurement-induced phase transition. *Phys. Rev. Lett.*, 125:030505, Jul 2020.
- [169] Scott Aaronson and Daniel Gottesman. Improved simulation of stabilizer circuits. *Physical Review A*, 70(5):052328, 2004.
- [170] Mehran Kardar and Yi-Cheng Zhang. Scaling of directed polymers in random media. *Phys. Rev. Lett.*, 58:2087–2090, May 1987.

- [171] Daniel Gottesman. *Stabilizer codes and quantum error correction*. California Institute of Technology, 1997.
- [172] Lukasz Fidkowski, Jeongwan Haah, and Matthew B Hastings. How dynamical quantum memories forget. *Quantum*, 5:382, 2021.
- [173] Iris Cong, Nishad Maskara, Minh C Tran, Hannes Pichler, Giulia Semeghini, Susanne F Yelin, Soonwon Choi, and Mikhail D Lukin. Enhancing detection of topological order by local error correction. *arXiv preprint arXiv:2209.12428*, 2022.
- [174] Iris Cong, Soonwon Choi, and Mikhail D Lukin. Quantum convolutional neural networks. *Nature Physics*, 15(12):1273–1278, 2019.
- [175] G. Semeghini, H. Levine, A. Keesling, S. Ebadi, T. T. Wang, D. Bluvstein, R. Verresen, H. Pichler, M. Kalinowski, R. Samajdar, A. Omran, S. Sachdev, A. Vishwanath, M. Greiner, V. Vuletić, and M. D. Lukin. Probing topological spin liquids on a programmable quantum simulator. *Science*, 374(6572):1242–1247, 2021.
- [176] K. J. Satzinger, Y.-J Liu, A. Smith, C. Knapp, M. Newman, C. Jones, Z. Chen, C. Quintana, X. Mi, A. Dunsworth, C. Gidney, I. Aleiner, F. Arute, K. Arya, J. Atalaya, R. Babbush, J. C. Bardin, R. Barends, J. Basso, A. Bengtsson, A. Bिल्mes, M. Broughton, B. B. Buckley, D. A. Buell, B. Burkett, N. Bushnell, B. Chiaro, R. Collins, W. Courtney, S. Demura, A. R. Derk, D. Eppens, C. Erickson, L. Faoro, E. Farhi, A. G. Fowler, B. Foxen, M. Giustina, A. Greene, J. A. Gross, M. P. Harrigan, S. D. Harrington, J. Hilton, S. Hong, T. Huang, W. J. Huggins, L. B. Ioffe, S. V. Isakov, E. Jeffrey, Z. Jiang, D. Kafri, K. Kechedzhi, T. Khattar, S. Kim, P. V. Klimov, A. N. Korotkov, F. Kostritsa, D. Landhuis, P. Laptev, A. Locharla, E. Lucero, O. Martin, J. R. McClean, M. McEwen, K. C. Miao, M. Mohseni, S. Montazeri, W. Mruczkiewicz, J. Mutus, O. Naaman, M. Neeley, C. Neill, M. Y. Niu, T. E. O’Brien, A. Opremcak, B. Pató, A. Petukhov, N. C. Rubin, D. Sank, V. Shvarts, D. Strain, M. Szalay, B. Villalonga, T. C. White, Z. Yao, P. Yeh, J. Yoo, A. Zalcman, H. Neven, S. Boixo, A. Megrant, Y. Chen, J. Kelly, V. Smelyanskiy, A. Kitaev, M. Knap, F. Pollmann, and P. Roushan. Realizing topologically ordered states on a quantum processor. *Science*, 374(6572):1237–1241, 2021.
- [177] Guo-Yi Zhu, Nathanan Tantivasadakarn, Ashvin Vishwanath, Simon Trebst, and Ruben Verresen. Nishimori’s cat: stable long-range entanglement from finite-depth unitaries and weak measurements, 2022.

- [178] Jong Yeon Lee, Wenjie Ji, Zhen Bi, and Matthew P. A. Fisher. Decoding measurement-prepared quantum phases and transitions: from ising model to gauge theory, and beyond, 2022.
- [179] Frank Verstraete, Michael M. Wolf, and J. Ignacio Cirac. Quantum computation and quantum-state engineering driven by dissipation. *Nature Physics*, 5(9):633–636, 2009.
- [180] S. Diehl, A. Micheli, A. Kantian, B. Kraus, H. P. Büchler, and P. Zoller. Quantum states and phases in driven open quantum systems with cold atoms. *Nature Physics*, 4(11):878–883, 2008.
- [181] Cheng-Ju Lin, Zhi Li, and Timothy H Hsieh. Entanglement renormalization of thermofield double states. *Physical Review Letters*, 127(8):080602, 2021.
- [182] Brian Swingle and John McGreevy. Mixed s-sourcery: Building many-body states using bubbles of nothing. *Physical Review B*, 94(15):155125, 2016.
- [183] Frank Verstraete, J Ignacio Cirac, José Ignacio Latorre, E Rico, and Michael M Wolf. Renormalization-group transformations on quantum states. *Physical review letters*, 94(14):140601, 2005.
- [184] Tsung-Cheng Lu, Zhehao Zhang, Sagar Vijay, and Timothy H. Hsieh. Mixed-state long-range order and criticality from measurement and feedback. *arXiv preprint arXiv:2303.15507*, 2023.
- [185] Yimu Bao, Ruihua Fan, Ashvin Vishwanath, and Ehud Altman. Mixed-state topological order and the errorfield double formulation of decoherence-induced transitions. *arXiv preprint arXiv:2301.05687*, 2023.
- [186] Ruochen Ma. Exploring critical systems under measurements and decoherence via keldysh field theory. *arXiv preprint arXiv:2304.08277*, 2023.
- [187] Ruochen Ma, Jian-Hao Zhang, Zhen Bi, Meng Cheng, and Chong Wang. Topological phases with average symmetries: the decohered, the disordered, and the intrinsic. *arXiv preprint arXiv:2305.16399*, 2023.
- [188] Patrick Hayden, Richard Jozsa, Denes Petz, and Andreas Winter. Structure of states which satisfy strong subadditivity of quantum entropy with equality. *Communications in mathematical physics*, 246:359–374, 2004.

- [189] Masato Koashi and Nobuyuki Imoto. Operations that do not disturb partially known quantum states. *Physical Review A*, 66(2):022318, 2002.
- [190] Barbara M Terhal and Paweł Horodecki. Schmidt number for density matrices. *Physical Review A*, 61(4):040301, 2000.
- [191] Chi-Fang Chen, Kohtaro Kato, and Fernando GSL Brandão. Matrix product density operators: When do they have a local parent hamiltonian? *arXiv preprint arXiv:2010.14682*, 2020.
- [192] Benjamin Schumacher and Michael A Nielsen. Quantum data processing and error correction. *Physical Review A*, 54(4):2629, 1996.
- [193] Matthew B Hastings. An area law for one-dimensional quantum systems. *Journal of statistical mechanics: theory and experiment*, 2007(08):P08024, 2007.
- [194] Sergey Bravyi and Robert König. Classification of topologically protected gates for local stabilizer codes. *Physical review letters*, 110(17):170503, 2013.
- [195] Ethan Lake, Shankar Balasubramanian, and Soonwon Choi. Exact quantum algorithms for quantum phase recognition: Renormalization group and error correction. *arXiv preprint arXiv:2211.09803*, 2022.
- [196] Frank Verstraete, Juan J Garcia-Ripoll, and Juan Ignacio Cirac. Matrix product density operators: Simulation of finite-temperature and dissipative systems. *Physical review letters*, 93(20):207204, 2004.
- [197] Alberto Ruiz de Alarcón, José Garre-Rubio, András Molnár, and David Pérez-García. Matrix product operator algebras ii: phases of matter for 1d mixed states. *arXiv preprint arXiv:2204.06295*, 2022.
- [198] J Ignacio Cirac, David Perez-Garcia, Norbert Schuch, and Frank Verstraete. Matrix product density operators: Renormalization fixed points and boundary theories. *Annals of Physics*, 378:100–149, 2017.
- [199] Gemma De las Cuevas, Norbert Schuch, David Pérez-García, and J Ignacio Cirac. Purifications of multipartite states: limitations and constructive methods. *New Journal of Physics*, 15(12):123021, 2013.
- [200] Martin Kliesch, David Gross, and Jens Eisert. Matrix-product operators and states: Np-hardness and undecidability. *Physical review letters*, 113(16):160503, 2014.

- [201] X. G. Wen. Topological Order in Rigid States. *Int. J. Mod. Phys. B*, 4:239, 1990.
- [202] Michael H. Freedman, Alexei Kitaev, Michael J. Larsen, and Zhenghan Wang. Topological quantum computation, 2002.
- [203] Michael Levin and Xiao-Gang Wen. Detecting topological order in a ground state wave function. *Physical Review Letters*, 96(11), mar 2006.
- [204] Alexei Kitaev and John Preskill. Topological entanglement entropy. *Physical Review Letters*, 96(11), mar 2006.
- [205] Michael A. Levin and Xiao-Gang Wen. String-net condensation: a physical mechanism for topological phases. *Physical Review B*, 71(4), jan 2005.
- [206] Pasquale Calabrese and John Cardy. Entanglement entropy and quantum field theory. *Journal of Statistical Mechanics: Theory and Experiment*, 2004(06):P06002, jun 2004.
- [207] Xie Chen, Zheng-Cheng Gu, and Xiao-Gang Wen. Classification of gapped symmetric phases in one-dimensional spin systems. *Physical Review B*, 83(3), jan 2011.
- [208] Y.-Y. Shi, L.-M. Duan, and G. Vidal. Classical simulation of quantum many-body systems with a tree tensor network. *Physical Review A*, 74(2), aug 2006.
- [209] Fernando Pastawski, Beni Yoshida, Daniel Harlow, and John Preskill. Holographic quantum error-correcting codes: toy models for the bulk/boundary correspondence. *Journal of High Energy Physics*, 2015(6), jun 2015.
- [210] Patrick Hayden, Sepehr Nezami, Xiao-Liang Qi, Nathaniel Thomas, Michael Walter, and Zhao Yang. Holographic duality from random tensor networks. *Journal of High Energy Physics*, 2016(11), nov 2016.
- [211] Tibor Rakovszky, Sarang Gopalakrishnan, and Curt von Keyserlingk. Defining stable phases of open quantum systems, 2023.
- [212] Daniel Malz, Georgios Styliaris, Zhi-Yuan Wei, and J Ignacio Cirac. Preparation of matrix product states with log-depth quantum circuits. *arXiv preprint arXiv:2307.01696*, 2023.
- [213] Matthew B Hastings and Tohru Koma. Spectral gap and exponential decay of correlations. *Communications in mathematical physics*, 265:781–804, 2006.

- [214] Sergey Bravyi, Matthew B Hastings, and Spyridon Michalakis. Topological quantum order: stability under local perturbations. *Journal of mathematical physics*, 51(9), 2010.
- [215] Spyridon Michalakis and Justyna P Zwolak. Stability of frustration-free hamiltonians. *Communications in Mathematical Physics*, 322:277–302, 2013.
- [216] Zijian Wang and Linhao Li. Anomaly in open quantum systems and its implications on mixed-state quantum phases. *arXiv preprint arXiv:2403.14533*, 2024.
- [217] Zijian Wang, Xu-Dong Dai, He-Ran Wang, and Zhong Wang. Topologically ordered steady states in open quantum systems. *arXiv preprint arXiv:2306.12482*, 2023.
- [218] Tomotaka Kuwahara, Kohtaro Kato, and Fernando GSL Brandão. Clustering of conditional mutual information for quantum gibbs states above a threshold temperature. *Physical review letters*, 124(22):220601, 2020.
- [219] Sven Bachmann, Spyridon Michalakis, Bruno Nachtergaele, and Robert Sims. Automorphic equivalence within gapped phases of quantum lattice systems. *Communications in Mathematical Physics*, 309(3):835–871, 2012.
- [220] Ruochen Ma and Chong Wang. Average symmetry-protected topological phases. *Phys. Rev. X*, 13:031016, Aug 2023.
- [221] Zhuan Li and Roger S. K. Mong. Replica topological order in quantum mixed states and quantum error correction, 2024.
- [222] Leonardo A. Lessa, Meng Cheng, and Chong Wang. Mixed-state quantum anomaly and multipartite entanglement, 2024.
- [223] Yu-Hsueh Chen and Tarun Grover. Unconventional topological mixed-state transition and critical phase induced by self-dual coherent errors, 2024.
- [224] Ramanjit Sohal and Abhinav Prem. A noisy approach to intrinsically mixed-state topological order, 2024.
- [225] Tyler Ellison and Meng Cheng. Towards a classification of mixed state topological orders in two dimensions, in preparation.
- [226] Yu-Hsueh Chen and Tarun Grover. Symmetry-enforced many-body separability transitions, 2023.

- [227] Tibor Rakovszky, Sarang Gopalakrishnan, and Curt von Keyserlingk. Defining stable phases of open quantum systems, 2024.

APPENDICES

Appendix A

Appendix for Chapter.1

A.1 Relation between pure- and mixed- state phase equivalence

We sketch a proof of the following statement: On a given lattice, two pure states $|\psi_1\rangle$ and $|\psi_2\rangle$ are of the same mixed-state phase if and only if there exists an invertible state $|a\rangle$ on the same lattice such that $|\psi_1\rangle$ and $|\psi_2\rangle \otimes |a\rangle$ are of the same pure state phase. A many-body ground state $|a\rangle$ is called an invertible state if there exists another state $|\tilde{a}\rangle$ such that $|a\rangle \otimes |\tilde{a}\rangle$ can be LU transformed into a product state.

Since a LU transformation is also a LC transformation, pure-state phase equivalence trivially implies mixed-state phase equivalence.

Now we show the other direction. Assume that there exists a pair of LC transformations $\mathcal{C}_{1,2}$ such that $\mathcal{C}_1(\rho_1) \approx \rho_2$ and $\mathcal{C}_2(\rho_2) \approx \rho_1$. We use U_1, U_2 to denote the unitary circuit within the definition of \mathcal{C}_1 and \mathcal{C}_2 .

We observe that: Since $\mathcal{C}_1(\rho_1) \approx \rho_2$ and ρ_2 is a pure state, the state right before the tracing-out operation must factorize as:

$$U(|\psi_1\rangle \otimes |\mathbf{0}\rangle) \approx |\psi_2\rangle \otimes |a_1\rangle \tag{A.1}$$

where $|a_1\rangle$ is the state that supports on qubits to be traced out and is defined on the same lattice. Recalling the definition of pure-state phases, we conclude the (pure-state) phase equivalence: $|\psi_1\rangle \underset{\text{pure}}{\sim} |\psi_2\rangle \otimes |a_1\rangle$. Following a similar argument, we can also obtain

$|\psi_2\rangle \underset{pure}{\sim} |\psi_1\rangle \otimes |a_2\rangle$. We thus have:

$$|\psi_1\rangle \underset{pure}{\sim} |\psi_2\rangle \otimes |a_1\rangle \underset{pure}{\sim} |\psi_1\rangle \otimes |a_2\rangle \otimes |a_1\rangle \quad (\text{A.2})$$

As a result, the state $|a_1\rangle \otimes |a_2\rangle$ is in the trivial phase, and $|a_1\rangle$ is either in the trivial phase or an invertible state. Note that the proof assumes there is no ‘catalyst’ effect in phase equivalence relation: if $|\psi_1\rangle$ and $|\psi_2\rangle$ cannot be LU connected to each other, then neither does the pair $|\psi_1\rangle \otimes |a\rangle$ and $|\psi_2\rangle \otimes |a\rangle$, for any state $|a\rangle$.

Appendix B

Appendix for Chapter.2

Proposition Claim

B.1 Clifford Circuits with Symmetry

A stabilizer state over N qubits $|\psi_{\mathcal{S}}\rangle$ is defined to be the unique simultaneous $+1$ eigen-state of a set of stabilizers \mathcal{S} :

$$s |\psi_{\mathcal{S}}\rangle = |\psi_{\mathcal{S}}\rangle \quad \forall s \in \mathcal{S} \quad (\text{B.1})$$

Where $\mathcal{S} = \{s_1, \dots, s_N\}$ is a set of mutually commuting and independent (under multiplication) Pauli string operators. The algorithm for obtaining entanglement entropy from \mathcal{S} was introduced in [39]

Since any non-identity Pauli string operator $s \in \mathcal{S}$ has spectrum $\{1, -1\}$, $\frac{1}{2}(s + 1)$ is a projector to the s 's positive eigen-space. Further the density matrix of $|\psi_{\mathcal{S}}\rangle$ can be explicitly written as:

$$\rho_{\mathcal{S}} = |\psi_{\mathcal{S}}\rangle \langle \psi_{\mathcal{S}}| = \prod_i \left(\frac{1 + s_i}{2} \right) = \frac{1}{2^N} \sum_{g \in \mathcal{G}} g \quad (\text{B.2})$$

Here $\mathcal{G}_{\mathcal{S}} = \{s_1^{b_1}, \dots, s_N^{b_N} | b_i \in \{0, 1\} \forall i\}$ is the finite abelian group spanned by \mathcal{S} under multiplication, named the stabilizer group of $|\psi_{\mathcal{S}}\rangle$.

A stabilizer state $|\psi_{\mathcal{S}}\rangle$ can be efficiently stored in memory by only keeping track of \mathcal{S} , which takes $\mathcal{O}(N^2)$ bytes. One can also obtain quantities involving $|\psi_{\mathcal{S}}\rangle$ by only referring

to \mathcal{S} . A method for calculating bipartite entanglement entropy from \mathcal{S} was introduced in [40]. For the spin glass order parameter 2.2, the two-point correlation square term can be expressed as:

$$\begin{aligned}
& \langle \psi_{\mathcal{S}} | Z_i Z_j | \psi_{\mathcal{S}} \rangle^2 \\
&= \text{Tr}(\rho_{\mathcal{S}} Z_i Z_j \rho_{\mathcal{S}} Z_i Z_j) \\
&= \frac{1}{2^{2N}} \text{Tr} \left(\prod_k (1 + s_k) Z_i Z_j \prod_l (1 + s_l) Z_i Z_j \right) \\
&= \frac{1}{2^{2N}} \text{Tr} \left(\prod_k (1 + s_k) (1 + c_{ki} c_{kj} s_k) \right) \\
&= \frac{1}{2^{2N}} \text{Tr} \left(\prod_k (1 + s_k) (1 + c_{ki} c_{kj}) \right) \tag{B.3} \\
&= \frac{1}{2^{2N}} \text{Tr} \left(\prod_k (1 + s_k) \right) \prod_l (1 + c_{li} c_{lj}) \\
&= \frac{1}{2^N} \prod_l (1 + c_{li} c_{lj}) \\
&= \prod_l \mathbb{1}[c_{li} c_{lj} = 1]
\end{aligned}$$

where \mathbf{c} is a $\{1, -1\}$ valued matrix such that $Z_i s_k = c_{ki} s_k Z_i$. The one-point square term can similarly be obtained as:

$$\langle \psi_{\mathcal{S}} | Z_i | \psi_{\mathcal{S}} \rangle^2 = \prod_l \mathbb{1}[c_{li} = 1] \tag{B.4}$$

Clifford gates over N qubits \mathcal{C}_N is a class of unitary gates with the property of always mapping one Pauli string operator to another. The action of Clifford gate $U \in \mathcal{C}_N$ on a stabilizer state $|\psi_{\mathcal{S}}\rangle$ is given by:

$$U^\dagger |\psi_{\mathcal{S}}\rangle \langle \psi_{\mathcal{S}}| U = \prod_i \left(\frac{1 + U^\dagger s_i U}{2} \right) = |\psi_{\mathcal{S}^U}\rangle \langle \psi_{\mathcal{S}^U}| \tag{B.5}$$

where $\mathcal{S}^U = \{s_1^U, \dots, s_N^U\} = \{U^\dagger s_1 U, \dots, U^\dagger s_N U\}$ is still a valid set of stabilizers. So Clifford group also leaves the set of stabilizer states invariant.

A N -qubit Clifford gate is completely decided by its action on single site Pauli operators $\{X_i, Z_i\}_{i \in [N]}$. Clearly the mapping must preserve the commutation relation within

$\{X_i, Z_i\}_{i \in [N]}$. Moreover, it can be shown that any mapping that maps $\{X_i, Z_i\}_{i \in [N]}$ to the set of Pauli string operators and preserves their commutation relations uniquely (up to a phase factor) determines a $U \in \mathcal{C}_N$.

In the maintext we focused on a subset of \mathcal{C}_N that respects the Ising symmetry, namely the \mathbb{Z}_2 symmetric Clifford gates $\mathcal{C}_N^{\text{sym}}$. Such gates can be characterized by their defining property of leaving the global flipping operator $T = \prod_i X_i$ invariant:

$$\mathcal{C}_N^{\text{sym}} = \{U \in \mathcal{C}_N | U^\dagger T U = T\} \quad (\text{B.6})$$

Similar to generic Clifford gates, $\mathcal{C}_N^{\text{sym}}$ as a finite discrete group can be generated by a much smaller set of one- and two-qubit gates. The description of this set is more clear in the Majorana picture through the Jordan-Wigner transformation:

$$\begin{aligned} \gamma_{2i-1} &= \left(\prod_{j < i} X_j \right) Y_i \\ \gamma_{2i} &= \left(\prod_{j < i} X_j \right) Z_i \end{aligned} \quad (\text{B.7})$$

Because the transformation always maps a Pauli string operator to a Majorana one and vice versa, we can conclude that in the Majorana picture a Clifford gate always maps one Majorana string operator to another (up to some phase factor). The \mathbb{Z}_2 symmetry constraint guarantees that the action of $U \in \mathcal{C}_N^{\text{sym}}$ preserves the Majorana parity, and is local in both spin and Majorana picture.

Within the Majorana picture, $\mathcal{C}_N^{\text{sym}}$ is generated by two kinds of gates: the two-Majorana swap gate $U^s = \exp(\frac{\pi}{4} \gamma_1 \gamma_2)$:

$$\begin{aligned} (U^s)^\dagger \gamma_1 U^s &= \gamma_2 \\ (U^s)^\dagger \gamma_2 U^s &= -\gamma_1 \end{aligned} \quad (\text{B.8})$$

and the four-Majorana ‘‘parity gate’’ (acting like a multiplication by the local fermion parity operator) $U^p = \exp(\frac{i\pi}{4} \gamma_1 \gamma_2 \gamma_3 \gamma_4)$:

$$\begin{aligned} (U^p)^\dagger \gamma_1 U^p &= i\gamma_2 \gamma_3 \gamma_4 \\ (U^p)^\dagger \gamma_2 U^p &= -i\gamma_1 \gamma_3 \gamma_4 \\ (U^p)^\dagger \gamma_3 U^p &= i\gamma_1 \gamma_2 \gamma_4 \\ (U^p)^\dagger \gamma_4 U^p &= -i\gamma_1 \gamma_2 \gamma_3 \end{aligned} \quad (\text{B.9})$$

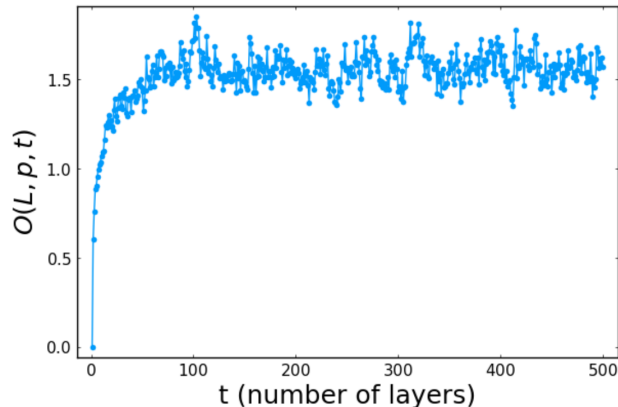


Figure B.1: Spin glass order parameter O as a function of time for a system of 512 spins at $r = 1, p = p_c = 0.39$

To numerically sample an element U from $\mathcal{C}_2^{\text{sym}}$, first a random element is picked in $\mathcal{P}_2 - \{I_1 I_2, X_1 X_2\}$ as X_1^U (\mathcal{P}_2 is the set of 2-Pauli operators), then X_2^U is automatically determined through $X_1^U X_2^U = X_1 X_2$. Z_1 is sampled from a subset of $\mathcal{P}_2 - \{I_1 I_2, X_1 X_2, X_1^U, X_2^U\}$ that commutes with X_2^U and anti-commutes with X_1^U . Finally Z_2^U can be sampled in a similar manner.

B.2 Details of sampling procedure

In the main text, we are mainly concerned about properties of the ensemble of late time steady states produced by some given circuit architecture. In this section we explain how we sample states from this ensemble numerically.

For a given random realization of circuit with size L , we first evolve the initial state (which is typically chosen to be a product state) for τL steps so that it reaches the equilibrium, then sample the evolving state every Δt steps. By increasing Δt , one can reduce the correlation between two adjacent sampled states and increase the convergence speed of target quantities. In our simulations Δt is fixed to be 32. The selection of τ is usually simulation-wise as τL needs to be larger than the time required for the system to reach equilibrium, and the latter is usually architecture and parameter dependent. To decide τ one can plot the quantity of interest as a function of time steps then take any time after which the quantity saturates divided by L as τ . As an example, FIG.B.1 shows the transient behavior of $O(L = 512, p = 0.39, t)$ at $r = 1$.

B.3 Entanglement entropy on other cross sections

We obtain entanglement entropy scaling for three additional cross sections of the phase diagram: $r = 0.25, 0.75$ (Fig. B.2) and $p = 0.75$ (Fig. B.3).

B.4 Data for the Alternative Architecture

For the alternative architecture (Fig. 2.7 in main text), we present the entanglement entropy scaling and spin glass order parameter data in Figures B.4 and B.5. Based on the data, we conclude that the volume law phase is destroyed at $p_{c,S} \approx 0.52$ and the spin glass order onsets at $p_{c,O} \approx 0.58$. The intermediate regime has spin-glass correlation and entanglement scaling that is neither clearly area or volume law. These could be due to finite size effects and require larger systems for further study.

B.5 Further data for (2+1)D circuit at $p = 0.3$

Fig.B.6 and fig.B.7 present the behaviors of $S_A(L, p)$ and $O(L, p)$ at $p = 0.3$ in (2+1)D circuit (see fig.2.6 in maintext). Our result shows that $S_A(L, p) / O(L, p)$ scales linearly with partition size / system size when $p = 0.3$.

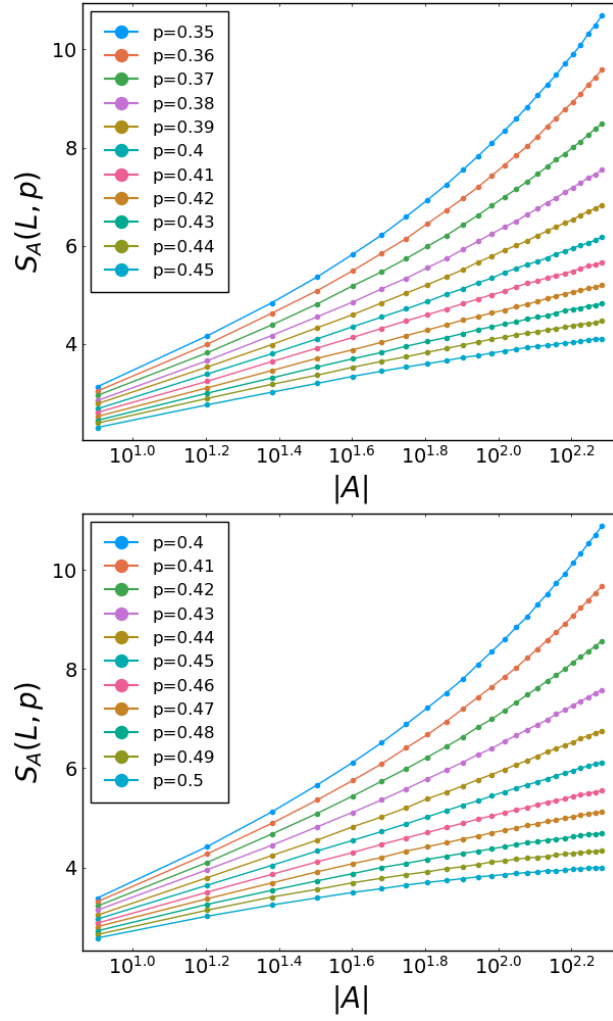


Figure B.2: Entanglement entropy versus log of partition size near the critical points at $r = 0.25$ (top) and $r = 0.75$ (bottom). $L = 768$.

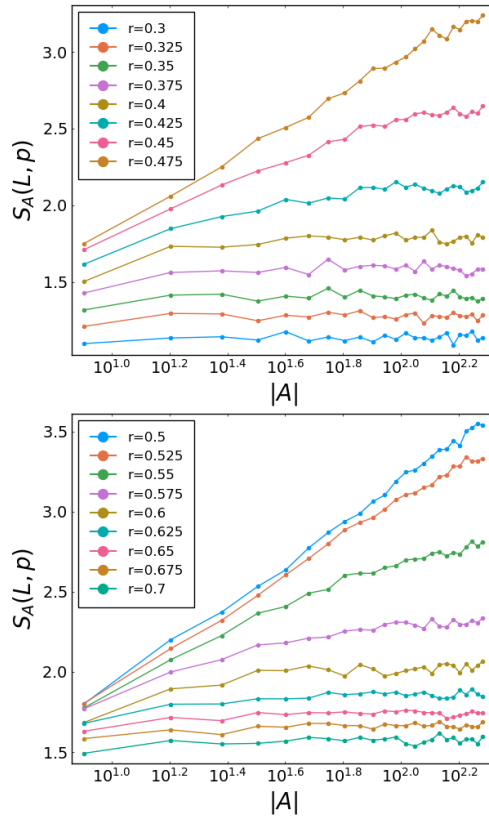


Figure B.3: Entanglement entropy versus log of partition size near the critical points at $p = 0.75$, two figures for two different ranges of r . $L = 768$.

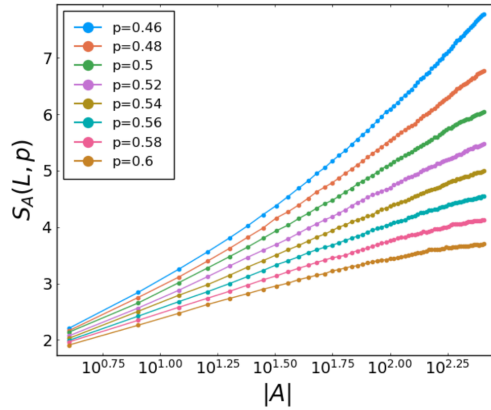


Figure B.4: Entanglement entropy versus log of partition size, for various p , for the alternative architecture.

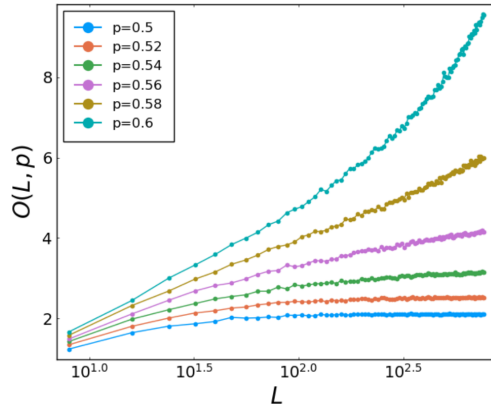


Figure B.5: Spin glass order parameter versus log of system size, for various p , for the alternative architecture.

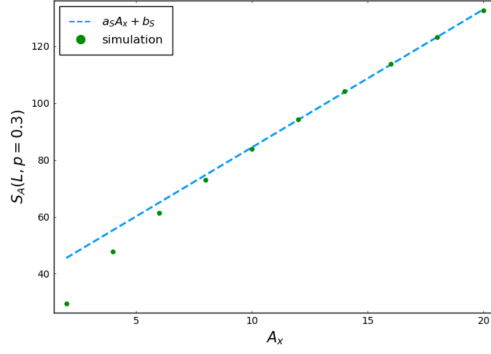


Figure B.6: Simulated bipartite entanglement entropy $S_A(L, p)$ at $p = 0.3$ in $(2+1)$ D circuit with varying partition size $A = (A_x, A_y)$. The total system size $L = (L_x, L_y) = (60, 20)$ and $A_y = 20$ are fixed while A_x is varying. For dashed line $(a_S, b_S) = (4.87, 35.85)$

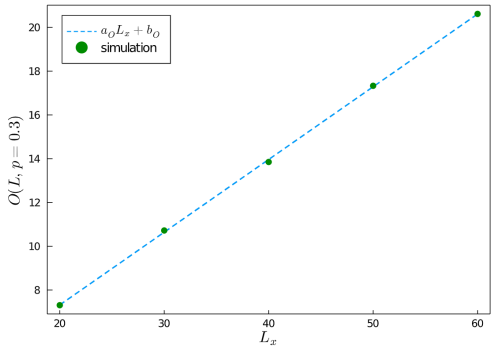


Figure B.7: Simulated spin-glass order parameter $O(L, p)$ at $p = 0.3$ in $(2+1)$ D circuit with $L_y = 20$ fixed and L_x varying. For dashed line $(a_O, b_O) = (0.33, 0.67)$

Appendix C

Appendix for Chapter.3

C.1 Monitored dynamics as a quantum channel

In the main part of the paper, we focused on the trajectory dynamics $C_{\mathbf{m}}$ corresponding to a single measurement outcome sequence \mathbf{m} . In this appendix, we study the ensemble of all the trajectory dynamics $\{C_{\mathbf{m}}\}$ that can arise in a monitored circuit with given unitary gates and measurement locations.

To study the ensemble of dynamics $\{C_{\mathbf{m}}\}$, we introduce a set of registers M to record all the measurement outcomes. The whole process can be viewed as a Clifford quantum channel from P to $P \cup M$ [29, 168], written as:

$$\mathcal{E}_C(\rho_P) = \sum_{\mathbf{m} \in \{0,1\}^{|M|}} |\mathbf{m}\rangle \langle \mathbf{m}|_M \otimes (C_{\mathbf{m}} \rho C_{\mathbf{m}}^\dagger)_P. \quad (\text{C.1})$$

Here we have made each measurement outcome decoherent by applying a complete dephasing channel on registers.

Given a Pauli operator O_A defined on $A \subset P$, we are naturally led to look for a Pauli operator \tilde{O}_S defined on $S \subset Q$ such that:

$$\text{tr}(O_A \rho) = \text{tr}(\tilde{O}_S \mathcal{E}_C(\rho)) \quad \forall \rho. \quad (\text{C.2})$$

Accordingly, we use the following quantity as a measure for the amount of information transferred from A into S by the stabilizer channel \mathcal{E} :

$$H_{A \rightarrow S}(\mathcal{E}) \equiv |\{O \in \mathcal{P}_A : \exists \tilde{O}_S \in \mathcal{P}_S \text{ s.t. } O = \mathcal{E}^\dagger(\tilde{O}_S)\}|, \quad (\text{C.3})$$

where \mathcal{P}_A (\mathcal{P}_S) denotes the set of Pauli operators supported on A (S).

The central result of this appendix is a relation between the entanglement properties of a single trajectory dynamics and that of the ensemble of dynamics.

Theorem 4. Letting \mathcal{E}_C be a Clifford monitored dynamics and $A, B \subseteq P$, we have:

$$I_{A_R:B_P}(|\phi_{\mathbf{m}}\rangle) = \log_2 H_{A \rightarrow B \cup M}(\mathcal{E}_C) - \log_2 H_{A \rightarrow M}(\mathcal{E}_C). \quad (\text{C.4})$$

On the *r.h.s* of the equation, the first (second) term measures how much information is transmitted from A to $B \cup M$ (to B). Therefore, $I_{A_R:B_P}(t)$ quantifies the amount of *extra* information within the input A extractable within the output B , given all the classical measurement outcomes M are known. Below, we present a proof of Thm.4.

It is convenient to introduce the Choi state:

$$\begin{aligned} \Phi_{\mathcal{E}} &= \frac{1}{\dim P} \sum_{i,j} \mathcal{E}_C(|i\rangle \langle j|_P) \otimes |i\rangle \langle j|_R \\ &= \sum_{\mathbf{m} \in \{0,1\}^{|\mathcal{M}|}} p_{\mathbf{m}}(|\mathbf{m}\rangle \langle \mathbf{m}|_M) \otimes (|\phi_{\mathbf{m}}\rangle \langle \phi_{\mathbf{m}}|)_{PR}. \end{aligned} \quad (\text{C.5})$$

Stabilizer generators of the Choi state $\Phi_{\mathcal{E}}$ can be related to the recoverability of operators via the following lemma.

Lemma 1. Given a stabilizer channel $\mathcal{E} : L(\mathcal{H}_P) \rightarrow L(\mathcal{H}_Q)$, $O \in \mathcal{P}_P$ is recovered by $\tilde{O} \in \mathcal{P}_Q$ through \mathcal{E} if and only if $O^T \otimes \tilde{O}$ is a stabilizer of $\Phi_{\mathcal{E}}$.

Proof. Starting from the definition of recoverability, we have

$$\begin{aligned} O &= \mathcal{E}^\dagger(\tilde{O}) \\ \Leftrightarrow \mathcal{E}^\dagger(\tilde{O})O &= \mathbb{I}_P \\ \Leftrightarrow \text{tr}(\mathcal{E}^\dagger(\tilde{O})O) &= \dim P \\ \Leftrightarrow \text{tr}(\Phi_{\mathcal{E}} O^T \otimes \tilde{O}) &= 1. \end{aligned} \quad (\text{C.6})$$

The second last equivalence follows from the fact that \mathbb{I} is the only Pauli operator with non-zero trace and the fact that \mathcal{E}^\dagger maps Pauli operators to Pauli operators. The last

equivalence is due to

$$\begin{aligned}
\text{tr}(\mathcal{E}^\dagger(\tilde{O})O) &= \text{tr}(\tilde{O}\mathcal{E}(O)) \\
&= \text{Diagram 1} \\
&= \text{Diagram 2} \\
&= \dim P \cdot \text{tr}(\Phi_{\mathcal{E}} O^T \otimes \tilde{O}).
\end{aligned} \tag{C.7}$$

The last condition in Eq. (C.6) shows that $O^T \otimes \tilde{O}$ is a stabilizer. This completes the proof. \square

Next, we relate the amount of transferred operators to the mutual information, as summarized in the following lemma.

Lemma 2. Given a stabilizer channel $\mathcal{E} : L(\mathcal{H}_P) \rightarrow L(\mathcal{H}_Q)$ and two regions $A \subseteq P$, $S \subseteq Q$, we have $\log_2 H_{A \rightarrow S}(\mathcal{E}) = I_{A:S}(\Phi_{\mathcal{E}})$.

Proof. Letting S be the stabilizer group of $\Phi_{\mathcal{E}}$. Define $G_S = G \cap \mathcal{P}_S$ and similarly G_{AS} . By lemma 1, we have:

$$\log_2 H_{A \rightarrow B}(\mathcal{E}) = \log_2 |G_{AS}| - \log_2 |G_S|. \tag{C.8}$$

Here, $\log_2 |G_B|$ is subtracted since the \tilde{O} in lemma 1 has the redundancy resulting from multiplying stabilizer operators in G_S .

Let us recall the formula for entanglement entropy:

$$S_{AS} = |A| + |S| - \log_2 |G_{AS}|, \quad S_S = |S| - \log_2 |G_S|. \tag{C.9}$$

We obtain

$$\log_2 H_{A \rightarrow S}(\mathcal{E}) = |A| + |S| - S_{AS} - |S| + S_S = I_{A:S}(\Phi_{\mathcal{E}}). \tag{C.10}$$

The last equation is due to $S_A = |A|$ since A is maximally mixed. This completes the proof. \square

We are now ready to prove Thm.4. Recall that entanglement of the ensemble state $\Phi_{\mathcal{E}}$ and that of each trajectory $|\phi_{\mathbf{m}}\rangle$ are related by the following property of the conditional entropy:

$$\mathbb{E}_{\mathbf{m}}[S_X(|\phi_{\mathbf{m}}\rangle)] = S_{X|M}(\Phi_{\mathcal{E}}) = S_{X \cup M}(\Phi_{\mathcal{E}}) - S_M(\Phi_{\mathcal{E}}). \quad (\text{C.11})$$

Here X is any subregion of $P \cup R$, and $\mathbb{E}_{\mathbf{m}}$ denotes averaging over all the trajectories:

$$\mathbb{E}_{\mathbf{m}}[\dots] \equiv \sum_{\mathbf{m}} p_{\mathbf{m}}(\dots)_{\mathbf{m}}. \quad (\text{C.12})$$

Moreover, for a Clifford monitored circuit, entanglement entropies of $|\phi_{\mathbf{m}}\rangle$ do not depend on \mathbf{m} as long as $p_{\mathbf{m}} \neq 0$.

We are now ready to derive Eq. (C.4):

$$\begin{aligned} I_{A:B}(|\phi_{\mathbf{m}}\rangle) &= (S_A + S_B - S_{A \cup B})(|\phi_{\mathbf{m}}\rangle) \\ &= (S_{A_R|M} + S_{B_P|M} - S_{A_R \cup B_P|M})(\Phi_{\mathcal{E}}) \\ &= (I_{A_R:(B_P \cup M)} - I_{A_R:M})(\Phi_{\mathcal{E}}) \\ &= \log_2 H_{A \rightarrow B \cup M}(\mathcal{E}) - \log_2 H_{A \rightarrow M}(\mathcal{E}). \end{aligned} \quad (\text{C.13})$$

Here the second equality follows from Eq. (C.11), and the last equality follows from lemma 1. This completes the proof of Thm. 4.

C.2 Details about random polymer simulation

To perform numerical simulations of DPRE, we consider a lattice discretization of $D_V(\mathbf{x}, \mathbf{y})$ defined in Eq. (3.66). We replace the continuous spacetime manifold with a $L \times T$ grid, then change the continuous shortest path $\mathbf{z}(\tau)$ into a discrete one \mathbf{z}_i on the grid:

$$D_V^{\text{discretized}}(\mathbf{x}, \mathbf{y}) = \min_{\substack{\mathbf{z}: \mathbf{z}_0 = \mathbf{x}, \\ \mathbf{z}_{l(\mathbf{z})} = \mathbf{y}}} \left(\sum_{i=0}^{l(\mathbf{z})-1} V_{(\mathbf{z}_i, \mathbf{z}_{i+1})} \right), \quad (\text{C.14})$$

where the integer valued $l(\mathbf{z})$ is the total length of the path \mathbf{z} . The discretized random potential $V_{(\mathbf{z}, \mathbf{z}')}$ is defined on the grid's links, and takes independent values at different locations. The problem, when formulated this way, is equivalent to looking for the ground state domain-wall of a random bond Ising model at zero temperature [62].

For simulations presented in Sec. 3.4, for each site \mathbf{z} we take $V_{\mathbf{z}}$ to be a uniform distribution on the interval $(0, 1)$. Since all V s are positive, the shortest path can be solved with the Dijkstra's algorithm using $O(LT \log(LT))$ time.

Appendix D

Appendix for Chapter.4

D.1 Various short proofs

D.1.1 Derivation of Eq.(4.11)

Let us assume $\mathcal{E}_{A \rightarrow A'}$ approximately preserves the correlation of a bi-partite state ρ_{AB} :

$$I_{A:B}(\rho) - I_{A':B}(\mathcal{E}_{A \rightarrow A'}(\rho)) = \epsilon, \quad (\text{D.1})$$

After defining W and $\sigma_{A'EB}$ the same way as in the proof of Thm.2, the condition above is equivalent to:

$$I_{B:E|A'}(\sigma_{A'EB}) = \epsilon. \quad (\text{D.2})$$

Using the result in [81], there exists a reconstruction map $\mathcal{T}_{A' \rightarrow A'E}$ to approximately reconstruct $\sigma_{A'EB}$ from $\sigma_{A'B}$, with the approximation error bounded as:

$$\epsilon \geq -2 \log_2 F(\sigma_{A'EB}, \mathcal{T}_{A' \rightarrow A'E}(\sigma_{A'B})). \quad (\text{D.3})$$

We still define the recovery map $\mathcal{D}_{A' \rightarrow A}$ using Eq.(4.8). We have:

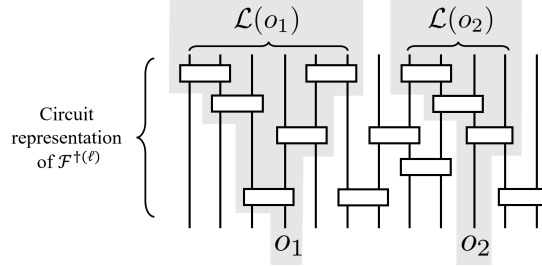
$$\begin{aligned} & F(\rho_{AB}, \mathcal{D} \circ \mathcal{E}(\rho_{AB})) \\ &= F\left(\text{tr}_R\left(U_W^\dagger U_W ((\rho_{AB}) \otimes |0\rangle_R \langle 0|) U_W^\dagger U_W\right), \text{tr}_R\left(U_W^\dagger \mathcal{T}(\sigma_{A'B}) U_W\right)\right) \\ &\geq F\left(U_W ((\rho_{AB}) \otimes |0\rangle_R \langle 0|) U_W^\dagger, \mathcal{T}(\sigma_{A'B})\right) \\ &= F(\sigma_{A'EB}, \mathcal{T}(\sigma_{A'B})), \end{aligned} \quad (\text{D.4})$$

where the inequality is due to the monotonicity of F under quantum channels. Combining the two expressions above, we arrive at the approximate recoverability we want:

$$\epsilon \geq -\log_2 F(\rho_{AB}, \mathcal{D} \circ \mathcal{E}(\rho_{AB})) \quad (\text{D.5})$$

D.1.2 Derivation of Eq.(4.22)

We assume that the two operators $o_1^{(\ell)} = o_1$ and $o_2^{(\ell)} = o_2$ have non-overlapping lightcones $\mathcal{L}(o_1)$ and $\mathcal{L}(o_2)$ in the circuit representation of \mathcal{F}^\dagger , as illustrated below:



To prove Eq.(4.22), we decompose \mathcal{F}^\dagger into $O(1)$ number of layers (as is drawn in the figure above). Each individual layer is of the form $\mathcal{E}_1^\dagger \otimes \mathcal{E}_2^\dagger \otimes \dots \otimes \mathcal{E}_K^\dagger$, where each \mathcal{E}_I^\dagger is a dual channel that acts on a block of sites referred to as B_I such that $B_I \cap B_J = \emptyset$ whenever $I \neq J$. We inspect $o_1 o_2$'s transformation under a single layer. Assuming o_1, o_2 are supported on B_I and B_J respectively, we have

$$\mathcal{E}_1^\dagger \otimes \mathcal{E}_2^\dagger \otimes \dots \otimes \mathcal{E}_K^\dagger(o_1 o_2) = \mathcal{E}_I^\dagger(o_1) \mathcal{E}_J^\dagger(o_2) \quad (\text{D.6})$$

because dual channels are unital. By doing induction over all the layers in \mathcal{F}^\dagger , we arrive at our conclusion Eq.(4.22).

D.1.3 Derivation of Eq.(4.39)

We prove the channel equality by checking its action on $|0\rangle\langle 0|$, $|0\rangle\langle 1|$ and $|1\rangle\langle 1|$, which form a basis of linear operators for a single qubit.

We first act on the isometry and the noise channel:

$$\begin{aligned}
(\mathcal{N}_p^X)^{\otimes b} \circ \mathcal{U}_{w_b}(|0\rangle\langle 0|) &= \sum_{\mathbf{s} \in \{0,1\}^b} p^{|\mathbf{s}|} (1-p)^{b-|\mathbf{s}|} |\mathbf{s}\rangle\langle \mathbf{s}| = \sigma_{00} \\
(\mathcal{N}_p^X)^{\otimes b} \circ \mathcal{U}_{w_b}(|0\rangle\langle 1|) &= \sum_{\mathbf{s} \in \{0,1\}^b} p^{|\mathbf{s}|} (1-p)^{b-|\mathbf{s}|} |\mathbf{s}\rangle\langle \bar{\mathbf{s}}| = \sigma_{01} \\
(\mathcal{N}_p^X)^{\otimes b} \circ \mathcal{U}_{w_b}(|1\rangle\langle 1|) &= \sum_{\mathbf{s} \in \{0,1\}^b} p^{|\mathbf{s}|} (1-p)^{b-|\mathbf{s}|} |\bar{\mathbf{s}}\rangle\langle \bar{\mathbf{s}}| = \sigma_{11}
\end{aligned} \tag{D.7}$$

Then we act the majority vote channel. Its action on σ_{00} is:

$$\begin{aligned}
\mathcal{E}(\sigma_{00}) &= \sum_{\mathbf{s}} p^{|\mathbf{s}|} (1-p)^{b-|\mathbf{s}|} |\text{maj}(\mathbf{s})\rangle\langle \text{maj}(\mathbf{s})| \otimes \text{tr}(|\text{diff}(\mathbf{s})\rangle\langle \text{diff}(\mathbf{s})|) \\
&= \left(\sum_{\mathbf{s}:|\mathbf{s}|<b/2} p^{|\mathbf{s}|} (1-p)^{b-|\mathbf{s}|} \right) |0\rangle\langle 0| + \left(\sum_{\mathbf{s}:|\mathbf{s}|>b/2} p^{|\mathbf{s}|} (1-p)^{b-|\mathbf{s}|} \right) |1\rangle\langle 1| \\
&= (1-p') |0\rangle\langle 0| + p' |1\rangle\langle 1| \\
&= \mathcal{N}_{p'}^X(|0\rangle\langle 0|),
\end{aligned} \tag{D.8}$$

where

$$p' = \sum_{\mathbf{s}:|\mathbf{s}|>b/2} p^{|\mathbf{s}|} (1-p)^{b-|\mathbf{s}|} = \sum_{k=(b+1)/2}^b \binom{b}{k} p^k (1-p)^{b-k} \tag{D.9}$$

Following a very similar calculation, we have:

$$\begin{aligned}
\mathcal{E}(\sigma_{01}) &= (1-p') |0\rangle\langle 1| + p' |1\rangle\langle 0| = \mathcal{N}_{p'}^X(|0\rangle\langle 1|) \\
\mathcal{E}(\sigma_{11}) &= (1-p') |1\rangle\langle 1| + p' |0\rangle\langle 0| = \mathcal{N}_{p'}^X(|1\rangle\langle 1|)
\end{aligned} \tag{D.10}$$

Then we obtain Eq.(4.39).

D.2 Convergence of real-space RGs

In Sec.4.1.4 it is stated that if a mixed state's RG flow $\{\rho^{(0)}, \rho^{(1)}, \dots\}$ satisfies the following conditions for large enough ℓ :

$$\text{Eq.(4.24): } F(\rho^{(\ell)}, \rho^{(\infty)}) \simeq \exp(-\alpha \theta^{(\ell)} L^{(\ell)})$$

$$\text{Eq.(4.25): } \theta^{(\ell+1)} \lesssim (\theta^{(\ell)})^\gamma \quad \text{when } \theta^{(\ell)} \rightarrow 0_+,$$

then choosing

$$\ell^* = O(\log \log(L/\epsilon)) \quad (\text{D.11})$$

guarantees $F(\rho^{(\ell^*)}, \rho^{(\infty)}) > 1 - \epsilon$ for a small ϵ . $L^{(\ell)} = L/b^\ell$ is the renormalized system size.

In this appendix we first prove the statement, then show the validness of conditions Eqs.(4.24),(4.25) in several scenarios, including all examples we studied in the main text.

Suppose $\ell_0 = O(1)$ simultaneously satisfies the following two conditions: Eq.(4.25) holds when $\ell > \ell_0$ and that $\theta^{(\ell_0)} := \theta_0 < 1$. Iterating the condition $(\ell - \ell_0)$ times, we get:

$$\theta^{(\ell)} < (\theta_0)^{\gamma^{\ell-\ell_0}}. \quad (\text{D.12})$$

We need to find how large ℓ needs to be, in order to satisfy:

$$\exp(-\alpha\theta^{(\ell)}L^{(\ell)}) > 1 - \epsilon, \quad (\text{D.13})$$

which is implied by (note that $L^{(\ell)} < L$):

$$\theta^{(\ell)} < \epsilon/L, \quad (\text{D.14})$$

which is further implied by:

$$\ell > \ell_0 + \log_\gamma \log_{\theta_0^{-1}}(L/\epsilon) = O(\log \log(L/\epsilon)) \quad (\text{D.15})$$

This completes the proof.

In the rest of this appendix section, we show several scenarios where the condition Eq.(4.24)(4.25) is satisfied. For the case of matrix product state with a tree tensor network RG, the analysis is done thoroughly in a recent work [212].

D.2.1 Classical statistical mechanics models

Let us consider a classical statistical mechanics model with the Hamiltonian:

$$H_g = H_0 - gH' \quad (\text{D.16})$$

We assume that under some given RG process, H_0 is the RG fixed point while H' is an irrelevant perturbation with respect to H_0 . Further, we assume both H_0 and H' are summations of spatially local terms each involving $O(1)$ number of sites. Further, each spin only appears $O(1)$ number of terms, and terms are uniformly bounded.

Let $\rho_g \propto \exp(-H_g)$ be the Gibbs state of H_g . We are interested in how fast it approaches the fixed-point ρ_0 . We use the fidelity as a measure of closeness between the two states:

$$F(\rho_g, \rho_0) = |\sqrt{\rho_g}\sqrt{\rho_0}|_1 = \text{tr}(e^{-H_g/2}e^{-H_0/2})/\sqrt{Z_g Z_0} = Z_{g/2}/\sqrt{Z_g Z_0} \quad (\text{D.17})$$

where $Z_g := \text{tr}(\rho_g)$ is the partition function. We note that since ρ_g is a classical state, the fidelity function F coincides with the Bhattacharyya coefficient, a measure of similarity for classical distributions.

We have:

$$Z_g = \text{tr} \left(e^{-H_0} \sum_n \frac{g^n}{n!} (H')^n \right) = Z_0 \sum_n \frac{g^n}{n!} \langle (H')^n \rangle_0 \quad (\text{D.18})$$

Without loss of generality, we assume each term in H' is positive, so that: $0 \leq \langle (H')^n \rangle_0 \leq |H'|^n$. Thus we have:

$$Z_0 \leq Z_g \leq Z_0 e^{g|H'|} \quad (\text{D.19})$$

Combining with Eq.(D.17), we get:

$$F(\rho_g, \rho_0) \geq e^{-g|H'|} \quad (\text{D.20})$$

Since $|H'|$ is a summation of spatially local terms whose norms are uniformly bounded, $|H'|$ must be upper-bounded by αL for some $\alpha = O(1)$ and large L . This leads to:

$$F(\rho_g, \rho_0) \geq e^{-g\alpha L} \quad (\text{D.21})$$

Thus Eq.(4.24) is satisfied. The Eq.(4.25) is satisfied because g is an irrelevant coupling for a non-critical fixed point.

D.2.2 Noisy GHZ state in Sec.4.3

(a) Bit flip noise

The fidelity function is:

$$\begin{aligned} F(\rho_{p,L}^X, \rho_{0,L}^X) &= \langle \text{GHZ} | \rho_{p,L}^X | \text{GHZ} \rangle \\ &= \frac{1}{2} \sum_{\mathbf{s} \in \{0,1\}^L} p^{|\mathbf{s}|} (1-p)^{L-|\mathbf{s}|} \langle \text{GHZ} | (|\mathbf{s}\rangle \langle \mathbf{s}| + |\bar{\mathbf{s}}\rangle \langle \mathbf{s}| + |\mathbf{s}\rangle \langle \bar{\mathbf{s}}| + |\bar{\mathbf{s}}\rangle \langle \bar{\mathbf{s}}|) | \text{GHZ} \rangle \\ &= (1-p)^L + p^L \\ &\approx e^{-pL} \end{aligned} \quad (\text{D.22})$$

The approximation follows from $p \ll 1$. The iteration relation of p satisfies:

$$p' = \sum_{k=(b+1)/2}^b \binom{b}{k} p^k (1-p)^{b-k} \leq 2^{b-1} p^{(b+1)/2} \leq p^{b/2} \quad (\text{D.23})$$

the last inequality holds if $p < 2^{-2b+2}$, which can be always achieved after an $O(1)$ number of RG iterations starting from any $p \in (0, 0.5)$.

(b) Phase-flip noise

The fidelity function is:

$$\begin{aligned} F(\rho_{p,L}^Z, \rho_{1/2,L}^Z) &= \text{tr} \sqrt{\sqrt{\rho_{1/2,L}^Z} \rho_{p,L}^Z \sqrt{\rho_{1/2,L}^Z}} \\ &= \frac{1}{2} + \frac{1}{2} \sqrt{1 - (1 - 2p)^{2L}} \end{aligned} \quad (\text{D.24})$$

We notice that the fidelity function actually goes to 1 when $L \rightarrow \infty$. This can be treated as a special case of the condition Eq.(4.24) for $\alpha = 0$.

The iteration relation for p around the stable fixed-point $p = 0.5$ is:

$$(p' - 1/2) = (p - 1/2)^b \quad (\text{D.25})$$

D.2.3 Thermal toric code state in Sec.4.4.2

We consider the fidelity between the finite temperature state and the infinite temperature one. Note that the latter is proportional to identity. Thus,

$$\begin{aligned}
F(\rho_\beta, \rho_0) &= 2^{-\frac{L^2}{2}} \text{tr} \sqrt{\rho_\beta} \\
&= 2^{-\frac{L^2}{2}} \sum_{\mathbf{m}, \mathbf{e}, \mathbf{l}} \sqrt{\text{Pr}_m(\mathbf{m}) \text{Pr}_e(\mathbf{e}) \text{Pr}_l(\mathbf{l})} \\
&= 2^{-\frac{L^2}{2} + 1} \left(\sum_{\mathbf{m}} \sqrt{\text{Pr}_m(\mathbf{m})} \right)^2 \\
&\geq 2^{-\frac{L^2}{2} + 1} \left(\sum_{\mathbf{m}: \pi(\mathbf{m})=0} p_\beta^{|\mathbf{m}|/2} (1 - p_\beta)^{(L^2/2 - |\mathbf{m}|)/2} \right)^2 \\
&= 2^{-\frac{L^2}{2} + 1} (1 - p_\beta)^{L^2/2} \left(\sum_{\mathbf{m}: \pi(\mathbf{m})=0} e^{-\beta|\mathbf{m}|} \right)^2 \\
&\geq 2^{-\frac{L^2}{2} + 1} 2^{-L^2/2} \left(2^{L/2-1} e^{-\beta L^2/2} \right)^2 \\
&= 2^{-\beta L^2 - 1}
\end{aligned} \tag{D.26}$$

The iteration relation of the inverse temperature β is given by

$$\beta' = \tanh^{-1} \tanh^4 \beta \approx \beta^4 \tag{D.27}$$

at small β , which satisfies the condition.

D.3 Symmetric RG of $\mathbb{Z}_2 \times \mathbb{Z}_2$ cluster state

In this appendix, we consider the RG of a mixed SPT (symmetry protected topological) state. The problem was first considered in [115], where the authors use the string order parameter as a definition for the mixed state SPT. They show that, when a pure SPT state is subject to noise, the string order parameter (*i.e.* the SPT phase) is preserved if and only if the noise is strongly symmetric, meaning that all its Kraus operators commute with the symmetry operator.

The above definition (via string order parameters) of mixed-state SPT actually agrees with the LC transformation based definition. To show this, we put forward a symmetric RG transformation that brings the noisy state back to a clean one. The RG is the same as the one proposed in [195]. Although in [195] the circuit is designed for recognizing pure-state phases, we point out that it can be readily applied on a mixed-state SPT states.

Here we demonstrate the principle with a simple (1+1)D SPT state, namely the $Z_2 \times Z_2$ SPT. Consider a 1D lattice spin chain where in the bulk each site contains 2 qubits, labeled as A and B . The pure SPT wavefunction can be written as:

$$|\psi\rangle = \bigotimes_{i=-\infty}^{+\infty} |\text{EPR}_{i_B, (i+1)_A}\rangle, \quad (\text{D.28})$$

where each $|\text{EPR}_{i,j}\rangle := \frac{1}{\sqrt{2}}(|0_i 0_j\rangle + |1_i 1_j\rangle)$. Note that the above way of defining the $Z_2 \times Z_2$ SPT is related to the cluster state by rotating the two spins within a unit cell with a CNOT gate. It is straightforward to verify that the state has a $Z_2 \times Z_2$ symmetry generated by 2 generators:

$$U^X = \prod_i X_{i_A} X_{i_B}, \quad U^Z = \prod_i Z_{i_A} Z_{i_B}. \quad (\text{D.29})$$

Two generators define two string order parameters:

$$S_{ij}^X = X_{i_B} \left(\prod_{k=i+1}^{j-1} X_{k_A} X_{k_B} \right) X_{j_A}, \quad S_{ij}^Z = Z_{i_B} \left(\prod_{k=i+1}^{j-1} Z_{k_A} Z_{k_B} \right) Z_{j_A} \quad (\text{D.30})$$

One signature of the SPT order in $|\psi\rangle$ is that expectation value of string order parameters does not decay with $|i - j|$.

We consider the XX dephasing channel:

$$\mathcal{N}_p^{XX}(\cdot) = (1 - p)(\cdot) + pX_A X_B(\cdot)X_A X_B, \quad (\text{D.31})$$

whose action can be realized by the pair of spins within each site being flipped simultaneously with probability p . The channel is strongly symmetric under U_X and U_Z , because its Kraus operators commute with symmetry operators.

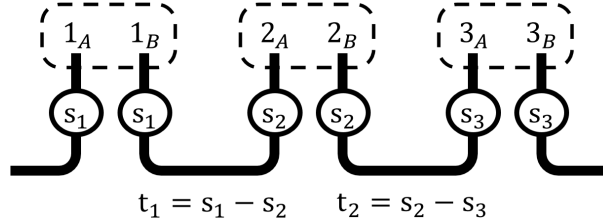
The noisy SPT state of our interest is obtained by applying \mathcal{N}_p uniformly upon ψ :

$$\sigma_{p,L} = \mathcal{N}_p^{\otimes L}(|\psi\rangle \langle \psi|). \quad (\text{D.32})$$

It will be useful to unravel σ_p into a classical mixture of pure SPT states decorated by domain walls:

$$\begin{aligned}\sigma_p &= \mathbb{E}[|\psi_{\mathbf{s}}\rangle \langle \psi_{\mathbf{s}}|] = \sum_{\mathbf{s} \in \{0,1\}^L} P(\mathbf{s}) |\psi_{\mathbf{s}}\rangle \langle \psi_{\mathbf{s}}| \\ P(\mathbf{s}) &:= p^{|\mathbf{s}|} (1-p)^{L-|\mathbf{s}|} \\ |\psi_{\mathbf{s}}\rangle &:= \bigotimes_i X_{i_A}^{s_i} X_{(i+1)_B}^{s_{i+1}} |\text{EPR}_{i_B, (i+1)_A}\rangle\end{aligned}\tag{D.33}$$

Now we focus on a block of b sites within the state and devise the channel that coarse-grains the block. The part of the $|\psi_{\mathbf{s}}\rangle$ within the block can be drawn as (for $b = 3$):



where each hollowed circle is either an identity gate if $s = 0$ or an X gate if $s = 1$. Each s_i is an independent Bernoulli random variable with chance p .

The renormalized site is formed by qubits $\{1_A, b_B\}$, while the $(b-2)$ entangled pairs supporting on the remaining qubits $\{1_B, 2_A, 2_B, \dots, b_A\}$ can help us infer and correct errors s_1 and s_b before they get traced out. More concretely, the coarse-graining channel \mathcal{E} 's action is the following:

1. Measure each Bell pairs *within* the block in the ZZ basis, whose outcome records the domain-walls between s_i , i.e., $\{t_1 = s_1 - s_2, t_2 = s_2 - s_3, \dots, t_{b-1} = s_{b-1} - s_b\}$. The outcomes decide all the s_i up to a global flip, i.e. once we assume a value for the first error $s_1 = \hat{s}_1$, the remaining s are also uniquely determined by: $\hat{s}_k = (\sum_{j=1}^{k-1} t_j) - \hat{s}_1$.
2. Assume

$$\hat{s}_1 = \operatorname{argmax}_{s_1 \in \{0,1\}} \Pr(s_1 | t_1, \dots, t_{b-1})\tag{D.34}$$

to be the actual error, and correct all sites within the block. Namely, applying $X_{i_A} X_{i_B}$ if $\hat{s}_i = 1$. After this step, all Bell pairs within the block are noiseless and decoupled from $\{1_B, b_A\}$.

3. Trace out $\{1_B, 2_A, 2_B, \dots, b_A\}$. Then we obtain the renormalized site with $\{1_B, b_A\}$,

It is clear that channel \mathcal{E} is strongly symmetric under $Z_2 \times Z_2$ since each individual step is. The renormalized site gets a XX error if and only if $\hat{s}_1 \neq s_1$, whose probability we denote as p' . Thus we find that the normalized state is still a symmetrically dephased SPT state, but with a normalized noise strength p' :

$$\mathcal{E}^{\otimes \frac{L}{b}}(\sigma_{p,L}^{\text{SPT}}) = \sigma_{p',L/b}^{\text{SPT}} \quad (\text{D.35})$$

The explicit form of p' is:

$$p' = \sum_{k=(b+1)/2}^b \binom{b}{k} p^k (1-p)^{b-k} \quad (\text{D.36})$$

Thus we obtain a similar RG flow as in the X -dephased GHZ state studied in Sec.4.3: symmetrically decohered SPT state flows back to a pure SPT state when $0 \leq p < 0.5$.

Appendix E

Appendix for Chapter.6

E.1 Petz recovery map

Let \mathcal{H} , \mathcal{H}' be two Hilbert spaces. For a density operator ρ defined on \mathcal{H} and a completely positive trace preserving (CPTP) map $\mathcal{E} : \mathcal{B}(\mathcal{H}) \rightarrow \mathcal{B}(\mathcal{H}')$, the CPTP map called twirled Petz map $\mathcal{P}_{\mathcal{E},\rho} : \mathcal{B}(\mathcal{H}') \rightarrow \mathcal{B}(\mathcal{H})$ is defined as:

$$\mathcal{P}_{\mathcal{E},\rho}[\cdot] = \int_{-\infty}^{\infty} f(\tau) \rho^{\frac{1-i\tau}{2}} \mathcal{E}^{\dagger} \left[\mathcal{E}[\rho]^{\frac{-1+i\tau}{2}} (\cdot) \mathcal{E}[\rho]^{\frac{-1-i\tau}{2}} \right] \rho^{\frac{1+i\tau}{2}} d\tau \quad (\text{E.1})$$

where $f(t) \equiv \frac{\pi}{2(\cosh(\pi t)+1)}$, and the map \mathcal{E}^{\dagger} is defined through the relation $\text{tr}(\mathcal{E}^{\dagger}[X]Y) = \text{tr}(X\mathcal{E}[Y])$

The importance of the twirled Petz map comes from the following inequality concerning approximate quantum sufficiency [108]:

$$D(\rho\|\sigma) - D(\mathcal{E}[\rho]\|\mathcal{E}[\sigma]) \geq -2 \log F(\rho, \mathcal{P}_{\mathcal{E},\sigma} \circ \mathcal{E}[\rho]) \quad (\text{E.2})$$

Where ρ and σ are both states defined on \mathcal{H} . $D(\rho\|\sigma) \equiv \text{tr}(\rho(\log \rho - \log \sigma))$ and $F(\cdot, \cdot)$ is the fidelity between states. In plain language, the theorem states that the twirled Petz map $\mathcal{P}_{\mathcal{E},\sigma}$ approximately reverses the action of \mathcal{E} on any state ρ whose relative entropy with respect to σ does not change much under \mathcal{E} .

In order to derive Eq.(6.4), we take $\rho = \rho_{ABC}$ and $\sigma = \rho_{AB} \otimes \rho_C$, and let \mathcal{E} be a channel acting on A only. In this case the *l.h.s.* becomes:

$$I_{\rho}(AB : C) - I_{\mathcal{E}[\rho]}(AB : C) = I_{\rho}(A : C|B) - I_{\mathcal{E}[\rho]}(A : C|B) \quad (\text{E.3})$$

which comes from $I(A : C|B) \equiv I(AB : C) - I(B : C)$. We notice that $I_\rho(B : C) = I_{\mathcal{E}[\rho]}(B : C)$ because \mathcal{E} acts on A only. To bound the *r.h.s.* in terms of trace norm, we use the relation:

$$1 - F(\rho, \sigma) \geq \frac{1}{4} |\rho - \sigma|_1^2 \quad \Rightarrow \quad -2 \log F \geq \frac{1}{2 \ln 2} |\rho - \sigma|_1^2 \quad (\text{E.4})$$

Combining two expressions together, we obtain:

$$I_\rho(A : C|B) - I_{\mathcal{E}[\rho]}(A : C|B) \geq (2 \ln 2)^{-1} \cdot |\mathcal{P}_{\mathcal{E}, \rho_{AB}} \circ \mathcal{E}[\rho] - \rho|_1^2 \quad (\text{E.5})$$

which is also Eq.(6.4).

E.2 Derivation of Eq.(6.8)

The recovery error of a single layer is bounded as:

$$\begin{aligned} \left| \tilde{\mathcal{C}}_\ell \circ \mathcal{C}_\ell[\rho_{\ell-1}] - \rho_{\ell-1} \right|_1 &= \left| \sum_{x=1}^{x_{\max}-1} \left(\tilde{\mathcal{E}}_{x,\ell} \circ \mathcal{E}_{x,\ell} [\mathcal{C}_{<x,\ell}[\rho_{\ell-1}]] - \mathcal{C}_{<x,\ell}[\rho_{\ell-1}] \right) \right|_1 \\ &\leq \sum_{x=1}^{x_{\max}-1} \left| \tilde{\mathcal{E}}_{x,\ell} \circ \mathcal{E}_{x,\ell} [\mathcal{C}_{<x,\ell}[\rho_{\ell-1}]] - \mathcal{C}_{<x,\ell}[\rho_{\ell-1}] \right|_1 \\ &\leq \sum_{x=1}^{x_{\max}-1} \left| \tilde{\mathcal{E}}_{x,\ell} \circ \mathcal{E}_{x,\ell} [\rho_{\ell-1}] - \rho_{\ell-1} \right|_1 \end{aligned} \quad (\text{E.6})$$

where $\mathcal{C}_{<x,\ell} \equiv \prod_{y<x} \tilde{\mathcal{E}}_{y,\ell} \circ \mathcal{E}_{y,\ell}$. The first inequality is from the triangle inequality of trace norm, while the second one is from the contractivity of CPTP maps.

The cumulative error of the total forward-backward evolution is:

$$\left| \tilde{\mathcal{G}}(t) \circ \mathcal{G}(t)[\rho] - \rho \right|_1 \equiv \left| \tilde{\mathcal{C}}_1 \circ \dots \circ \tilde{\mathcal{C}}_{\ell_{\max}} \circ \mathcal{C}_{\ell_{\max}} \circ \dots \circ \mathcal{C}_1[\rho] - \rho \right|_1 \equiv \left| \tilde{\mathcal{C}}_{\{1, \dots, \ell_{\max}\}}[\rho_{\ell_{\max}}] - \rho_0 \right|_1 \quad (\text{E.7})$$

where $\ell_{\max} = t/\delta t$, and $\tilde{\mathcal{C}}_{\{1, \dots, \ell\}} \equiv \tilde{\mathcal{C}}_1 \circ \dots \circ \tilde{\mathcal{C}}_\ell$. We make use of the following iteration relation which holds for $\ell = 1, \dots, \ell_{\max}$:

$$\tilde{\mathcal{C}}_{\{1, \dots, \ell\}}[\rho_\ell] = \tilde{\mathcal{C}}_{\{1, \dots, \ell-1\}}[\rho_{\ell-1}] + \tilde{\mathcal{C}}_{\{1, \dots, \ell-1\}} \left[\tilde{\mathcal{C}}_\ell \circ \mathcal{C}_\ell[\rho_{\ell-1}] - \rho_{\ell-1} \right] \quad (\text{E.8})$$

so that the cumulative error can be expanded and bounded as follows:

$$\begin{aligned}
\left| \tilde{\mathcal{C}}_{\{1, \dots, \ell_{\max}\}}[\rho_{\ell_{\max}}] - \rho_0 \right|_1 &= \left| \sum_{\ell=1}^{\ell_{\max}-1} \tilde{\mathcal{C}}_{\{1, \dots, \ell-1\}} \left[\tilde{\mathcal{C}}_{\ell} \circ \mathcal{C}_{\ell}[\rho_{\ell-1}] - \rho_{\ell-1} \right] \right|_1 \\
&\leq \sum_{\ell=1}^{\ell_{\max}-1} \left| \tilde{\mathcal{C}}_{\{1, \dots, \ell-1\}} \left[\tilde{\mathcal{C}}_{\ell} \circ \mathcal{C}_{\ell}[\rho_{\ell-1}] - \rho_{\ell-1} \right] \right|_1 \\
&\leq \sum_{\ell=1}^{\ell_{\max}-1} \left| \tilde{\mathcal{C}}_{\ell} \circ \mathcal{C}_{\ell}[\rho_{\ell-1}] - \rho_{\ell-1} \right|_1 \\
&\leq \sum_{x, \ell} \left| \tilde{\mathcal{E}}_{x, \ell} \circ \mathcal{E}_{x, \ell}[\rho_{\ell-1}] - \rho_{\ell-1} \right|_1
\end{aligned} \tag{E.9}$$

E.3 Derivation of Eq.(6.12)

Suppose Q is a non-simply-connected region of the toric code ground states surrounding a hole.

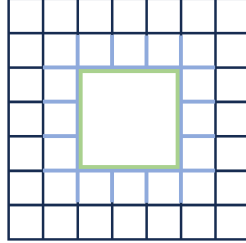


Figure E.1: Illustration of a non-simply connected region Q . Only qubits (edges) that belong to Q is drawn. Supports of the two non-local operators $A_{\tilde{\square}}$ and $B_{\tilde{\square}}$ surrounding the hole are denoted with green and blue edges, respectively.

Before the dephasing, the reduced density operator on Q is:

$$\begin{aligned}
\rho_{0, Q} &= \text{tr}(|\text{t.c.}\rangle \langle \text{t.c.}|) \\
&= \left(\frac{1 + A_{\tilde{\square}}}{2} \right) \left(\frac{1 + B_{\tilde{\square}}}{2} \right) \prod_{\square \text{ within } Q} \left(\frac{1 + A_{\square}}{2} \right) \prod_{+ \text{ within } Q} \left(\frac{1 + B_{+}}{2} \right)
\end{aligned} \tag{E.10}$$

where $A_{\tilde{\square}}$ is a X -loop operator acting on green edges (see Fig.E.1), and $B_{\tilde{\square}}$ is a Z -loop operator acting on blue edges. The two terms show up because Q is not simply-connected.

We notice that each factor in the expression is a projector operator and all factors commute with each other.

Once a Z operator acts on an edge, anyon occupancies of the two adjacent plaquettes will be flipped. Thus if we use the binary vector \mathbf{e} to indicate the set of edges that are acted by Z , plaquettes with a net anyon (indicated with a binary vector \mathbf{m}) are those intersects odd number of times with \mathbf{e} . We denote this relation as $\mathbf{m} = \partial\mathbf{e}$. The dephased state is the weighted mixture of states result from all the possible \mathbf{e} s:

$$\begin{aligned}\rho_{p,Q} &= \frac{1}{2^{z_Q}} \sum_{\mathbf{m}} \Pr(\mathbf{m}) \left(\frac{1+B_{\mp}}{2} \right) \left(\frac{1+(-1)^{m_{\square}} A_{\square}}{2} \right) \prod_{\square \text{ within } Q} \left(\frac{1+(-1)^{m_{\square}} A_{\square}}{2} \right) \prod_{+ \text{ within } Q} \left(\frac{1+B_{+}}{2} \right) \\ &\equiv \frac{1}{2^{z_Q}} \sum_{\mathbf{m}} \Pr(\mathbf{m}) \Pi_{\mathbf{m}}\end{aligned}\tag{E.11}$$

where $\Pr(\mathbf{m}) = \sum_{\mathbf{e}} p^{|\mathbf{e}|} (1-p)^{|Q|-|\mathbf{e}|} \delta(\partial\mathbf{e} = \mathbf{m})$. Noticing that each $\Pi_{\mathbf{m}}$ is a projector and $\Pi_{\mathbf{m}}\Pi_{\mathbf{m}'} = 0$ when $\mathbf{m} \neq \mathbf{m}'$, we obtain the expression for $\rho_{p,Q}$'s von Neumann entropy:

$$S(\rho_{p,Q}) = -\text{tr}(\rho_{p,Q} \log \rho_{p,Q}) = S(\rho_{0,Q}) + H(\mathbf{m})\tag{E.12}$$

Which is the Eq.(6.12) in the maintext. We remark that there is a small difference between the notation here and that adapted in the maintext: In the maintext \mathbf{m} represents only anyon configuration of unit plaquettes within Q , and the net anyon number in the big plaquette (*i.e.* the green plaquette above) is denoted with $\pi(\mathbf{m}_{\Gamma})$. But here we use \mathbf{m} to denote both.

E.4 Tensor network technique for simulating $H(\mathbf{m})$

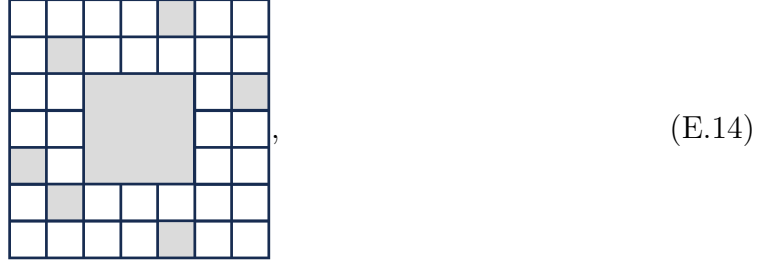
In order to simulate $H(\mathbf{m})$, we first rewrite it as a sample averaged quantity:

$$H(\mathbf{m}) = -\mathbb{E}_{\mathbf{m} \sim \Pr(\mathbf{m})} [\log \Pr(\mathbf{m})].\tag{E.13}$$

Anyon configuration \mathbf{m} can be efficiently sampled by first sampling \mathbf{e} , which follows a product distribution, then calculating \mathbf{m} as $\mathbf{m} = \partial\mathbf{e}$. However a bruteforce evaluation of $\Pr(\mathbf{m})$ is not easy because it requires enumerating all the \mathbf{e} s that can produce \mathbf{m} , which leads to exponentially many terms.

To circumvent this difficulty, we represent $\Pr(\mathbf{m})$ as a two dimensional tensor network. For instance, for the following anyon configuration \mathbf{m} (plaquettes holding anyons

are shaded):



$$(E.14)$$

its probability can be expressed as:

$$\Pr(\mathbf{m}) = \sum_{\mathbf{e}} p^{|\mathbf{e}|} (1-p)^{|Q|-|\mathbf{e}|} \delta(\partial \mathbf{e} = \mathbf{m}) =$$

$$(E.15)$$

where each two-leg circle tensor $T_{s_1 s_2}$, $s_{1,2} \in \{0, 1\}$ is used for assigning weights:

$$T_{s_1 s_2} = \delta(s_1 = s_2) p^{s_1} (1-p)^{s_1} \quad (E.16)$$

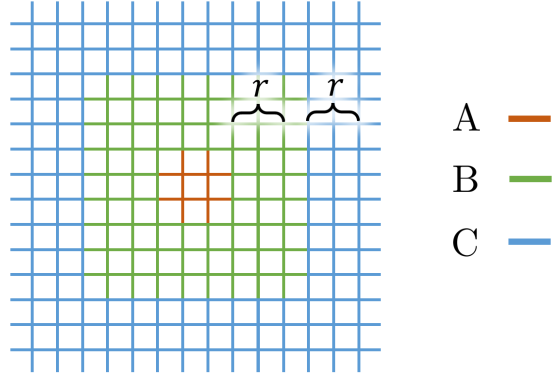
and each q -leg square tensor Q_{s_1, \dots, s_q}^s , $s_i \in \{0, 1\}$ is used for imposing parity constraint on each plaquette:

$$Q_{s_1, \dots, s_q}^s = \delta \left(\sum_{i=1}^q s_i = s \pmod{2} \right). \quad (E.17)$$

In the tensor network image above, Q^0 s and Q^1 s are drawn with yellow and green squares, respectively. Correctness of the tensor network representation can be explicitly checked by expanding all the tensors. The 2D tensor network can be evaluated approximately and efficiently using the boundary matrix product state (bMPS) method [110, 111].

E.5 Details on numerical simulation in Fig.6.3

For numerical results presented in Fig.6.3, regions A , B and C are taken as follows (the plotted figure corresponds to $r = 2$):



Edges belong to different regions are indicated with different colors. When varying r , the region A remains unchanged.

In Figs.6.3(b, c), each data point is averaged over at least 3.5×10^4 samples. In Fig.6.3(d), each data point is averaged over at least 6×10^6 samples.

E.6 Mapping to RBIM's free energy

In this appendix we derive the mapping from the anyon distribution's Shannon entropy $H(\mathbf{m}_Q)$ (*r.h.s.* of Eq.(6.12)) to the RBIM's free energy, and further relate CMI to RBIM's free energy cost due to a point defect.

We focus on an annulus shaped subregion Q which contains a hole. \mathbf{m}_Q is used for denoting both the anyon configuration within Q and the net anyon occupancy in the hole, *i.e.* the hole is treated as a big plaquette. A simply connected region Q can be considered as a special case where the hole contains only one plaquette.

We use binary vector \mathbf{e} to indicate edges that are acted by Z gates, and $\mathbf{m} = \partial\mathbf{e}$ is its corresponding anyon configuration. The probability of observing the configuration \mathbf{m} is:

$$\Pr(\mathbf{m}) = \sum_{\mathbf{e}'} \delta(\partial\mathbf{e} = \mathbf{m}) p^{|\mathbf{e}'|} (1-p)^{|Q|-|\mathbf{e}'|}. \quad (\text{E.18})$$

After a change of variable: $\mathbf{c} \equiv \mathbf{e} + \mathbf{e}'$ (the summation is modular 2), the delta function constraint becomes into $\partial\mathbf{c} = 0$, *i.e.* \mathbf{c} must form a loop. We obtain:

$$\Pr(\mathbf{m}) = [p(1-p)]^{|Q|/2} \sum_{\mathbf{c}} \delta(\partial\mathbf{c} = 0) e^{J \sum_x \eta_x \tilde{c}_x} \quad (\text{E.19})$$

where $\tilde{c}_x \equiv 2c_x - 1$, $\tilde{e}_x \equiv 2e_x - 1$, $J = \frac{1}{2} \log(p/(1-p))$, and the index x runs over edges.

In order to solve the loop constraint, we perform another change of variable: $c_{x=ij} = \sigma_i \sigma_j$, where σ_s are spin variables defined on plaquettes of the original lattice, *i.e.* the dual lattice:

$$\Pr(\mathbf{m}) = \frac{1}{2} [p(1-p)]^{|Q|/2} \sum_{\{\sigma\}} e^{J \sum_{ij} \eta_{ij} \sigma_i \sigma_j} = e^{-F_{\text{RBIM},p}(Q, \tilde{\mathbf{e}}) - c_1 |Q| + c_2} \quad (\text{E.20})$$

where $c_1 = -\frac{1}{2} \ln p(1-p)$ and $c_2 = \ln 2$.

The Shannon entropy of \mathbf{m} can now be written as:

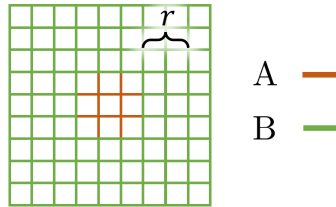
$$H(\mathbf{m}_Q) = - \sum_{\mathbf{m}_Q} \Pr(\mathbf{m}_Q) \log \Pr(\mathbf{m}) \quad (\text{E.21})$$

$$= \sum_{\mathbf{m}_Q} \Pr(\mathbf{m}_Q) (F_{\text{RBIM},p}(Q, \tilde{\mathbf{e}}) + c_1 |Q| + c_2) \quad (\text{E.22})$$

$$= \sum_{\mathbf{e}} \Pr(\mathbf{e}) (F_{\text{RBIM},p}(Q, \tilde{\mathbf{e}}) + c_1 |Q| + c_2) \quad (\text{E.23})$$

$$= \overline{F_{\text{RBIM},p}(Q)} + c_1 |Q| + c_2 \quad (\text{E.24})$$

Finally we look into the meaning of CMI in terms of the RBIM. Letting $Q = B$ and $Q = AB$ following the geometry below:



we obtain that:

$$H(\pi(\mathbf{m}_A), \mathbf{m}_B) - H(\mathbf{m}_{AB}) \quad (\text{E.25})$$

$$= \overline{F_{\text{RBIM},p}} \left(\begin{array}{c} \text{Grid with central defect} \end{array} \right) - \overline{F_{\text{RBIM},p}} \left(\begin{array}{c} \text{Grid} \end{array} \right) + c.c. \quad (\text{E.26})$$

where lattices upon which the corresponding RBIMs are defined were drawn. Since A is fixed, in the large r limit the expression above can be viewed as the free energy cost of introducing a point-like defect in the center of the lattice, which we denote with $F_{\text{def}}(2r)$. Following exactly the same argument, one can derive that $H(\pi(\mathbf{m}_A), \mathbf{m}_{BC}) - H(\mathbf{m}_{ABC}) = F_{\text{def}}(4r)$. We thus obtain the Eq.(6.16):

$$I(A : C|B) = H(\pi(\mathbf{m}_A), \mathbf{m}_{BC}) - H(\mathbf{m}_{ABC}) - (H(\pi(\mathbf{m}_A), \mathbf{m}_B) - H(\mathbf{m}_{AB})) \quad (\text{E.27})$$

$$= \overline{F_{\text{def}}(4r)} - \overline{F_{\text{def}}(2r)}, \quad (\text{E.28})$$

E.7 Convergence of dephasing Lindbladian

In this appendix we examine how fast does $\exp(t\mathcal{L})$, where $\mathcal{L}[\cdot] \equiv \sum_i \mathcal{L}_i = \sum_i \frac{1}{2}(\cdot) - \frac{1}{2}Z_i(\cdot)Z_i$, converges to the complete dephasing channel $\prod_i \mathcal{E}_i[\cdot] \equiv \prod_i \left(\frac{1}{2}(\cdot) + \frac{1}{2}Z_i(\cdot)Z_i \right)$.

We consider the diamond distance: for two quantum channels $\mathcal{C}_1, \mathcal{C}_2$ acting on a n -dimensional Hilbert space, their diamond distance is defined as

$$|\mathcal{C}_1 - \mathcal{C}_2|_{\diamond} \equiv \max_{\rho} |\mathcal{C}_1 \otimes \mathcal{I}_n[\rho] - \mathcal{C}_2 \otimes \mathcal{I}_n[\rho]|_1 \quad (\text{E.29})$$

where \mathcal{I}_n is the identity channel.

We first check the distance between $\exp(\mathcal{L}_i)$ and \mathcal{E}_i . Bringing in $\mathcal{C}_1 = \exp(t\mathcal{L}_i)$ and $\mathcal{C}_2 = \mathcal{E}_i$, we get:

$$|\exp(t\mathcal{L}_i) - \mathcal{E}_i|_{\diamond} = \left| p_t - \frac{1}{2} \right| \cdot \max_{\rho} |Z\rho Z - \rho|_1 = \frac{1}{2}e^{-t}\lambda \quad (\text{E.30})$$

where $p_t = (1 - e^{-t})/2$. We let $\lambda \equiv \max_{\rho} |Z\rho Z - \rho|_1$, which is an $O(1)$ constant.

Then the diamond distance between \mathcal{E} and $\sqcup\mathcal{L}$ is bounded as:

$$|\exp(t\mathcal{L}) - \mathcal{E}|_\diamond \leq \sum_i |\exp(t\mathcal{L}_i) - \mathcal{E}_i|_\diamond = \frac{L}{2} e^{-t\lambda} \quad (\text{E.31})$$

Thus in order to achieve ϵ proximity, it suffices to pick $t = O(\log(L/\epsilon))$.

In conclusion, \mathcal{E} can be well-approximated by a quasi-local Lindbladian evolution.